

University of Windsor

Scholarship at UWindor

Electronic Theses and Dissertations

Theses, Dissertations, and Major Papers

2007

A study of hydraulic intake entrainment envelope delineation methods

Temitope Veronica Olatunji
University of Windsor

Follow this and additional works at: <https://scholar.uwindsor.ca/etd>

Recommended Citation

Olatunji, Temitope Veronica, "A study of hydraulic intake entrainment envelope delineation methods" (2007). *Electronic Theses and Dissertations*. 4619.
<https://scholar.uwindsor.ca/etd/4619>

This online database contains the full-text of PhD dissertations and Masters' theses of University of Windsor students from 1954 forward. These documents are made available for personal study and research purposes only, in accordance with the Canadian Copyright Act and the Creative Commons license—CC BY-NC-ND (Attribution, Non-Commercial, No Derivative Works). Under this license, works must always be attributed to the copyright holder (original author), cannot be used for any commercial purposes, and may not be altered. Any other use would require the permission of the copyright holder. Students may inquire about withdrawing their dissertation and/or thesis from this database. For additional inquiries, please contact the repository administrator via email (scholarship@uwindsor.ca) or by telephone at 519-253-3000ext. 3208.

**A STUDY OF HYDRAULIC INTAKE ENTRAINMENT ENVELOPE
DELINEATION METHODS**

by

Temitope Veronica Olatunji

A Thesis

Submitted to the Faculty of Graduate Studies
through the Department of Civil and Environmental Engineering
in Partial Fulfillment of the Requirements for
the Degree of Master of Applied Science at the
University of Windsor

Windsor, Ontario, Canada

2007

© 2007 Temitope V. Olatunji



Library and
Archives Canada

Bibliothèque et
Archives Canada

Published Heritage
Branch

Direction du
Patrimoine de l'édition

395 Wellington Street
Ottawa ON K1A 0N4
Canada

395, rue Wellington
Ottawa ON K1A 0N4
Canada

Your file *Votre référence*
ISBN: 978-0-494-34933-5
Our file *Notre référence*
ISBN: 978-0-494-34933-5

NOTICE:

The author has granted a non-exclusive license allowing Library and Archives Canada to reproduce, publish, archive, preserve, conserve, communicate to the public by telecommunication or on the Internet, loan, distribute and sell theses worldwide, for commercial or non-commercial purposes, in microform, paper, electronic and/or any other formats.

The author retains copyright ownership and moral rights in this thesis. Neither the thesis nor substantial extracts from it may be printed or otherwise reproduced without the author's permission.

AVIS:

L'auteur a accordé une licence non exclusive permettant à la Bibliothèque et Archives Canada de reproduire, publier, archiver, sauvegarder, conserver, transmettre au public par télécommunication ou par l'Internet, prêter, distribuer et vendre des thèses partout dans le monde, à des fins commerciales ou autres, sur support microforme, papier, électronique et/ou autres formats.

L'auteur conserve la propriété du droit d'auteur et des droits moraux qui protègent cette thèse. Ni la thèse ni des extraits substantiels de celle-ci ne doivent être imprimés ou autrement reproduits sans son autorisation.

In compliance with the Canadian Privacy Act some supporting forms may have been removed from this thesis.

Conformément à la loi canadienne sur la protection de la vie privée, quelques formulaires secondaires ont été enlevés de cette thèse.

While these forms may be included in the document page count, their removal does not represent any loss of content from the thesis.

Bien que ces formulaires aient inclus dans la pagination, il n'y aura aucun contenu manquant.


Canada

ABSTRACT

Surface water has been a reliable source of providing municipal drinking water over the years by drawing water through hydraulic intake pipe. In this study, an effort is made to establish the entrainment envelope for the hydraulic intake pipe in a uniform cross-flow. The envelope is essential in defining the proportion of passing contaminants and flow ingested by the intake. An analytical delineation method – potential flow theory investigated the two and three dimensional flow solutions. The results were validated by numerical modeling of inviscid and laminar flow conditions; and velocity measurements obtained with laser Doppler anemometer confirmed the intake entrainment envelope as the immediate zone from which the water intake withdraws water. Comparison of the flow pattern, stagnation streamlines and velocity field plots show that intake entrainment envelope is characterized by a symmetrical half-body which increase in size with increasing intake discharge irrespective of the flow conditions. The entrainment envelope for viscous flow exceeded the inviscid radial flow in width and depth by distorting the entrainment envelope as a result of clockwise vortices found in the vicinity of the hydraulic intake for high intake withdrawal rates. The three-dimensional study confirmed these deductions and inferred the validity range for the potential theory and inviscid flow assumption.

To the Almighty God, the Creator of heaven and earth

ACKNOWLEDGEMENTS

Life would not be worth living without the mercies of the Almighty God. My profound appreciation and heartfelt gratitude to my advisors, Dr. Rupp Carriveau and Dr. David S-K Ting for their patience, invaluable supervision, guidance, thoughtful insights, encouragement and support throughout this research. Sincere gratitude is also expressed to my committee members; Dr. A. Edrisy and Dr. S. Cheng for their helpful comments, suggestions and their valuable time.

I appreciate Mr. Matthew St. Louis, Mr. Lucian Pop (Luke), Mr. Paul Fraser and Mr. Patrick Seguin for their devotion in building the experimental setup and providing workstation related supports. Your prompt action and commitment to remedy the problems encountered during the testing program assisted the timely completion of this study. Special thanks to Mr. M.A.A. Faruque for his assistance during my experimental runs. The encouragements from my friends and fellow graduate students, especially Mr. Alex Bey, Mr. Olumuyiwa Olatunji and Mr. Zakir Faruquee are highly appreciated. Financial supports from the University of Windsor and NSERC in terms of GA, RA and Tuition Scholarship are greatly valued.

Lastly, I am greatly indebted to my affectionate mother whose love and advice are unparalleled; Mr. and Mrs. Yinka Omiyale for their unstinting efforts and immutable supports towards my career in life and to all members of my family.

TABLE OF CONTENTS

ABSTRACT	iii
DEDICATION	iv
ACKNOWLEDGEMENTS	v
LIST OF TABLES	x
LIST OF FIGURES	xi
NOMENCLATURE	xv
CHAPTER 1 INTRODUCTION	1
1.1 Flow Field around Hydraulic Intake	2
1.2 Motivation	5
1.3 Objectives	6
1.4 Scope and Thesis Outline	7
CHAPTER 2 LITERATURE REVIEW	8
2.1 Introduction	8
2.2 Vortices at Hydraulic Intakes	8
2.3 Critical Submergence for a Hydraulic Intake	11
2.4 Three-Dimensional Study of Flow at a Hydraulic Intake	14
2.5 Evaluation of Literature	16
CHAPTER 3 DELINEATION METHODS	17
3.1 Introduction of Prototype Geometry	17
3.2 Scaling Parameters and Model Assumptions	18
3.3 Analytical Method: Potential Flow Analysis	20
3.3.1 Two-dimensional flow	21
3.3.2 Three-dimensional flow	23
3.4 Numerical Method	24
3.4.1 Governing equation discretization	26

3.4.2	Computational geometry and boundary conditions	26
3.4.3	Model discretization	29
3.4.4	Discussion of convergence	31
3.4.5	Grid independence	32
3.5	Experimental Model	33
3.5.1	Model description	33
3.5.2	Experimental procedure	35
3.5.3	Measurement technique	36
3.6	Testing Program	37
CHAPTER 4 RESULTS AND DISCUSSION		 39
4.1	Entrainment Envelope Delineation Criteria	40
4.2	Two-Dimensional Flow Solution	41
4.3	Potential Flow Solution of Two-Dimensional Flow	42
4.4	Numerical Solution of Two-Dimensional Flow	44
4.4.1	Flow field for inviscid flow condition	45
4.4.2	Comparison of inviscid data to potential flow theory	49
4.4.3	Flow field for laminar flow condition	51
4.4.4	Comparison of vorticity contour to validate entrainment envelope distortion	57
4.4.5	Comparison of numerical laminar data to potential flow theory	59
4.5	Experimental Results	61
4.6	Review of Two-Dimensional Flow Results	64
4.7	Three-Dimensional Flow Study	65
4.8	Potential Flow Solution of Three-Dimensional Flow	65

4.9	Numerical Solution of Three-Dimensional Flow	67
4.9.1	Flow field for 3-D inviscid flow condition	67
4.9.2	3-D numerical inviscid and analytical data comparison	70
4.9.3	Flow field for 3-D laminar flow condition	71
4.9.4	Numerical laminar and analytical data comparison	76
4.10	Review of Three-Dimensional Flow Results	77
4.11	Physical Significance of Study to IPZ Delineation	78
CHAPTER 5	CONCLUSIONS AND RECOMMENDATIONS	82
5.1	Conclusions	82
5.2	Recommendations for Future Works	85
REFERENCES		86
APPENDIX A	Scaling Parameters for Experimental and Numerical model	90
APPENDIX B	Properties of Water	92
APPENDIX C	Convergence History	93
	C1. Convergence of residual history	93
	C2. Convergence of monitored flow variables	95
	C3. Convergence by flux report	97
APPENDIX D	Numerical Error Analysis	98
APPENDIX E	Uncertainty Analysis of Experimental data	101
APPENDIX F	Tabulated Data Set	102

F1.	Comparison of 2-D numerical inviscid result with potential flow theory	102
F2.	Summary of two-dimensional flow data	103
F3.	Summary of three-dimensional flow data	105
VITA AUCTORIS		 105

LIST OF TABLES

CHAPTER 3

Table 3.1:	Summary of test conditions	38
------------	----------------------------	-------	----

APPENDICES

Table A.1:	Relevant scaling parameters for experimental model	91
Table A.2:	Relevant scaling parameters for computational model	91
Table B.1:	Properties of water at 20°C	92
Table C.1:	Flux report	97
Table D.1:	Error estimate for H and r_o	100
Table F.1:	Analytical data comparison with numerical inviscid data	102
Table F.2:	Effect of singularity on entrainment envelope (EE) width	102
Table F.3:	Entrainment envelope data for 2-D solution	104
Table F.4:	Entrainment envelope data for 3-D solution of Test B	105

LIST OF FIGURES

CHAPTER 1

Figure 1.1:	Picture of an intake pipe situated at cross-flow	3
Figure 1.2:	Schematic sketch of intake entrainment envelope	4
Figure 1.3:	3-D flow patterns in hydraulic intake at cross-flow	5

CHAPTER 2

Figure 2.1:	Vortex type classification	9
Figure 2.2:	(a) Critical submergence representation of S_c	13
	(b) Critical spherical sink surface	
Figure 2.3:	Streamline of velocity components with intake cap	15

CHAPTER 3

Figure 3.1:	a) Prototype profile geometry Intake face	18
	b) Conical transition of intake configuration	
Figure 3.2:	Potential flow representation of an intake	21
Figure 3.3:	2-D representation of uniform flow and point sink	22
Figure 3.4:	Representation of Rankine half-body of revolution.	24
Figure 3.5:	2-D schematic of computational geometry (Plan view)	27
Figure 3.6:	3-D boundary conditions for computational geometry	28
Figure 3.7:	a) Typical grid for 2-D computational domain full view	30
	b) Typical grid for 2-D computational domain zoomed view	
Figure 3.8:	a) Typical computational mesh full view of domain	30
	b) Horizontal section of grid through the centre of the intake pipe	31
Figure 3.9:	Grid independence of H and r_s of entrainment envelope	32
Figure 3.10:	Experimental setup	34
Figure 3.11:	Laboratory flume set up for intake entrainment envelope study	35

Figure 3.12:	Sampling grid for experimental model	37
 CHAPTER 4			
Figure 4.1:	Schematic sketch of entrainment envelope delineation criteria	41
Figure 4.2:	2-D potential flow result for intake discharge - Case 1	42
Figure 4.3:	2-D potential flow result for intake discharge - Case 2	43
Figure 4.4:	2-D potential flow result for intake discharges (Cases 1 – 5)	44
Figure 4.5:	Effect of intake discharge on the entrainment envelope parameters	44
Figure 4.6:	Flow patterns of inviscid flow for Case 1 ($Q_i = 0.005$), Case 3 ($Q_i = 0.025$) and Case 5 ($Q_i = 0.125$)	47
Figure 4.7:	Stagnation streamline plots of inviscid flow	48
Figure 4.8:	a) Analytical data comparison to numerical inviscid result for H b) Influence of singularity on numerical inviscid solution of Tests A, B and C	50
Figure 4.9:	Analytical data comparison to numerical inviscid result for r_s and r_o	51
Figure 4.10:	Flow patterns of laminar flow for Case 3 ($Q_i = 0.025$), Case 4 ($Q_i = 0.075$) and Case 5 ($Q_i = 0.125$)	53
Figure 4.11:	Stagnation streamline plots of laminar flow	56
Figure 4.12:	Contour plots of vorticity magnitude (1/s) for Case 5	58
Figure 4.13:	Analytical data comparison to numerical laminar solution for H	59
Figure 4.14:	Analytical data comparison to numerical laminar solution for r_s and r_o	60
Figure 4.15:	Influence of singularity on numerical laminar solution	61
Figure 4.16:	a) Velocity vector plots for Test A full view b) Zoomed view of vectors at intake region of influence	62

Figure 4.17:	Velocity vector plots for Case 2	63
Figure 4.18:	Velocity vector plots for Case 3	63
Figure 4.19:	3-D potential flow result for intake discharges Cases 1-5	66
Figure 4.20:	Relationship between intake discharge and entrainment envelope parameters	66
Figure 4.21:	Flow patterns of inviscid flow for Case 1 ($Q_i = 0.005$) at a vertical plane $z = 25d_o$	68
Figure 4.22:	Flow patterns of inviscid flow for Case 1 ($Q_i = 0.005$) at a horizontal plane $y = 0$	68
Figure 4.23:	Stagnation streamline plots of inviscid flow at vertical plane $z = 25d_o$	69
Figure 4.24:	Stagnation streamline plots of inviscid flow at horizontal plane $y = 0$	69
Figure 4.25:	Comparison of 3-D potential flow and numerical inviscid solutions	71
Figure 4.26:	Flow patterns of laminar flow for Case 3 ($Q_i = 0.025$), Case 4 ($Q_i = 0.075$) and Case 5 ($Q_i = 0.125$) at a vertical plane $z = 25d_o$	72
Figure 4.27:	Flow patterns of laminar flow for Case 3 ($Q_i = 0.025$), Case 4 ($Q_i = 0.075$) and Case 5 ($Q_i = 0.125$) at a horizontal plane $y = 0$	73
Figure 4.28:	Stagnation streamline plots of laminar flow at vertical plane $z = 25d_o$	75
Figure 4.29:	Stagnation streamline plots of laminar flow at horizontal plane $y = 0$	75
Figure 4.30:	Numerical laminar flow data compared to potential flow solution	76
Figure 4.31:	Physical model location in Great Lakes connecting channel	80

Figure 4.32:	a) Zone delineation techniques by MOE guidance module (2006): preliminary intake zone	81
	b) Revised zone based on geophysical properties		
Figure 4.33:	Illustration of GC 1PZ1 and entrainment envelope	81

APPENDICES

Figure C1:	Convergence of residuals for 2-D laminar model (intake proportion $Q_i/Q = 0.0833$; Test A)	94
Figure C2:	Convergence of residuals for 2-D laminar model ($Q_i/Q = 0.0167$; Test A)	94
Figure C3:	Convergence of residuals for 3-D laminar model ($Q_i/Q = 0.034$; Test B)	95
Figure C4:	Convergence of mass flow rate on intake outlet for 3-D laminar model ($Q_i/Q = 0.385$; Test A)	96
Figure C5:	Convergence of drag coefficient for 3-D laminar model ($Q_i/Q = 0.345$ for Test B)	96
Figure C6:	Convergence of lift coefficient for 3-D laminar model ($Q_i/Q = 0.345$; Test B)	97

NOMENCLATURE

ACRONYMS

CFD	Computational Fluid Dynamics
CSSS	Critical Spherical Sink Surface
EE	Entrainment Envelope
IPZ	Intake Protection Zone
LDA	Laser Doppler Anemometer
LES	Large Eddy simulation
MOE	Ministry of Environment
RHB	Rankine Half-Body
SWP	Source Water Protection
US EPA	United State Environment Protection Agency
USGS	Unites State geological survey
2-D	Two-Dimensional
3-D	Three-Dimensional

ENGLISH SYMBOLS

DEFINITION

b	width of computational domain(m)
B	width of headrace channel (m)
c	scaled intake clearance (m)
C_d	discharge coefficient
D	entrainment envelope depth (m)
d_o	intake diameter (m)
d_r	refined intake diameter (m)
F	intake Froude number = $V_i/\sqrt{gd_o}$
g	gravitational acceleration (m/s^2)
H	entrainment envelope width (m)
I^*	scaled intake penetration (m)
K	intake diameter kolf number = $\Gamma/V_i d_o$
L	characteristic length (m)

L_r	length ratio
N_r^*	dimensionless circulation number = $\frac{S\Gamma}{Q}$
p	pressure (Pa)
Q	channel flow rate = $U_\infty A$ (m^3/s)
Q_i	intake discharge = $V_i \pi d_o^2 / 4$ (m^3/s)
r	radial distance from intake centerline (m)
r_o	radial distance from intake centre to entrainment envelope/stagnation point (m)
r_s	horizontal distance from intake centre to entrainment envelope (m)
Re	intake Reynolds number = $V_i d_o / \nu$
S	dimensionless intake submergence (h/d_o)
t	proportionality constant in %
U	uniform flow velocity (m/s)
V_i	intake velocity (m/s)
V_θ	tangential velocity (m/s)
V_r	radial velocity (m/s)
w^*	scaled width (m)
W	weber number = $\rho d_o V_i^2 / \sigma$
x	streamwise direction
x_u	upstream distance (m)
x_d	downstream distance (m)
y	cross-stream direction
y_u	top wall distance (m)
y_d	bottom wall distance (m)
z	span-wise direction

GREEK SYMBOLS

β	angle of rotation (radians)
α	approach flow angle (radians)

Γ	circulation of vortex = $2\pi rV_\theta$ (m^2/s)
σ	surface tension (N/m)
ν	kinematic viscosity of water (m^2/s)
ν_e	effective viscosity (m^2/s)
ρ	mass density of water (kg/m^3)
ψ	stream function (m)
ψ_i	streamline
θ	angle of revolution (radians)
ϕ	residuals of velocity and pressure at any iteration

SUBSCRIPTS

a	analytical data
c	critical
f	inviscid flow data
i	intake
l	laminar flow data
m	model
p	prototype
∞	free-stream

CHAPTER 1

INTRODUCTION

Hydraulic intakes have received attention over the years because of their widespread application and relevance in hydraulic engineering which includes its usage in hydropower stations, cooling systems of electric power generation plants, and cooling-water pump intakes. These intakes are structures of different cross sectional shapes (e.g. horizontal, rectangular, circular, elliptical, conical) through which fluid is withdrawn from a source in order to supply water for municipal, domestic, irrigation and industrial demands. In general, our water comes primarily from two sources: surface water and ground water. Surface water is open to the atmosphere and includes lakes, rivers, streams, creeks, oceans and wetlands. Groundwater is water found beneath the Earth's surface between the cracks and spaces in soil, sand and rocks such as underground aquifers.

In 2006, statistical results established that approximately 74% of Canadians get their municipal water supply from surface water [MOE, Clean Water Act, 2006] while 61% of United State population [US EPA, 2006] depends on surface water. Therefore, it can be concluded that significant portion of the population is dependent on surface water as a source of drinking water. This accentuates the importance of protecting municipal raw water quality drawn into the water intakes from potential contamination and depletion. In the interest of safeguarding public health, the Ministry of Environment Canada introduced in 2006 the Source Water Protection (SWP) program. The SWP program focuses on protecting both the quality and quantity of our water resources from contamination that might enter from nearby regions or known sources (e.g. storm sewer watersheds and open drainage ditches). An integral part of the SWP program is the

delineation of surface water Intake Protection Zones (IPZ) for all public water intakes located in various surface water sources. The IPZ is the area/zone around the intake that is to be protected from immediate contaminants of concern (such as chemical spill; agricultural and commercial discharges; and waste water effluents) that might potentially impact the quality of water drawn into the intake. The initial IPZ, also called the most vulnerable area as a result of its close proximity to the intake is designated by marking a fixed starting radius of 1km upstream of an intake. This explains that the initial IPZ includes the exact region from which the intake withdraws its water (defined as entrainment envelope herein) and its adjacent areas.

1.1 Flow Field around Hydraulic Intake

An increasing number of hydraulic intakes are used in lakes, oceans and rivers to draw in water for human consumption. In most cases when intakes are situated in rivers, they are situated perpendicularly to the direction of flow in the river as depicted in Figure 1.1. Such set-up is usually referred to as cross-flow in hydraulic studies. The extent of approaching river flow drawn into water intake largely depends on the river flow characteristics (e.g. the river channel velocity, depth, width, nature of flow) and the hydraulic intake flow configuration (e.g. the intake flow rate, intake diameter). The intake design considered in this study is schematically depicted in Figure 1.2 which comprises of a simple intake pipe situated at cross-flow.

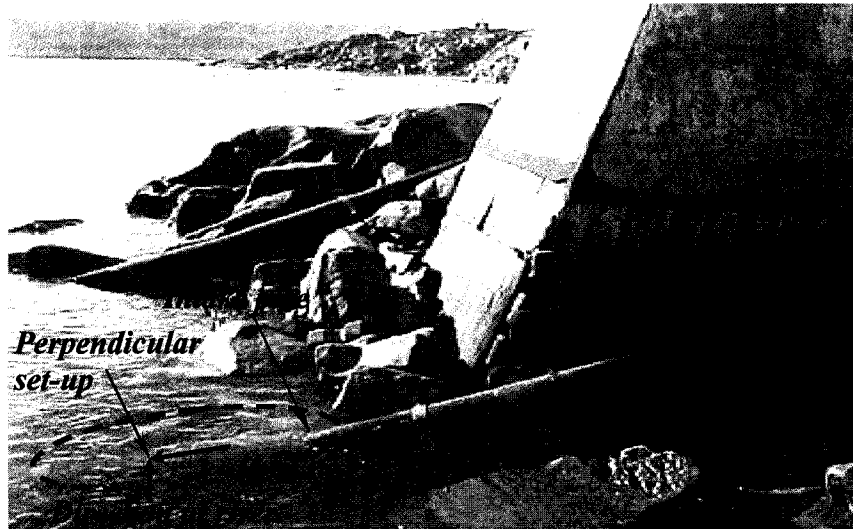


Figure 1.1: Picture of an intake pipe situated at cross-flow

Generally, the intake pipe draws in water from its surroundings or its flow boundaries. The flow boundaries represent the hydraulic intake region of withdrawal influence or the area from which the intake actually withdraws its water. This region is defined as the “entrainment envelope (EE)” in this study. Carriveau et al. [2002] described the EE as the region of flow in which intake bound velocities are sufficient to transport fluid and fluid borne material into the intake. The entrainment envelope can be observed in plan view in Figure 1.2 with the water flowing from left to right. Water is withdrawn at the intake point through the delivery pipe to the end user. Thus, for the case of this approaching flow, the flow-field information is needed to delineate local regions immediately around the intake structure and the actual flow boundaries from which the intake withdraws water, that is, the entrainment envelope (shown in dark blue). The flow-field is represented by streamlines (lines that are tangential to the velocity vectors throughout the flow-field) and any streamlines that crosses this envelope will be withdrawn into the intake. Specifically, streamlines ψ_1 , ψ_2 , and ψ_3 will subsequently be

entrained into the intake while streamlines ψ_4 , ψ_5 will pass without being entrained. Close inspection of Figure 1.2 reveals that the delineated entrainment envelope is the critical region of water required to be protected from all contaminants for the municipality to withdrawal potable water from the approaching flow. In other words, if contaminant plume is located within streamlines ψ_1 , ψ_2 , or ψ_3 or confined within the EE, it will enter the intake.

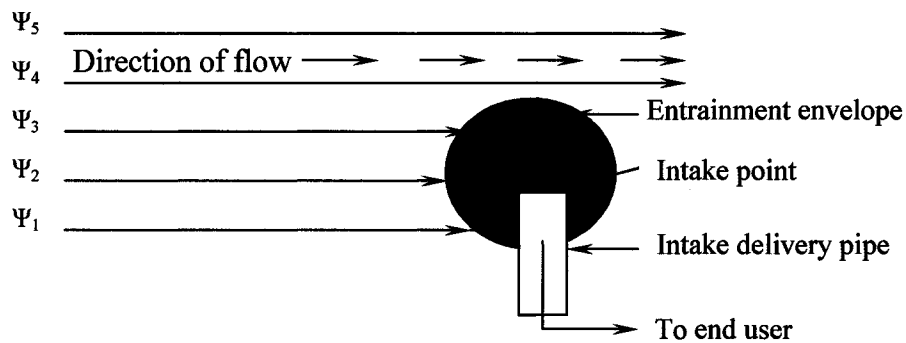


Figure 1.2: Schematic sketch of intake entrainment envelope

A 3-D schematic representation of the entrainment envelope formation for hydraulic intakes situated in a cross-flow or river is illustrated in Figure 1.3. As the flow approaches the intake, it is accelerated by the suction pressure at the end of the intake causing the flow to divide such that a portion enters the intake with the remainder continuing downstream in the main channel. The portion withdrawn by the intake is marked by dividing streamlines that define the region from which the intake pipe draws its water. As explained earlier, this region defines the entrainment envelope for the river intake and the illustration clearly revealed that any pollutants located outside the dividing stream surface will not enter the intake.

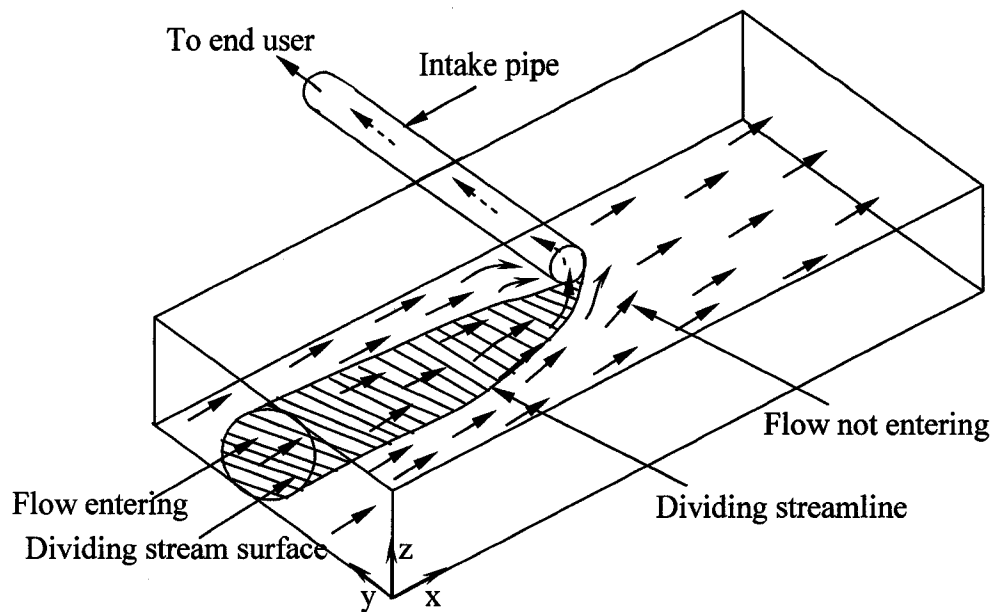


Figure 1.3: 3-D flow patterns in hydraulic intake at cross-flow

1.2 Motivation

The study of flow pattern and behaviour around the intake has many industrial applications and is essential in solving numerous hydraulic problems faced at various intakes. Some of these problems have been investigated over the years, but the need for the use of water intakes to meet various needs of urban communities persistently increases, thereby resulting in continuous research to channel newly developed concerns. The focus of this study is to investigate the entrainment envelope for hydraulic intakes in surface water (river) and the motivation for this study is drawn from the following considerations.

- (a) The source water protection program (SWP) introduced by the Ministry of Environment (MOE) and the United States Environmental Protection Agency which focuses on designating the protection zone (IPZ) around the drinking water intakes is an emerging research area. The lack of information in characterizing

these drinking water intakes as outlined in MOE Source Protection Guidance Module [2006] indicates the need for a systematic study of the hydrodynamic characteristics associated with hydraulic intakes in cross-flow.

- (b) Accurate delineation of the entrainment envelope has the possibility to aid the water treatment plant operator in calculating the actual (minimum) response time to respond to adverse conditions or an emergency such as spill release in the river.
- (c) A substantial number of studies focused on the control of vortices at hydraulic intakes that may impede the efficiency of the pump intakes. Despite this, no comprehensive studies have been conducted in delineating entrainment envelope.

1.3 Objectives

The purpose of the present investigation is to study the flow-field into a hydraulic intake since a detailed understanding and depiction of the entrainment envelope has the potential to be a useful tool in protecting consumers of surface water. Based on this and the considerations stated in Section 1.2, the objectives of this study are to:

- (1) Evaluate analytical, computational and experimental methods of delineating the intake entrainment envelope;
- (2) Compare each delineation approach employed;
- (3) Complement the Intake Protection Zone (IPZ) delineation project implemented by the Ministry of Environment Canada and to
- (4) Further understand the 3-D flow patterns of an intake in cross-flow.

1.4 Scope and Thesis Outline

Three practical tests were numerically simulated in this study for both two and three dimensional models in order to achieve the objectives stated in Section 1.3. The relative size of the entrainment envelope was determined by varying the intake withdrawal rates. The physical problem was then solved analytically and experimentally to enhance results validation and its physical relevance.

The thesis is laid out in the following format. A detailed review of past work in the area of interest is summarized in Chapter 2. Chapter 3 explains the methodology by describing in details the problem geometry; the analytical method with the principal equations; the numerical method which includes the numerical schemes, mesh generation techniques, boundary conditions and governing equations employed in the computational domain; the experimental details including the setup, measurement techniques and the procedures adopted. The data and results obtained are presented and discussed in Chapter 4, which centers on validating and comparison of three delineation approaches. Based on the discussion of the results, conclusions are drawn in Chapter 5 along with recommendations for future work.

CHAPTER 2

LITERATURE REVIEW

2.1 Introduction

The flow around and into intakes has been investigated by many researchers. Theoretical and experimental flow characteristics at submerged intakes, ranging from the study of vortices at intakes to effects of submerged hydraulic intakes on the flow boundary have been widely addressed in the research. Some of the common themes reviewed are presented in the following order.

2.2 Vortices at Hydraulic Intakes

The occurrence of vortices is one of the major potential hazards faced at many hydraulic intakes. The vortex formation at intakes situated in river is mainly stimulated by eccentric orientation of the intake relative to a symmetric approach flow area, asymmetric approach flow conditions due to irregularities in the boundary lining, non uniform velocity distribution caused by boundary layer separation, wind action and counter currents. Despite many years of investigation, the occurrence of these vortices is still unpredictable and continues to be given special consideration when designing both submerged symmetric and asymmetric water intakes. These vortices are mostly classified as air-core and dye-core vortices; they are illustrated in Figure 2.1. The air core vortices refer to vortex that entrains air through their central core as a result of the high tangential velocity near its centre. This air-core entrains large quantities of debris, frazil and zebra mussels into the intake pipes which consequently results in severe blockages of the intake structures, pollution of water drawn into the intake, reduction of intake discharge capacity, affects the intake efficiency and leads to unstable operation, noise and vibration

of the hydraulic machinery. In contrast, dye-core vortices are characterized as vortex without air which can only be visualized by the injection of dye or particles at the vortex core [Carriveau et al., 2002]. They are also referred to as internal vortices that lead to air-core vortex formation in a swirling flow field. For intakes located in large bodies of water (e.g. river), the weak dye-core vortices are commonly found and are capable of causing hazards to the intakes such as significant enlargement of the entrainment zone. The bulk of previous studies on vortices have focused on mitigating or avoiding air core vortices at pump sumps and predicting the formation of vortices at hydraulic intakes. Based on the established fact that vortices have the potential of reducing the discharge capacity of the intake, the subsequent effect of the vortices on the size of entrainment envelope was assessed in this study.

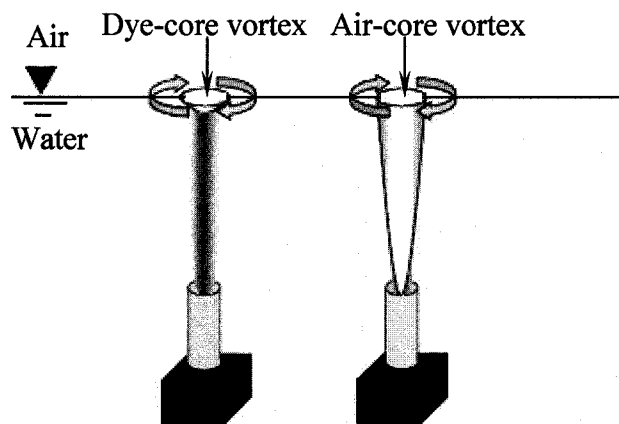


Figure 2.1: Vortex type classification [Carriveau, 2002]

Gulliver and Rindels work in 1987 laid the foundation for the study of internal vortices or dye core vortices at intakes. They defined the dye core vortex as the weak, free surface vortices found at vertical intakes in the head race channel. Their experimental work simulated weak vortices at vertically arranged hydropower intakes in

headrace channels. The authors represented the intake vortex flow fields as three dimensional, thereby allowing minimal simplification of the equation of motion. By considering the geometry of a typical headrace channel and earlier work of Anwar [1966], they developed an expression for a dimensionless circulation number used in analyzing their experimental data. The dimensionless circulation number is

$$N_r^* = \left(\frac{\tan(\alpha)}{1 + \frac{\beta L}{2 B} \tan(\alpha)} \right) \quad (2.1)$$

where $N_r^* = \frac{S\Gamma}{Q}$, α = approach flow angle, L = length of headrace channel, B = width of headrace channel, β = constant of the order of 1, S = intake submergence, Γ = circulation and Q = channel discharge. Since their work focused on defining the dye-core vortex, flow parameters were chosen to avoid surface tension or viscous scale effects in order to easily quantify their model. They ascertained that the transition from radial to vortical flow occurred over a range of flow conditions and they likened this phenomenon to the transition from laminar to turbulent boundary layer flow. They later deduced that a disturbance in intake approach flow may cause the formation of dye core vortex which may have impact on the hydraulic intake performance. Nevertheless, their work tried to mitigate occurrence of vortices by suggesting that large dimensionless submergence that is highly dependent upon approach flow angle and headrace length/width ratio is required to avoid weak vortices. They additionally indicated that locating the side and rear walls close to the intake and reducing the approach flow angles will prevent the dye-core vortex formation at hydraulic intakes.

Carriveau et al. [2002] conducted an experimental study to investigate the entrainment envelope of dye-core vortices associated with submerged hydraulic intake for swirling and non-swirling flows. Their study further clarified the importance of dye-core vortices and how they could occur in deeply submerged lake intakes especially in colder climates. Their experiment was conducted in an acrylic tank, designed to generate swirling and non swirling flow. Three-dimensional velocity measurements were taken and the vortex entrainment envelope was visualized with dye. The two conditions were compared using the velocity distribution and the flow pattern into the intake. Results of their investigation established that the swirling flow cases generated stable dye-core vortices with a significant large envelope reaching the water surface for all the depths of flow considered while the non-swirling flow produced radial flow pattern into the sink as suggested by potential flow theory and supports a small withdrawal envelope that reduces the possibility of far-field entrainment. They further inferred from their study that the regions of significant velocities are much larger in the swirling flow as compared with the non-swirling flow.

It is imperative to note that the present study did not investigate the presence of dye core vortices at hydraulic intake (since dye-core vortex can only be found in a submerged hydraulic intake), but the realization of their study provides additional motivation to employ potential flow theory to analytically investigate the radial flow pattern into the sink for the non-swirling flow considered in this study.

2.3 Critical Submergence for a Hydraulic Intake

The term submergence is employed in hydraulic intake studies to define the dimensionless ratio of the depth of water above the intake mouth to the intake diameter.

The critical submergence (S_c) refers to the minimum submerged value required to avoid a vortex at the intake. Yildirim and co-researchers [1995, 2000, 2002 and 2004] have made valuable contributions in defining the critical submergence for various shapes of hydraulic intakes in a cross flow with the intention to avoid the occurrences of vortices at hydraulic intakes. To the best of the writer's knowledge, their results have only contributed towards alleviating the vortices effects at hydraulic intakes.

The study of Yildirim and Kocabas [1995] investigated the critical submergence for an air-entraining vortex at intakes in a uniform canal flow. The authors employed the continuity equation and potential flow solution for the combination of a "point sink" and uniform canal flow (known as the Rankine's ovoid or Rankine half-body) to predict the occurrence of critical submergence. The flow into a cylindrical intake pipe was approximated as a "point sink", having the same centre and discharge as the intake. By solving the generalized equation of the Rankine half-body of revolution [Yuan, 1967], the derived equation for the critical submergence was expressed as:

$$\frac{S_c}{D_i} \approx 0.55 \left(C_d \frac{V_i}{U_\infty} \right)^{1/2} \quad (2.2)$$

where S_c = critical submergence, C_d = discharge coefficient, V_i = intake velocity, U_∞ = approach flow velocity and D_i = intake diameter. Figure 2.2 illustrates the application of Equation 2.2 and their findings. They infer that at the critical condition, the upper boundary of the Rankine half-body reaches the free surface level above the intake. Thus, the vertical distance between any point on the upper portion of the Rankine half-body and intake level is equal to S_c as shown in Figure 2.2a. In other words, they define S_c as the radius of the imaginary critical spherical sink surface (CSSS), shown in Figure 2.2b. Experiments were later conducted on a vertically oriented intake in a cross flow with the

effects of Reynolds number (ratio of inertia to viscous forces), Weber number (ratio of fluid inertia to surface tension), Froude number (ratio of inertia to gravitational forces) and Kolf number (ratio of circulation effect to inertia forces) neglected. The experimental data obtained was compared with the work of Yildirim and Jain [1981], Gulliver and Rindels [1987]; they found that the agreement of the analytical and experimental results was good. Equation 2.2 was employed in this study to determine the minimum depth of submergence (S_m) required to avoid the occurrence of air-core vortex or lessening the intensity of the vortex field at the hydraulic intake.

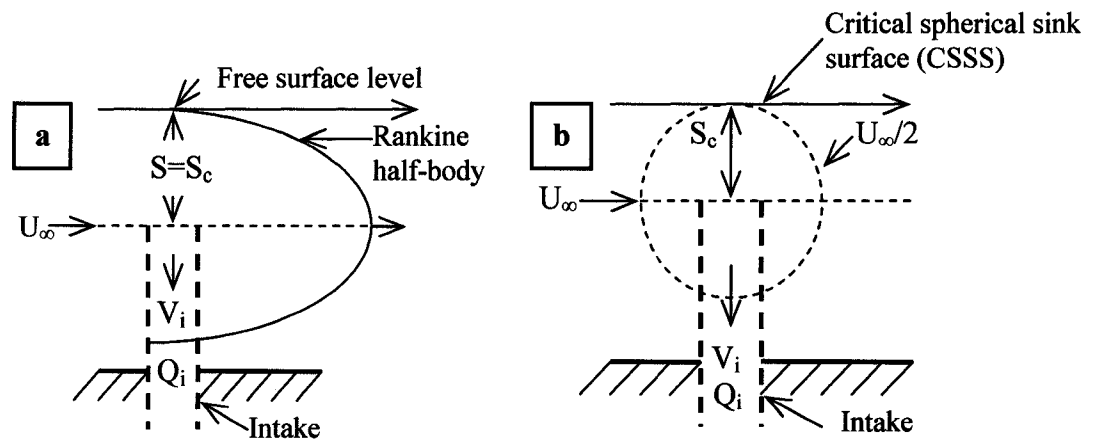


Figure 2.2: Critical submergence (a) representation of S_c (b) critical spherical sink surface [Yildirim and Kocabad, 1995]

Yildirim et al. [2000] continue the study of CSSS by investigating the flow boundary effects on the critical submergence of intake pipe. They defined ‘blockage’ as the loss in surface area of a complete CSSS, attributable to impervious flow boundaries or structures through which no flow is supplied to the intake. The authors quantified the blockage due to the intake pipe to be equal to the surface area of the spherical sector of the CSSS remaining inside the outer boundaries of the intake pipe where no flow is

supplied to the intake (see Figure 2.2b). By incorporating the effects of the intake pipe boundaries and impervious flow boundaries into the potential flow solution, several other CSSS equations were developed and experimental studies were conducted to validate their equations. They found that the effect of blockage of the intake pipe on the critical submergence may be neglected if the wall thickness is negligible. They further concluded that potential flow solution gives acceptable results if the distances of impervious flow boundaries to the centre of the intake are larger than or equal to the critical submergence. Based on these authors' conclusions, the effect of intake pipe blockage and that of surrounding model boundaries were disregarded in this study.

2.4 Three-Dimensional Study of Flow at a Hydraulic Intake

The majority of literature on three dimensional studies of intake flow has investigated the approach flow distribution within the pump intake for both cross-flow and no cross-flow conditions using experimental and numerical methods. Some of the computational fluid dynamics (CFD) approaches used over time include RANS and LES. However, the work of Marghzar et al. [2002] was different; they numerically simulated the flow at an asymmetric horizontal intake by developing a three dimensional model that solves Reynolds Average Navier Stokes (RANS) and turbulence closure equations. Their study identified the transition from the channel to the intake pipe and the vortices present at the free surface and solid bed of the geometry. The experimental results from LDA measurements on the model were later employed to validate their numerical code. Their results show that the asymmetric condition of the geometry creates stronger vortices at both free surface and sub-surfaces with the possibility of air-core vortex ingestion in the pipe. They affirmed that the flow pattern into the intake follows the body contour of the

geometry such that the spiral streamlines defining the flow pattern at the intake change directions due to the channel geometry and finally leaves through the intake pipe entrance.

The work of Chen et al. [2004] complement the study of flow field at an intake by researching how intake size, cap and shape influence intake ingestion of frazil ice in a cold climate. Their studies were conducted in a set of unique ice-tank experiments of a common intake configuration. The experiments were extended through numerical simulation by using a three dimensional model, U^2 RANS (Unsteady Reynolds-averaged-Navier Stokes) to solve the RANS equations. Their results show that the intake without cap draws water from a region extending almost semi-spherically out from the center point of the intake's rim. They also observed that an elevated cap placed above a water intake helps to isolate the intake from the upper levels of water and substantially reduce the intake ingestion of frazil during frigid-water conditions as shown in Figure 2.2. The technique used in extracting the three dimensional flow pattern in this study will be adopted in the 3-D study of flow into a hydraulic intake.

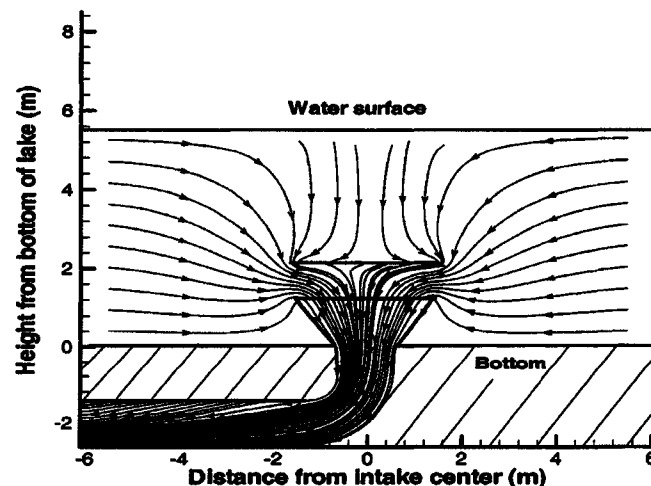


Figure 2.3: Streamline of velocity components with intake cap [Chen et al. 2004]

2.5 Evaluation of Literature

The review of existing literature shows that significant number of studies exist that focus on the hydrodynamic characteristics of flow around water intake structures and pump sumps. Some previous studies have utilized numerical and semi empirical models to explain the flow into a water intake, but at best, these have had to include various assumptions to favorably compare with experimental data. On evaluation, there are clear indications that though the intake submergence required for avoiding vortices at intakes for both cross-flow and no-cross-flow have been broadly identified, relatively little research has been conducted into the qualitative delineation of the withdrawal influence (entrainment envelope) of the hydraulic intake. This brought to light the scarcity of research in this area, it needs to be further explored, taking into consideration the current state-of-the-art measuring techniques and technologies that are available. The protection zone for surface water intakes need to be examined and accurately delineated since it is fundamental in determining the quality of raw water entrained by the intake. Further, it may provide insight toward resolving the operational difficulties encountered at intakes due to intake ingestion of debris and fragments. Therefore, this study is initiated to bridge the identified research gap and to provide applied contributions to the current environmental issues facing the hydraulic intake protection zone (IPZ).

CHAPTER 3

DELINEATION METHODS

In fluid dynamics, the relevance of various studies to field practical situations is determined by conducting tests on scaled models. A model in this regard is a scaled representation of a physical system that is used to predict the behaviour of the system. The physical system is usually referred to as the prototype while the analytical, computational and laboratory systems are usually thought of as models.

In this investigation, the hydrodynamic characteristics of the existing City of Windsor water intake structures situated in the Detroit River (prototype) were scaled appropriately in accordance with Froude number similitude (as required for models involving free surface flows). The concept of similitude herein is based on the idea that measurement or results obtained from the model can be used to describe the behaviour of the physical system. Three approaches were employed on the physical model to illustrate the entrainment envelope of an intake in a cross-flow. These include the laboratory experiments on scaled model, analytical potential flow study that offered the analytical solution and the computational solution via a finite volume solver for further comparison and validation of results.

3.1 Introduction of Prototype Geometry

The existing City of Windsor water intake structures consist of two different cylindrical shapes (circular and elliptical) with varying cross sectional area situated in Detroit River, through which the city withdraws water for its municipal water supply. According to previous investigation of the two hydraulic intakes by Carriveau [2004], the two intakes by model simplifications can be represented as identical circular pipes.

Figures 3.1a and 3.1b present the configuration parameters and the profile geometry of the circular intake pipe. The circular cross section is 2.44m in diameter and the intake transition from a circular face section to an elliptical pipe (d) is 1.22m x 1.52m. The submergence (measured as distance from intake surface to water elevation) of the intake is 8.23m. For the purpose of this study, the prototype is considered as a single circular hydraulic intake pipe situated in the river.

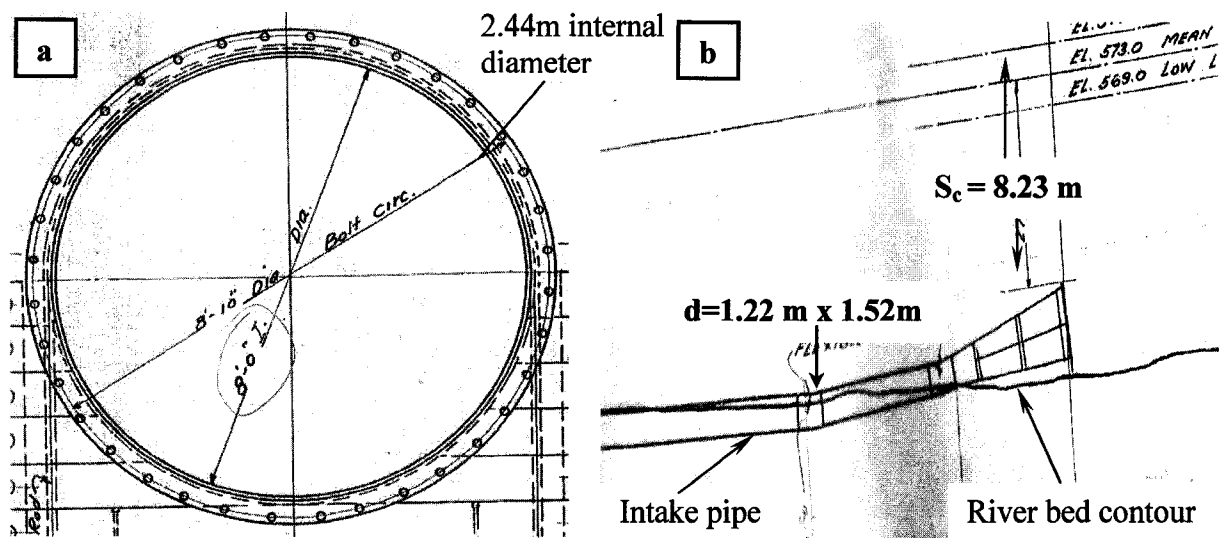


Figure 3.1: Prototype profile geometry (a) Intake face (b) Conical transition of intake configuration [Carriveau 2004]

3.2 Scaling Parameters and Model Assumptions

Flow processes involving a free-surface, as is the case in this study, are controlled predominantly by gravitational and inertial forces. In most cases, the viscous effects are relatively small and surface tension effects are deemed negligible but the relationship between the gravity and inertial forces defined as the Froude-similarity law is usually

preserved. Thus, the Froude number, defined as the ratio of inertia to gravitational force, is considered equal in both the prototype and the model.

$$F_r = \frac{F_m}{F_p} = 1 \quad (3.1)$$

where $F = \frac{V_i}{\sqrt{gd_o}}$, V_i = intake flow velocity, g = gravitational constant and d_o is a characteristic intake diameter.

In any laboratory setting, the model dimensions are typically governed by the lab apparatus available for testing. The same scenario occurred in this study, the length scale of model to prototype was determined based on the flume dimensions and commercially available pipe diameters. Using the geometric length ratio expressed in Equation 3.2 where L_r , L_m and L_p represent the length ratio, model length and corresponding prototype length, a length ratio of 1 to 125 was chosen for this study.

$$L_r = \frac{L_m}{L_p} = \frac{1}{125} \quad (3.2)$$

The prototype values of Detroit River acquired roughly 50 to 100 m upstream of the intakes were referenced from US geological survey - USGS [Holtschlag and Koschik 2002]. For each of the three delineation models, the essential prototype dimensions which includes the intake diameter, river velocity and intake withdrawal were modeled directly according to the Froude scaling laws while parameters denoted with an asterisk sign were determined by the spatial limits of the model and other relevant test conditions. These parameters include the model channel flow rate (Q_m^*) which is influenced by the reduced model width (w_m^*) and the intake penetration distance into the free stream (I_m^*) which was modified such that the ratio of intake penetration to free stream width was

approximately equal to that in the prototype. The scaling parameters for the experimental and numerical models are presented in Appendix A. The properties of water employed in this study are detailed in Appendix B.

The following assumptions were considered in solving this physical problem:

- (a) The hydraulic intake cylinder is infinitely long, thus the end effect is negligible.
- (b) The blockage effect caused by the intake pipe and impervious flow boundaries were considered to be insignificant.
- (c) The screen effect at the intake entrance was deemed negligible.
- (d) The effects of anti-vortex plate (used to prevent vortex effect) installed at the upstream and downstream of hydraulic intakes were considered inconsequential.
- (e) The thickness of the intake wall is assumed to be very small compared to the intake diameter.

3.3 Analytical Method: Potential Flow Analysis

The intake flow boundaries will be delineated analytically by considering potential flow theory. This theory has been applied extensively over the years to study the flow behaviour for relatively simple geometries. The flow into an intake pipe is approximated as a point sink, having the same centre and discharge Q_i as the intake. The channel flow is idealized as a uniform canal flow with velocity U_∞ flowing towards the positive x direction as depicted in Figure 3.2. The superposition of the uniform flow and the point sink produces the Rankine half-body (RHB) characterized by a singularity point. It is a shape that divides the flow into two regions, the flow area or streamlines entering the intake and flow area not entering the intake. This RHB intrinsically forms the entrainment envelope for an intake withdrawing from a perpendicular cross flow.

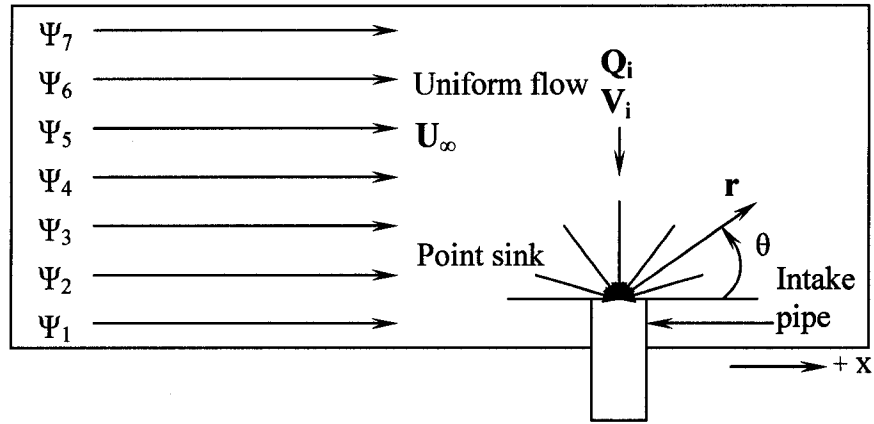


Figure 3.2: Potential flow representation of an intake

The theory of potential flow is governed by Laplace equation for irrotational, incompressible and inviscid flows. The inviscid term in this study refers to flow in which net viscous forces (viscosity) are negligible and the irrotationality condition signifies that the fluid particles around the intake are not rotating about their own axis. The Laplace equation is a linear homogenous differential equation, such that the linear combination of two solutions, ϕ_1 and ϕ_2 , must produce a third solution ϕ_3 . Equation 3.3 represents the 3-D Laplace equation in Cartesian coordinate system.

$$\nabla^2 \phi = \frac{\partial^2 \phi}{\partial x^2} + \frac{\partial^2 \phi}{\partial y^2} + \frac{\partial^2 \phi}{\partial z^2} = 0 \quad (3.3)$$

3.3.1 Two-dimensional flow

The combination of a 2-D uniform flow and a point sink flowing radially inward is depicted in Figure 3.3. The superposition of the Stokes stream function (ψ) for a uniform flow of a fluid with velocity U_∞ and the stream function of the point sink of strength Q_i at the origin yields the combined resultant stream function presented in Equation 3.4. In the figure, r is the radial distance from the centre of intake to the half-

body boundary, θ is the angle between horizontal axis x and radial direction vector, moving in a counter-clockwise direction from 0 to 2π radians and V_i is the intake velocity.

$$\psi = \psi_{uniformflow} + \psi_{point\ sink} \quad (3.4)$$

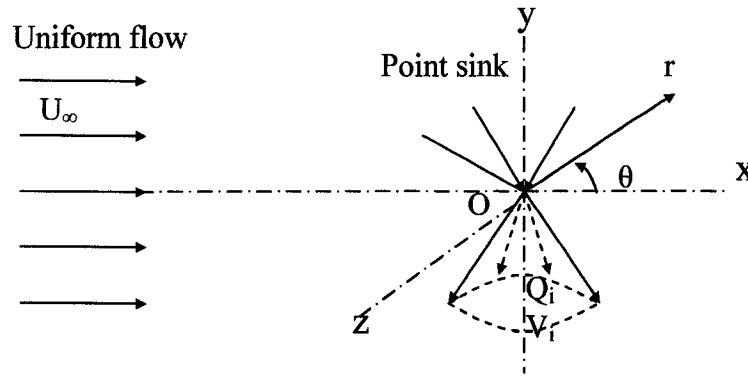


Figure 3.3: 2-D representation of uniform flow and point sink

The simplification of Equation 3.4 in terms of the defining parameters results in Equation 3.5 for the combined stream function. The equation of the stagnation streamline presented in Equation 3.6 for the Rankine half-body of revolution which divides the flow into two regions is obtained by considering the value of the stream surface at the stagnation point when $\theta = 0$ and $V_r = V_\theta = 0$ [Yuan 1967, White 2003].

$$\psi = U_\infty r \sin \theta - \frac{Q_i}{2\pi} (\theta) \quad (3.5)$$

$$y = r \sin \theta = \frac{Q_i}{2U_\infty} \left(1 - \frac{\theta}{\pi} \right) \quad (3.6)$$

where r is the radial distance from the centre of intake to the half-body boundary, θ is the angle between horizontal axis x and radial direction vector, moving in a counter-clockwise direction from 0 to 2π radians, U_∞ is the uniform canal flow velocity and Q_i is the intake discharge as represented in Figures 3.2 and 3.3 respectively.

3.3.2 Three-dimensional flow

The combined Stokes stream function for the uniform flow of a fluid with velocity U_∞ in the direction of the positive x -axis for three-dimensional axi-symmetric flow and the point sink is given by the expression in Equation 3.7 where the volume flow between any two stream surfaces along the stream function is a constant. From Figure 3.3, because the flow is axi-symmetric, there is no variation in the flow as z varies from 0 to 2π . Thus, the system reduces to plane polar coordinates where $x = r \cos\theta$, $y = r \sin\theta$ and $r = (x^2 + y^2)^{1/2}$ in Cartesian coordinate as shown in Figure 3.3 [Kirchhoff 1985]. For 3-D axi-symmetric flow, the resulting stagnation stream surface has a form of RHB of revolution as schematically depicted in Figure 3.4. The contour equation for the dividing stream surface which separates the flow into two regions is further expressed in Equation 3.8.

$$\psi = -\frac{Q}{4\pi} \cos\theta + \frac{1}{2} U_\infty r^2 \sin^2 \theta \quad (3.7)$$

$$r^2 = \frac{Q}{2\pi U_\infty} (1 + \cos\theta) \quad (3.8)$$

Similarly, r is the radial distance from the centre of intake to the half-body boundary, θ is the angle between horizontal axis x and radial direction vector, moving in a counter-clockwise direction from 0 to 2π radians, U_∞ is the uniform canal flow velocity, Q_i is the intake withdrawal rate and V_i is the intake velocity. As stated earlier, the outline of the stagnation streamline that forms the RHB delineates the region of flow that enters the sink. Thus, Equations 3.6 and 3.8 are solved analytically for five intake withdrawal rates to model the intake entrainment envelope.

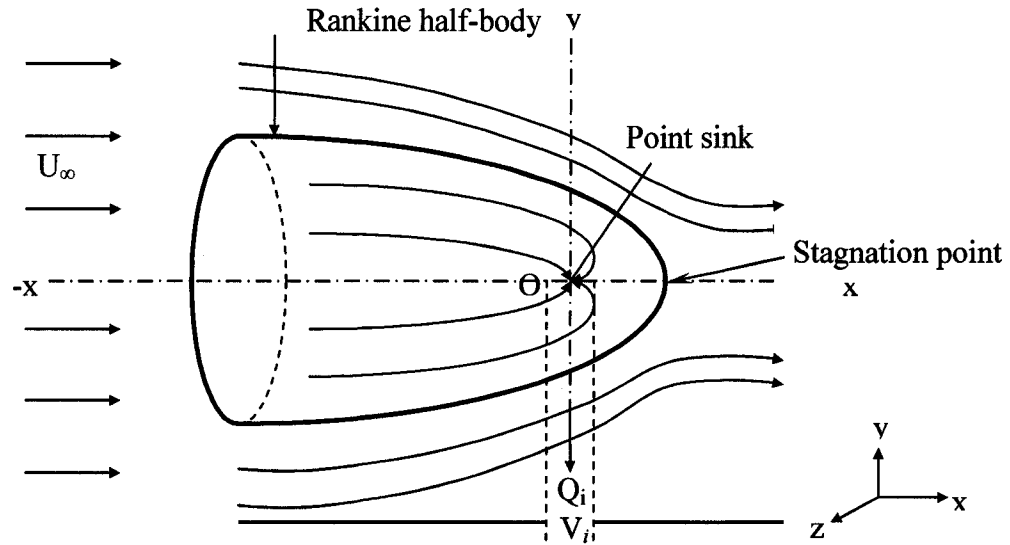


Figure 3.4: Representation of Rankine half-body of revolution.

3.4 Numerical Method

The numerical prediction of the fluid flow into a hydraulic intake involves the discretization of a set of transformed partial differential equations derived from the laws of conservation of mass and momentum over the computational domain of interest to yield a set of algebraic equations. The partial differential equation (PDE) resulting from the conservation of mass is known as the continuity equation while the systems of equations derived from the momentum balances are known as Navier Stokes equations. These equations with appropriate boundary conditions are sufficient to solve x , y and z components of velocity u , v , w and pressure p at any point for steady and unsteady incompressible flow. The 3-D continuity equation is stated in Equation 3.9 and Equations 3.10, 3.11 and 3.12 represent the x , y and z -direction momentum equations respectively.

$$\frac{\partial u}{\partial x} + \frac{\partial v}{\partial y} + \frac{\partial w}{\partial z} = 0 \quad (3.9)$$

$$\frac{\partial u}{\partial t} + u \frac{\partial u}{\partial x} + v \frac{\partial u}{\partial y} + w \frac{\partial u}{\partial z} = -\frac{1}{\rho} \frac{\partial p}{\partial x} + \frac{\mu}{\rho} \left(\frac{\partial^2 u}{\partial x^2} + \frac{\partial^2 u}{\partial y^2} + \frac{\partial^2 u}{\partial z^2} \right) \quad (3.10)$$

$$\frac{\partial v}{\partial t} + u \frac{\partial v}{\partial x} + v \frac{\partial v}{\partial y} + w \frac{\partial v}{\partial z} = -\frac{1}{\rho} \frac{\partial p}{\partial y} + \frac{\mu}{\rho} \left(\frac{\partial^2 v}{\partial x^2} + \frac{\partial^2 v}{\partial y^2} + \frac{\partial^2 v}{\partial z^2} \right) \quad (3.11)$$

$$\frac{\partial w}{\partial t} + u \frac{\partial w}{\partial x} + v \frac{\partial w}{\partial y} + w \frac{\partial w}{\partial z} = -\frac{1}{\rho} \frac{\partial p}{\partial z} + \frac{\mu}{\rho} \left(\frac{\partial^2 w}{\partial x^2} + \frac{\partial^2 w}{\partial y^2} + \frac{\partial^2 w}{\partial z^2} \right) \quad (3.12)$$

For two dimensional flow, the z-component of Equation 3.9 through 3.13 becomes zero and the time derivative term ($\frac{\partial}{\partial t}$) of the equations are zero for steady incompressible flow. The algebraic equations obtained from these partial differential equations are solved sequentially by an iterative method. The conversions of the differential equations into approximate equations are carried out using the control volume (CV) approach of the Computational Fluid Dynamics (CFD) code, FLUENT. The numerical scheme employed in this study is similar to that described by Tokyay and Constantinescu [2006] and it is in accordance with the FLUENT User's Guide [2005]. The CV based techniques first divide the computational domain into discretized control volumes using computational grid. The governing equations are integrated over individual CV to construct non-linear algebraic equations for the discrete dependent variables of velocities and pressures.

The solution algorithm for the non-linear algebraic equations involves the linearization of the discretized equations and solution of the resultant linear equation system to yield updated values of the dependent variables starting with a given initial value and boundary conditions. The update continues until the scaled relative difference between two successive iterations has been reduced below a user-set threshold.

3.4.1 Governing equation discretization

In reference to Section 3.4, this study employed the second order scheme which involves solving the second order terms of the Taylor series expansion of the PDE's for the velocity and momentum estimation. The scheme was referred to as the most accurate for laminar flow in FLUENT User's Guide [2005]. Initially, the solution procedure was initiated with the Semi-Implicit Method for Pressure-Linked Equation (SIMPLE) method of interpolation for pressure-velocity coupling for the segregated implicit solver. Then the SIMPLE-Consistent (SIMPLEC) method was employed on the same grid which resulted in quick solution convergence and ultimately improved the solution. The difference in the two methods may be as a result of the equations and significance of terms available in each method. Accordingly, the SIMPLEC method of interpolation was employed for all subsequent calculations. The second order interpolation scheme was then applied to calculate pressure. The details of these methods can be found in FLUENT User's Guide [2005].

3.4.2 Computational geometry and boundary conditions

The system of Navier Stokes equations was solved for incompressible inviscid and laminar hydraulic flow conditions with consideration for both steady and unsteady state. The 2-D and 3-D physical models were simulated as bounded flow as shown in Figures 3.5 and 3.6 respectively. The flow is described in a Cartesian coordinate system (x, y, z) in which x -axis is aligned with the inlet flow direction (streamwise direction); y -axis is perpendicular to the flow direction (cross-stream direction) generating a cross flow scenario and z -axis (spanwise direction) marks the geometry width for the 3-D case.

In Figure 3.5, the cylindrical intake pipe was represented in 2-D as a circle, bounded by the walls of a uniform approaching flow in a rectangular channel. The origin was centred at the middle point of the cylindrical pipe and the cylinder with diameter d_o was exposed to a constant channel velocity U_∞ from the entrance of the domain. The boundary conditions (BCs) defined the fluid flow variables at the various boundaries of the computational geometry. The velocity inlet BC was set at a far distance from the intake (an opening through which water enters the pipe) to mitigate an undisturbed flow; and was imposed at the domain inlet for all cases of the simulation. The inlet BC was located at an upstream distance of $x_u = 400d_o$, where d_o is the diameter of the intake. The channel exit (located at $x_d = 200d_o$) and the circular intake pipe exit were modeled as outflow BC. The top and bottom walls at distances (y_u) and (y_l) confining the domain were located at distance $150d_o$ from the intake centre.

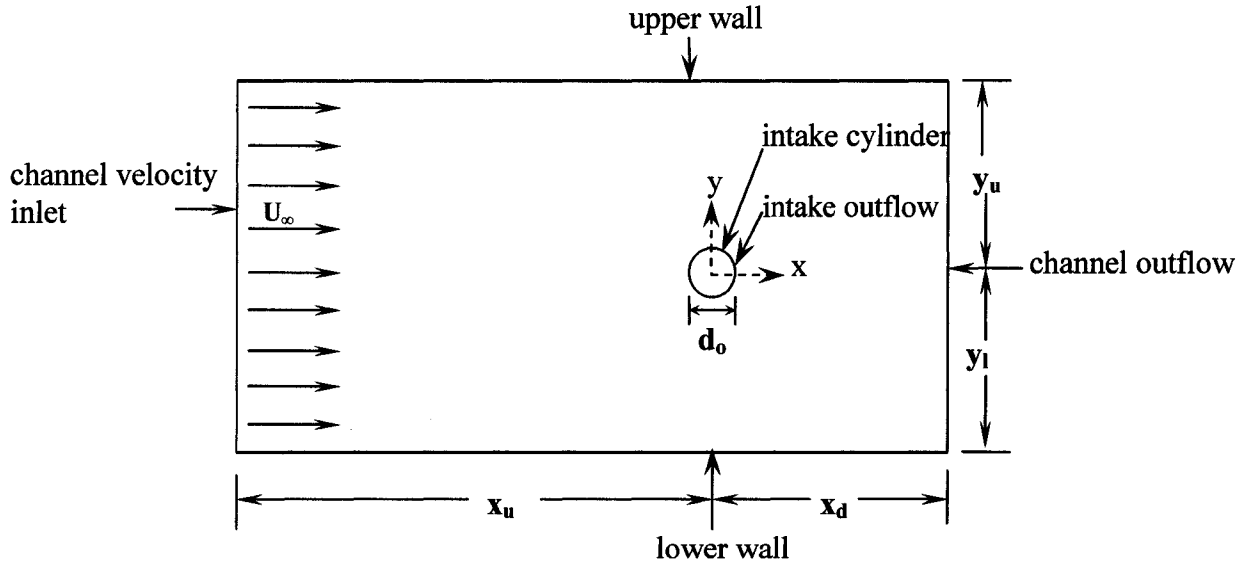


Figure 3.5: 2-D schematic of computational geometry (Plan view)

Figure 3.6 represents the 3-D geometry. The cylindrical intake pipe was positioned perpendicularly to the domain near-wall and it penetrated into the channel

flow at a distance of $25d_o$. Similarly, the velocity inlet BC was set at a distance of $x_u = 250d_o$ upstream of the intake pipe. The channel exit (located at downstream distance of $x_d = 200d_o$) and the cylindrical intake exit (the circular end that protruded into the flow) were modeled as outflow BC. The selected downstream distance of $200d_o$ in both geometries was considered appropriate to ensure fully developed condition at the exit for various intake discharges considered. These diameters surpass the upstream distance of $40d_o$, recommended for bounded flow and downstream distance of $55d_o$ to $60d_o$ suggested by many CFD users [Chen et al. 2004; Tokyay and Constatinescu 2006] for laminar flow. The standard slip and no-slip BCs were applied to the channel walls for the inviscid and laminar flow conditions respectively. For the scope of this study, the intake pipe was centrally located on the y-axis (equidistance of top and bottom wall) but further study should consider the effect of unequal wall distance on the physical problem.

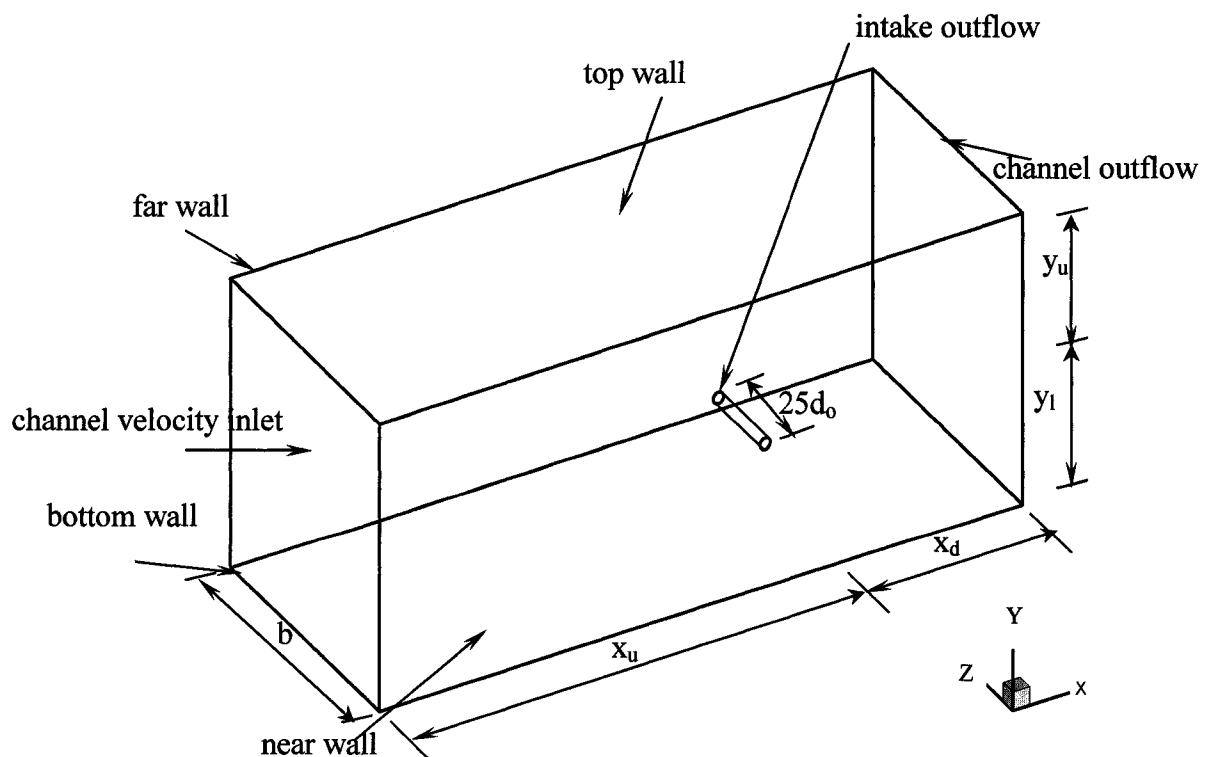


Figure 3.6: 3-D boundary conditions for computational geometry

3.4.3 Model discretization

The model geometry and the governing partial differential equations were discretized according to FLUENT User's Guide [2005] specifications before being solved. The geometry and the grid for the computational domain were created with Gambit processor, which is the grid generator part of the commercial software FLUENT. Gambit has a great deal of flexibility in construction of the geometry and can generate unstructured meshes with hybrid elements. Different meshing schemes were tested at the inception of the study using the unstructured triangular and quadrilateral mesh. The result shows that triangular meshes generate a fine resolution near the cylindrical intake surface which eased the transition from circular to rectangular channel structures. The successive gradient (change in size) from one element to another is minimal using triangular mesh and result into relatively faster convergence and zero skewness of the grid.

The detailed meshing scheme employed for the spatial discretization of the 2-D computational domain is shown in Figure 3.7 (a, b). The grid avoids rapid changes in the spacing of the cell near the solid cylinder surface. The smallest and largest cell gradient was maintained approximately at 0.002 and 0.1 respectively. The grid contained approximately 130000 to 150000 cells for the three intake diameters considered in this problem. Similarly, the 3-D geometry was discretized with unstructured triangular and tetrahedral pave mesh. The face components of the geometry were meshed using triangular grid while the entire domain (volume) was discretized using the tetrahedral pave mesh. Solutions were obtained on meshes consisting of up to 470000 to 600000 cells as illustrated in Figure 3.8(a). A section cutting horizontally through the centre of the intake pipe is presented in Figure 3.8(b).

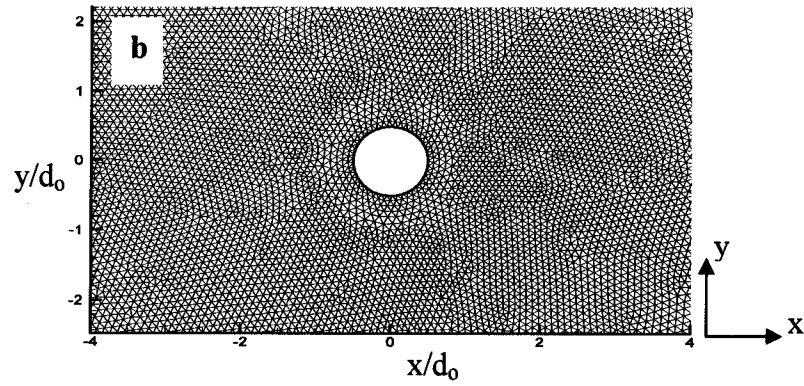
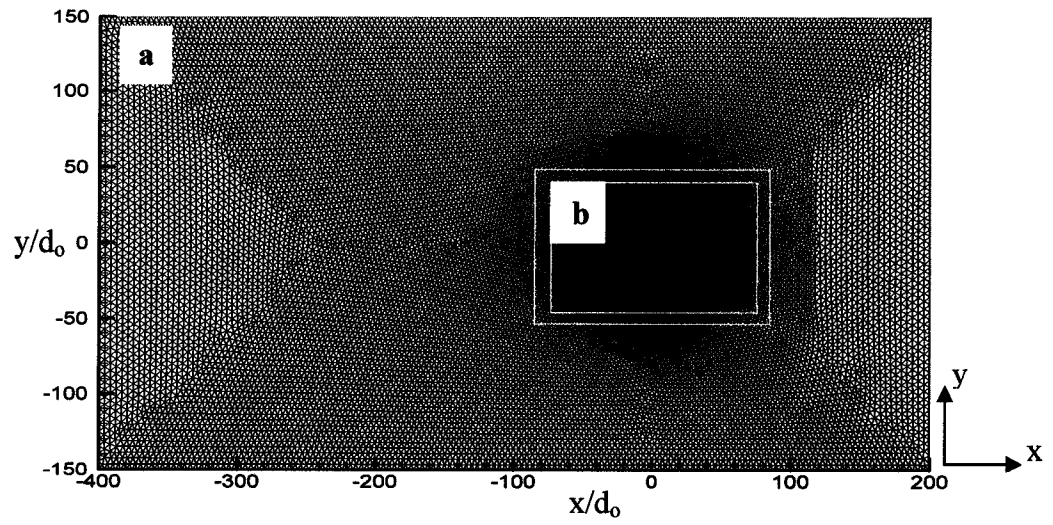
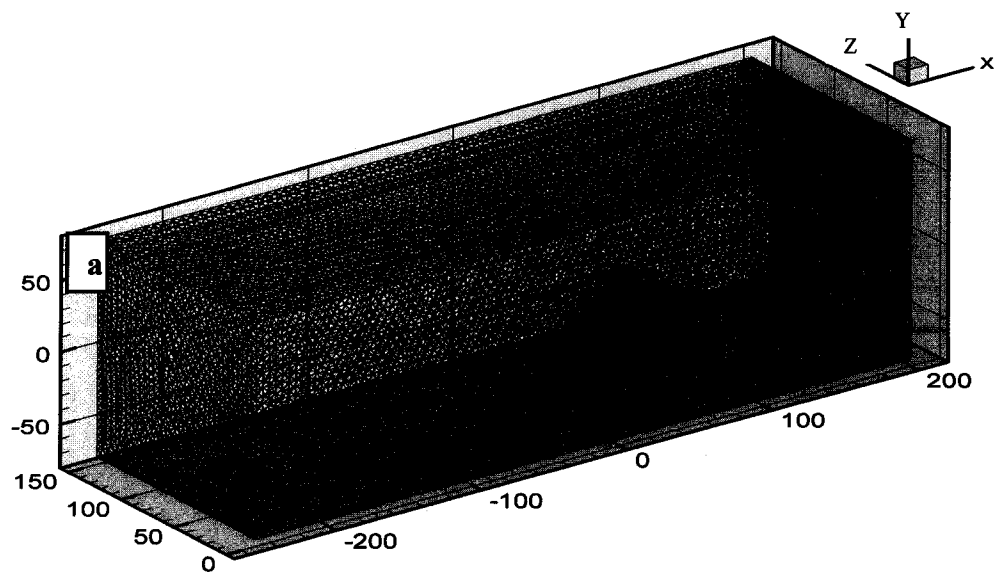


Figure 3.7: Typical grid for 2-D computational domain (a) full view; (b) zoomed view



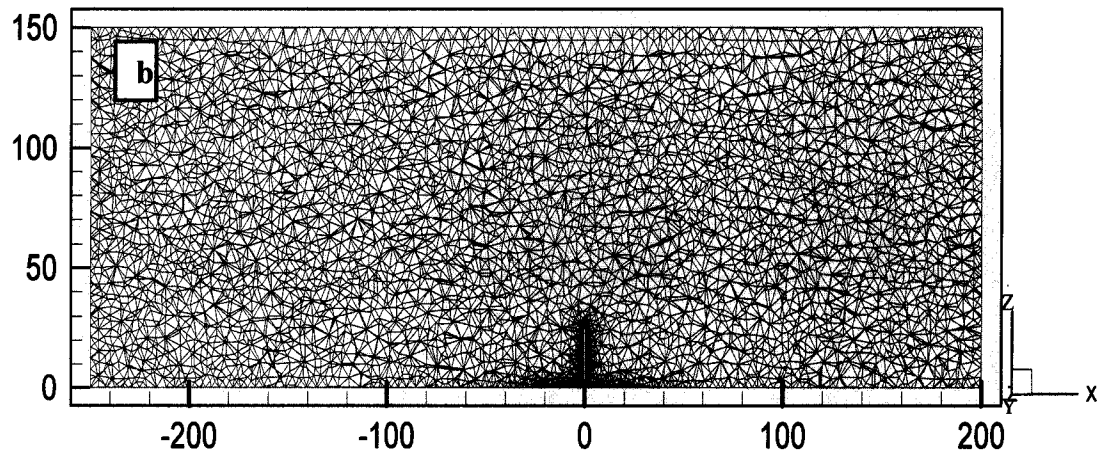


Figure 3.8: Typical computational mesh (a) full view of domain; (b) horizontal section of grid through the centre of the intake pipe

3.4.4 Discussion of convergence

In most CFD code, the model is considered solved when the cells in the domain are converged such that the residuals of the velocity components are reduced appropriately. The term residual refers to the change in the component values. With respect to the simplicity of the physical model studied and the second order scheme employed for the double precision segregated implicit solver, the residuals of the velocity components were first normalized by a factor of 1, which means dividing the residuals by the largest value during the first few iterations and they were subsequently reduced by approximately 5-6 orders of magnitude. The segregated implicit solver utilizes under-relaxation factors to control the updates of the computed variables at each iteration step; 0.20 to 0.30 and 0.60 to 0.70 were used for the pressure and momentum respectively as specified in FLUENT User's Guide [2005]. Converged solution was obtained at approximately 3000 to 75000 iterations for the 60 cases simulated. Appendix C details the convergence plots.

3.4.5 Grid independence

The accuracy of a CFD solution is governed by the number of cells used in the computational domain and the solution accuracy increases as the number of cells increases. Grid refinement study was carried out on four progressively refined grids based on the sophistication of the computational facilities: 70 x 20, 110 x 40, 150 x 60 and 170 x 70 where the nodes distributed over the intake circular surface are 55, 50, 45 and 40 respectively for the 2-D case. The meshed domain were smoothed and swapped in FLUENT to increase the efficiency of the grid as required for unstructured grids. The grid independency of two important parameters; depth of entrainment envelope H and vertical distance from the intake centerline to the envelope r_s (scaled by the intake diameter) is shown in Figure 3.9. The figure explains that the value of H and r_s were initially high and were subsequently reduced as the refinement progresses until further grid refinement results in insignificant effect on the parameters. Therefore, 150 x 60 (136895) cells were utilized for subsequent calculation.

Grid Convergence Index, recommended by the Journal of Fluids Engineering Policy [Celik 2004] was used to analyze the numerical error of important parameters in this study. The results and details of this analysis are presented in Appendix D.

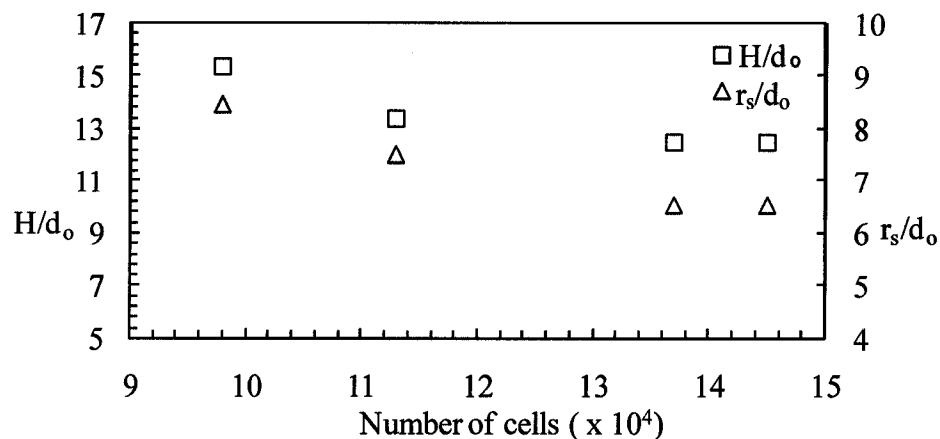


Figure 3.9: Grid independence of H and r_s of entrainment envelope

3.5 Experimental Model

Conducting scaled laboratory model test has become a routine practice to finding solutions to hydraulic flow problems and to validate results provided by other research approaches. In this study, an open channel flume was used for carrying out the study on the intake entrainment envelope located at cross flow. This delineation method was deemed necessary in order to validate the analytical and computational methods and most importantly, to observe the formation of the entrainment envelope via flow visualization. The experimental set up, procedure and the measurement techniques are described in this section.

3.5.1 Model description

The side view of the re-circulating open channel flume used in this study is schematically depicted in Figure 3.10. The main component of the flume is a rectangular channel 15m long, 0.7m deep and 0.98m wide. The intake pipe was located perpendicularly to the false wall, 5.2m from the flow entrance. The false wall was incorporated because of the restriction imposed by the flume. All the walls of the flume were made of transparent acrylic to allow visual observations and the passage of laser light. The energy dissipating screens and rafts located at the entrance of the flume helped to mitigate circulation and non-uniformity. The discharge entering the flume was measured by means of a digital flow monitoring system, which was kept constant at $0.02\text{m}^3/\text{s}$ for all the test measurements. The discharge was further validated by measuring the channel velocity with Laser Doppler Anemometer. Accordingly, the channel water depth was fixed at a constant value of 0.45m. The water entering the intake pipe was controlled by valve and calibrated flow meter was used to achieve the desired discharge

at the intake. Aluminum intake pipe with constant diameter of 0.02m was used for the study. In addition, the following conditions were set for the study in relation to the scaling parameter discussed in Section 3.2; the intake penetration I_m into the free stream was 0.45m, the intake clearance c_m from the floor of the flume to the intake centerline was 0.22m, the intake submergence ($S_m = h/d_o \gg S_c$) which refers to the dimensionless ratio of the depth of water above the intake mouth to the intake diameter was 0.21m and the free stream velocity U_∞ at the flume entrance was 0.05m/s. Figure 3.11 shows a pictorial view of the model set-up.

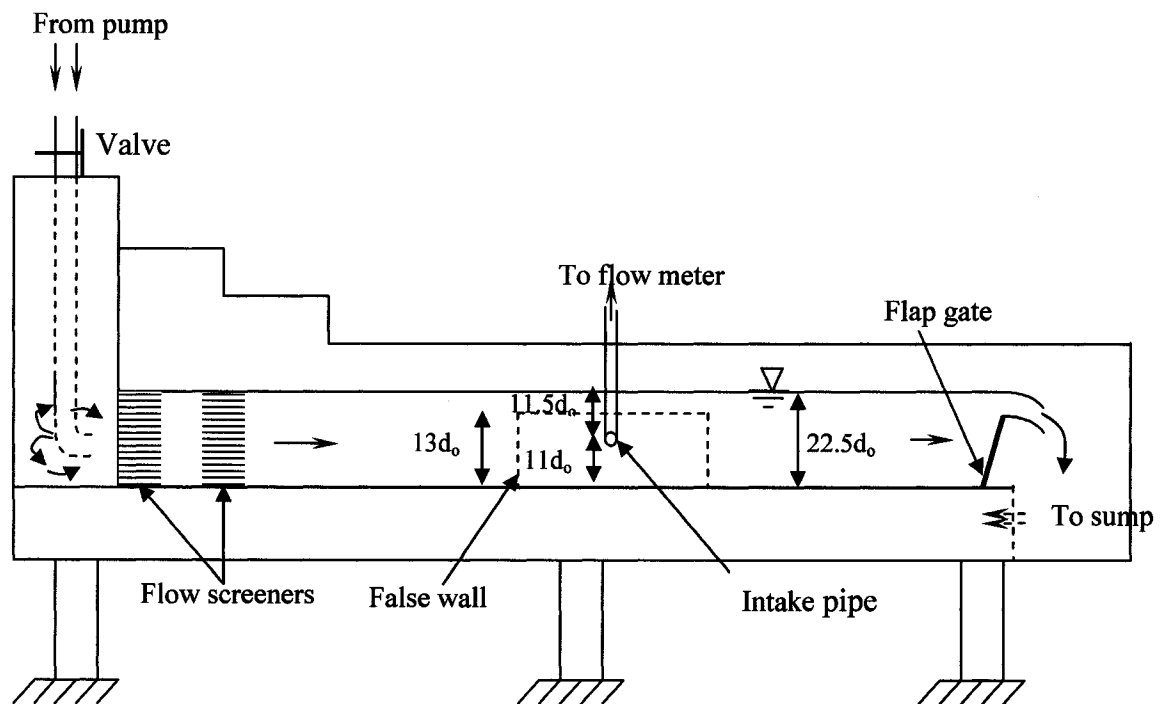


Figure 3.10: Experimental setup (not drawn to scale)

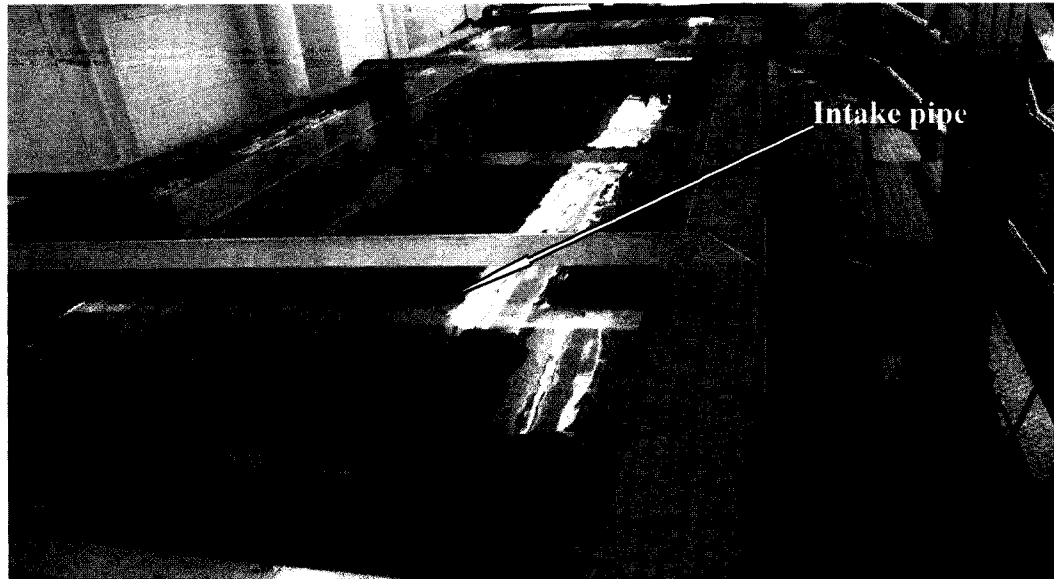


Figure 3.11: Laboratory flume set up for intake entrainment envelope study

3.5.2 Experimental procedure

The experimental procedure consisted of initially filling the flume with water to a depth of $22.5d_o$ (0.45m) by adjusting the tail-gate located at the downstream end of the main channel and gradually adjusting the pump power and valve in the water-supply line until the desired discharge and corresponding flow velocity in the main channel was obtained. Water was then withdrawn through the intake pipe and the valve controlling the discharge in the suction pipe was adjusted repeatedly until the desired intake discharge was obtained for each case. Due to the laboratory model constraints in terms of location, available experimental equipments and commercially available pipe diameters, three cases of intake discharges (out of five) were tested. After the flow in the model became steady and established, the streamwise and crosswise mean velocities were taken with Laser Doppler Anemometer at various locations upstream and downstream of the intake pipe to delineate the envelope. The flow pattern into the intake was visualized by dye injection and was captured on video.

3.5.3 Measurement technique

The Laser Doppler Anemometer (LDA) is a widely accepted tool for measuring the flow velocity. The LDA has to its advantages the non-intrusive measurement principle, high spatial and temporal resolution. This study explores two-dimensional velocity data systematically acquired within the intake region of influence using a single-component fiber-optic LDA manufactured by Dantec Measurement Technologies Inc. The LDA system was powered by 300mW argon-ion laser and the optical system include a Bragg cell, a beam expansion unit and a 500mm focusing lens. The LDA system was operated in backward scatter mode. The measuring volume for the present configurations was $0.124 \times 0.123 \times 1.65 \text{ mm}^3$. Due to refined screen located at the channel entrance, there were insufficient particles in the water; therefore an artificial seeding (solid tracer particles of size $2 \text{ }\mu\text{m}$) was used for all the experimental runs. As a result of the restrictions imposed by the geometry of the transmitting optics, the intake pipe material and the channel support structures, no measurement were possible at locations closer than a perpendicular distance of $0.25d_o$ ($\approx 5\text{mm}$) from the intake pipe entrance. The fiber optic probe, mounted on a two-dimensional stepper motor driven traversing mechanism is capable of repeatedly attaining the same location with an accuracy of $\pm 0.01\text{mm}$. Thus, measurements were conducted at a vertical plane $0.25d_o$ from the intake entrance at various horizontal and vertical distances ($1d_o$ apart) around the intake influence region with the attempt to observe the velocity field variation. Figure 3.12 shows the sketch of planar measurement grids used to sample a total of 121 points.

A statistical uncertainty analysis was conducted at 95% confidence level for the mean velocities (u and v). The result and detail of this analysis is presented in Appendix E.

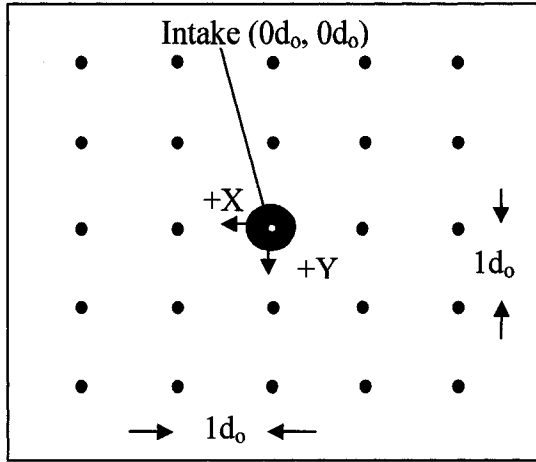


Figure 3.12: Sampling grid for experimental model

3.6 Testing Program

A summary of the tests is presented in Table 3.1. Five intake discharges (Q_i) with intake diameter d_o was modeled analytically and is presented as Test A. These intake discharges (Q_i) are denoted as Case 1 to Case 5 in this study. As a result of the mathematical singularity solution of the Rankine half-body which is based on point sink consideration (rather than intake diameter) in potential flow theory; attempt was made to numerically simulate the point sink by subsequently reducing the intake diameter d_o to refined intake diameters. The refined intake diameters (d_r) were quantified as a function of the intake diameter (d_o), that is, $d_r = t(d_o)$ where t is 100%, 10%, and 1%; r is 1, 2 and 3 for the three diameters. Thus, the three refined intake diameters tested are $d_1 = 100\%(d_o)$, $d_2 = 10\%(d_o)$ and $d_3 = 1\%(d_o)$ and are denoted as Test A, B and C respectively.

It should be noted that the change in the value of the intake diameter (d_o) to accommodate the other two tests (B and C) has no effect on the geometry size and all measurements were scaled with the intake diameter (d_o). Hence, Tests A, B and C were solved numerically using the proportion (Q_i/Q) of flow drawn into the intake from the

total flow (Q) in the channel as required by FLUENT. Limited experimental modeling of three intake discharges (out of five) of Test A was possible because of the restriction from the available laboratory apparatus. These cases were tested twice to ensure repeatability and further validation of flow features.

In general, the physical model was studied at intake Reynolds number ($Re = V_i d_o / \nu$) of $1.4e^4 \leq Re \leq 7.9e^6$ and Weber number ($W = \rho V_i^2 d_o / \sigma$) of $800 \leq W \leq 5000$ where V_i is the intake velocity, d_o is the intake diameter, ν is the kinematic viscosity and Γ is the circulation. These ranges confirm that the inertia force introduced by the uniform flow dominates the viscous, surface tension, centrifugal and gravity forces [Padmanabhan and Hecker, 1984]. In Table 3.1, Q_i is the Intake discharge, Q is the total channel flow rate, Q_i/Q is equivalent to the proportion of flow drawn into the intake from the total flow in the channel, d_r is the refined intake diameter and d_o is the intake diameter.

Table 3.1: Summary of test conditions

TEST	Cases	Q_i ($\times 10^{-3} \text{m}^3/\text{s}$)	Q_i/Q ($\times 10^{-3}$)	d_r
A	Case 1	5	17	$1d_o$
	Case 2	15	50	$1d_o$
	Case 3	25	83	$1d_o$
	Case 4	75	250	$1d_o$
	Case 5	125	417	$1d_o$
B	Case 1	5	17	$0.1d_o$
	Case 2	15	50	$0.1d_o$
	Case 3	25	83	$0.1d_o$
	Case 4	75	250	$0.1d_o$
	Case 5	125	417	$0.1d_o$
C	Case 1	5	17	$0.01d_o$
	Case 2	15	50	$0.01d_o$
	Case 3	25	83	$0.01d_o$
	Case 4	75	250	$0.01d_o$
	Case 5	125	417	$0.01d_o$

CHAPTER 4

RESULTS AND DISCUSSION

The results presented in this chapter focused on delineating the region of flow that provides water to the intake using three approaches. Emphasis will be on documenting the relevant differences in the intake entrainment envelope as the intake withdrawal rate increases. The most effective way of explaining results is by way of comparing and contrasting. Hence, some sections of this chapter will concentrate on comparing the analytical, numerical and experimental results; and their roles in delineating the entrainment envelope for the two flow conditions; inviscid and laminar flow.

The flow field around a hydraulic intake can be accurately defined by examining the actual trajectory of a fluid particle as it traverses in the flow. This process is defined as the particle pathline. Usually, the path of a fluid particle follows a particular streamline because the velocity vectors are invariant with time (for steady flow). Streamline as defined in Chapter 1, is the line drawn tangent to the velocity vector at each point in the flow field. They are lines that are everywhere parallel to the flow. Therefore, in the interest of delineating the entrainment envelope, streamlines and flow velocity vectors were used to analyze the flow, which consequently produce the stagnation stream surface for the radial flow field considered. The outline of this chapter is as follows. The first section illustrates the parameters defining the entrainment envelope. It gives a clear picture of the purpose of the research work and other flow features observed during the course of the study are tailored towards establishing their effects on these parameters. Second section discusses the two-dimensional flow condition. This includes the analysis of the analytical, inviscid and laminar numerical results and the experimental

measurements for the same test conditions. From the reviewed literature [Yildirim et al. 1995, Carriveau et al. 2002], it was established that the potential flow theory gives a good prediction of the flow into an intake. Hence, the potential flow solution forms the basis for comparing the results of these approaches. The effect of singularities on numerical result is also evaluated. Following this, an estimate of the numerical errors on the defining parameters (see Figure 4.1) is provided. In the third section, the three-dimensional results were analyzed and discussed for both flow conditions. Finally, the engineering significance of the study is detailed to complement the Intake protection Zone (IPZ) project from which the motivation of this work is drawn.

4.1 Entrainment Envelope Delineation Criteria

The recommended criteria for defining the maximum depth and width of an intake flow boundary were determined by considering the functional relationship involving the intake entrainment envelope and its influencing variables. The application of dimensional analysis to the influencing variables yields

$$\frac{H}{d_o} = f\left(\frac{U_\infty}{V_i}, \frac{D}{d_o}, \frac{r_o}{d_o}, \frac{r_s}{d_o}\right) \quad (4.1)$$

Equation (4.1) is schematically depicted in Figure 4.1 in which H = asymptotic width of the intake entrainment envelope; D = asymptotic depth of the intake entrainment envelope (not shown in the figure); U_∞ = free-stream velocity of the uniform canal flow at the upstream of the intake; V_i = intake flow velocity; d_o = diameter of the intake pipe; r_o = radial distance above the intake centre to the envelope, r_s = horizontal distance from the intake centre to the rear stagnation point or to the envelope boundary and Q_i is the intake discharge. The parameters H , r_s and r_o , scaled by the actual intake diameter (d_o) are the

functional variables defining the entrainment envelope. Considering the ideal assumption of intake cylindrical flow symmetry about the intake's axis for both inviscid and laminar flow conditions, the flow pattern on opposite sides of the intake are mirror images of each other, hence the defining parameters are measured towards the positive cross-stream (y) axis.

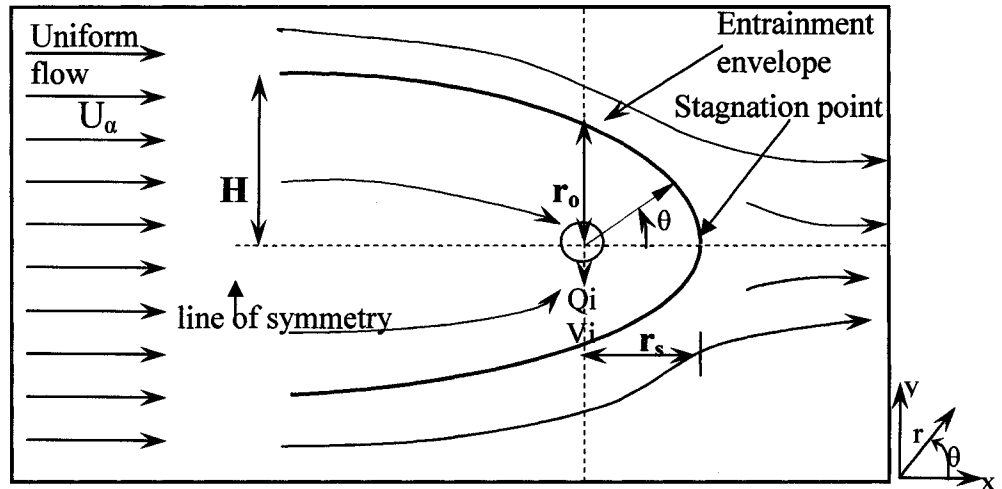


Figure 4.1: Schematic of entrainment envelope delineation criteria

4.2 Two-Dimensional Flow Solution

The results presented herein represent the 2-D analytical, numerical and experimental analyses. It is imperative to mention that all data obtained and mentioned herein are asymptotic values. For the analytical solution, Yildirim and Kocabas [1995] mentioned that the change of radius of Rankine half-body of revolution is negligible for $\theta > 90^\circ$ (see Figure 4.1). Therefore, the maximum width of the RHB occurs at $\theta = 0$ and at x tends to negative infinity. As a result, all numerical figures presented in this section are truncated for geometric similarities with analytical figures but numerical data are obtained at asymptotic condition.

4.3 Potential Flow Solution of Two-Dimensional Flow

The following figures illustrate the potential flow solution of an intake in a cross-flow for five intake discharges/cases (Test A in Table 3.1). Figure 4.2 shows the symmetrical stagnation streamlines for Case 1. Inspection of the figure revealed that the channel flow is from right to left and the intake withdrawal is perpendicular to the channel flow. The stagnation streamlines split the channel flow into two regions, the region that is drawn into the intake and the region that is not drawn into the intake. This confirms with the reviewed literatures that only the region around the flow provides water for the hydraulic intake [Chen 2004]. The maximum width H of the entrainment envelope obtained is $2.5d_o$ from the intake centre line which means that flow within the envelope will enter the intake and flow beyond the envelope will pass the intake without being entrained. Alternatively, flow passing at perpendicular distance, $H \geq 2.5d_o$ will flow downstream. Parameters r_o and r_s are measured to be $1.25d_o$ and $0.80d_o$ accordingly.

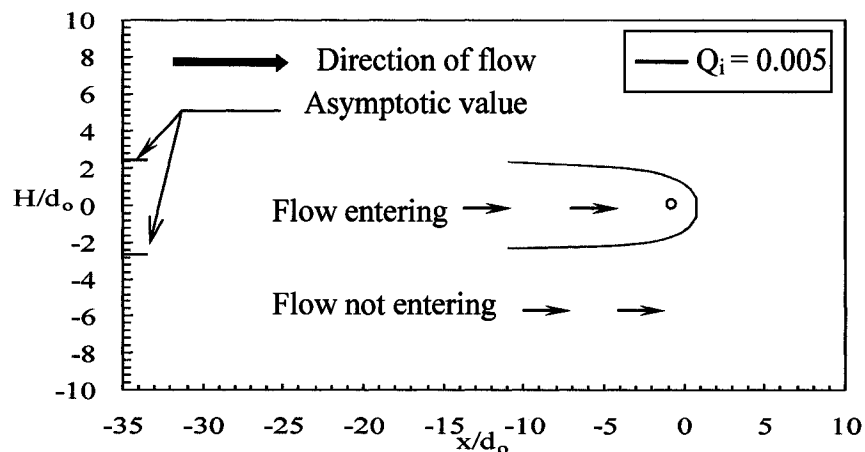


Figure 4.2: 2-D potential flow result for intake discharge - Case 1

Figure 4.3 presents the result for Case 2. The entrainment envelope H asymptotically approaches $7.5d_o$ while r_o and r_s are equal to $3.75d_o$ and $2.39d_o$

respectively. The differences in these values reveal that the potential for entrainment depends on the intake withdrawal rate, that is, the envelope size increases as the intake withdrawal rate increases. As it is, the flow within the entrainment envelope ($H \leq 7.5d_o$) will be drawn into the intake while any flow particles outside this region will flow downstream of the intake.

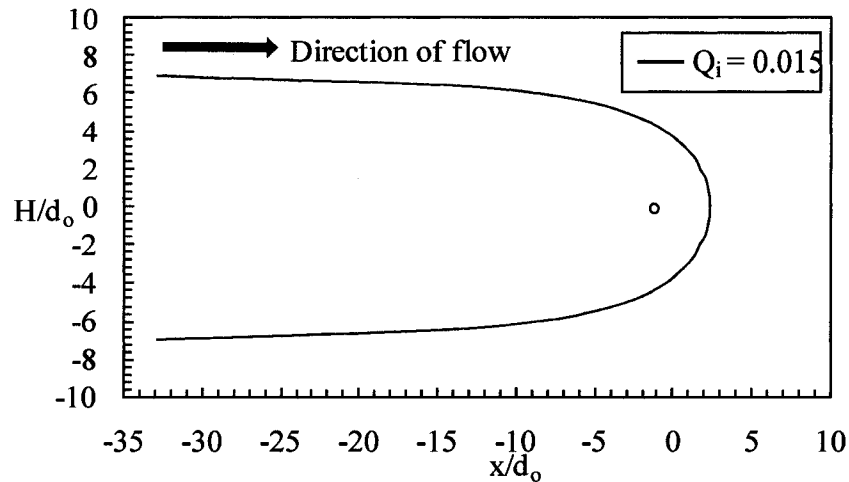


Figure 4.3: 2-D potential flow result for intake discharge - Case 2

Figure 4.4 represents the solution for the five intake discharge cases of Test A. The figure clearly made evident the dependence of the entrainment envelope size on the intake withdrawal rate. Case 5, that is, the highest withdrawal rate has the largest potential for entrainment with a width of $62.5d_o$ while Case 1 has the lowest potential for entrainment. The value of r_o and r_s also increased as the intake discharge rate increases. Figure 4.5 compares the entrainment envelope parameters for the intake discharges (Cases 1-5). The figure agrees with the direct proportionality trend between the intake discharge and the entrainment envelope defining parameters (H/d_o , r_o/d_o , r_s/d_o). That is, as

the intake withdrawal rate increases, the zone around the intake to be protected increases.

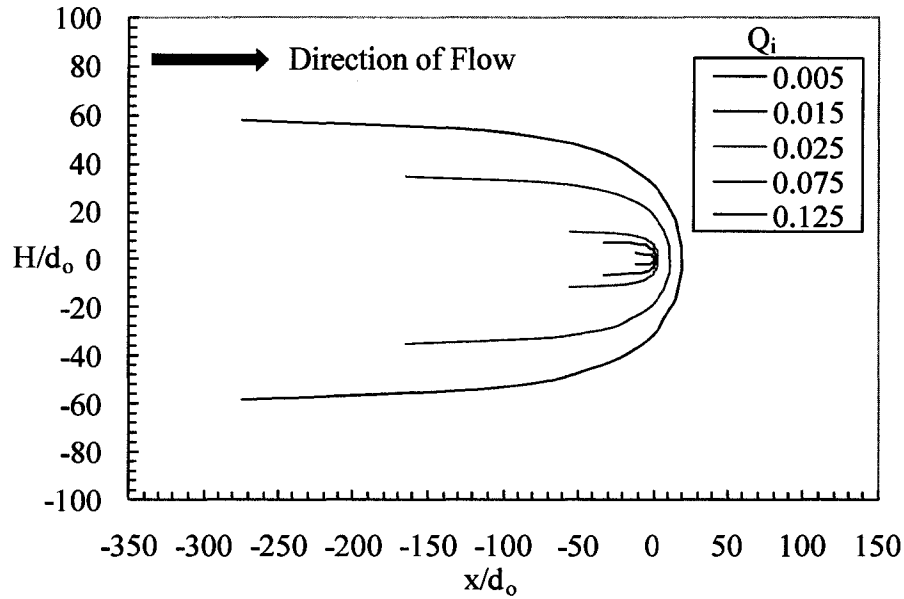


Figure 4.4: 2-D potential flow result for intake discharges (Cases 1 – 5).

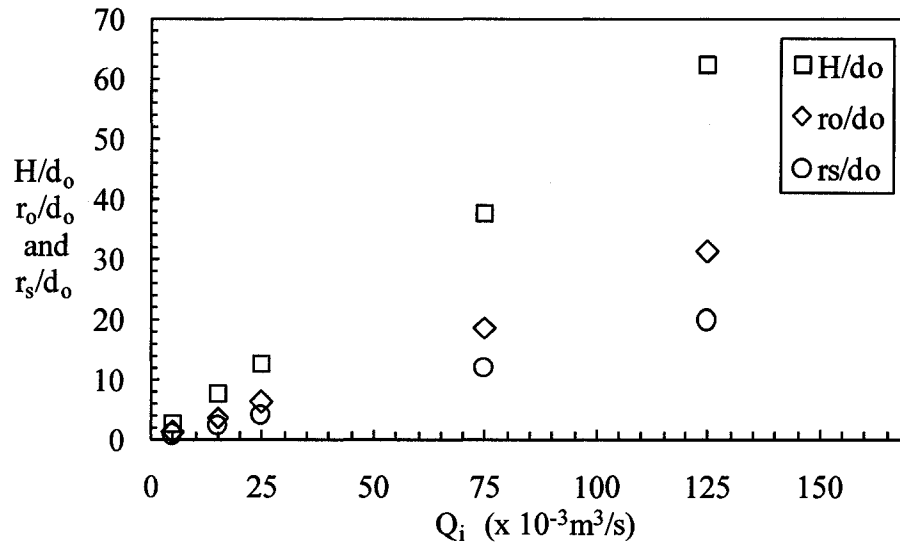


Figure 4.5: Effect of intake discharge on the entrainment envelope parameters

4.4 Numerical Solution of Two-Dimensional Flow

The computational solution of the physical model involves detailed analysis of three tests, Tests A, B and C for both inviscid and laminar flow conditions. These tests

were conducted numerically in an attempt to validate the singularity (point) effect of the potential flow theory. The results herein are presented by comparing the three tests result with the potential flow solution for both flow conditions. The specific test with extreme proximity to the potential flow solution for each flow condition is set out for further analysis.

4.4.1 Flow field for inviscid flow condition

The inviscid condition of the flow reveals the flow behaviour into and around a hydraulic intake of a frictionless fluid as detailed in Figure 4.6. The flow patterns into the hydraulic intake for the lowest intake discharge, Case 1 of Tests A, B and C are illustrated in Figures 4.6a, 4.6b and 4.6c. The symmetric nature of the flow shows that water is drawn directly downwards and towards the intake from around the intake, including the regions above, below and to the sides of the intake. The channel flow is sectioned into two regions in each case; the entering region and non-entering region. Flow passing below ψ_1 to the intake centre will enter the intake while flow passing above ψ_1 will not be drawn into the intake. It was also revealed that the width of the entering region increases as the intake withdrawal rate increases. Similar flow behaviour was observed in the subsequent intake discharges. Case 3 and Case 5 are presented in Figure 4.6d to 4.6i for validation purposes (note the difference in scale for each case).

The results were further analyzed to define the stagnation streamlines that represent the intake entrainment region. These stagnation streamlines were superimposed as shown in Figure 4.7 (a, b and c) in order to observe the differences in the width of the entrainment envelope. Close consideration of Case 1 shows that the asymptotic width (H) of the passing flow withdrawn into the intake is $2.6d_o$ for Test A and the value varies

significantly to $2.83d_o$ and $2.3d_o$ for Tests B and C respectively. This difference in envelope width was found to occur in all the intake discharge cases studied. Further inspection of the figures revealed that the largest envelope corresponds to the highest intake withdrawal rate and vice versa for each of the test.

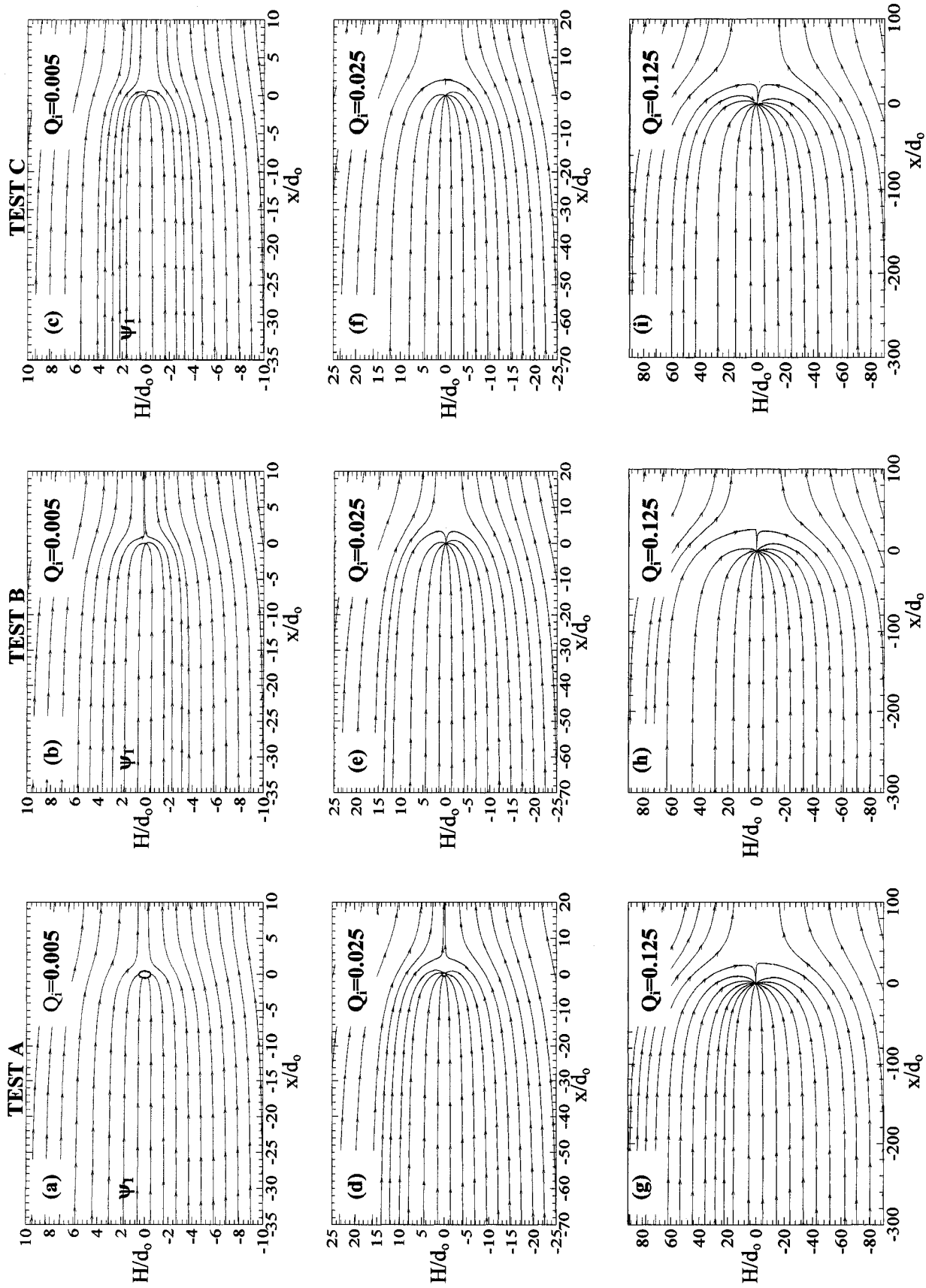


Figure 4.6: Flow patterns of inviscid flow for Case 1 ($Q_i = 0.005$), Case 3 ($Q_i = 0.025$) and Case 5 ($Q_i = 0.125$)

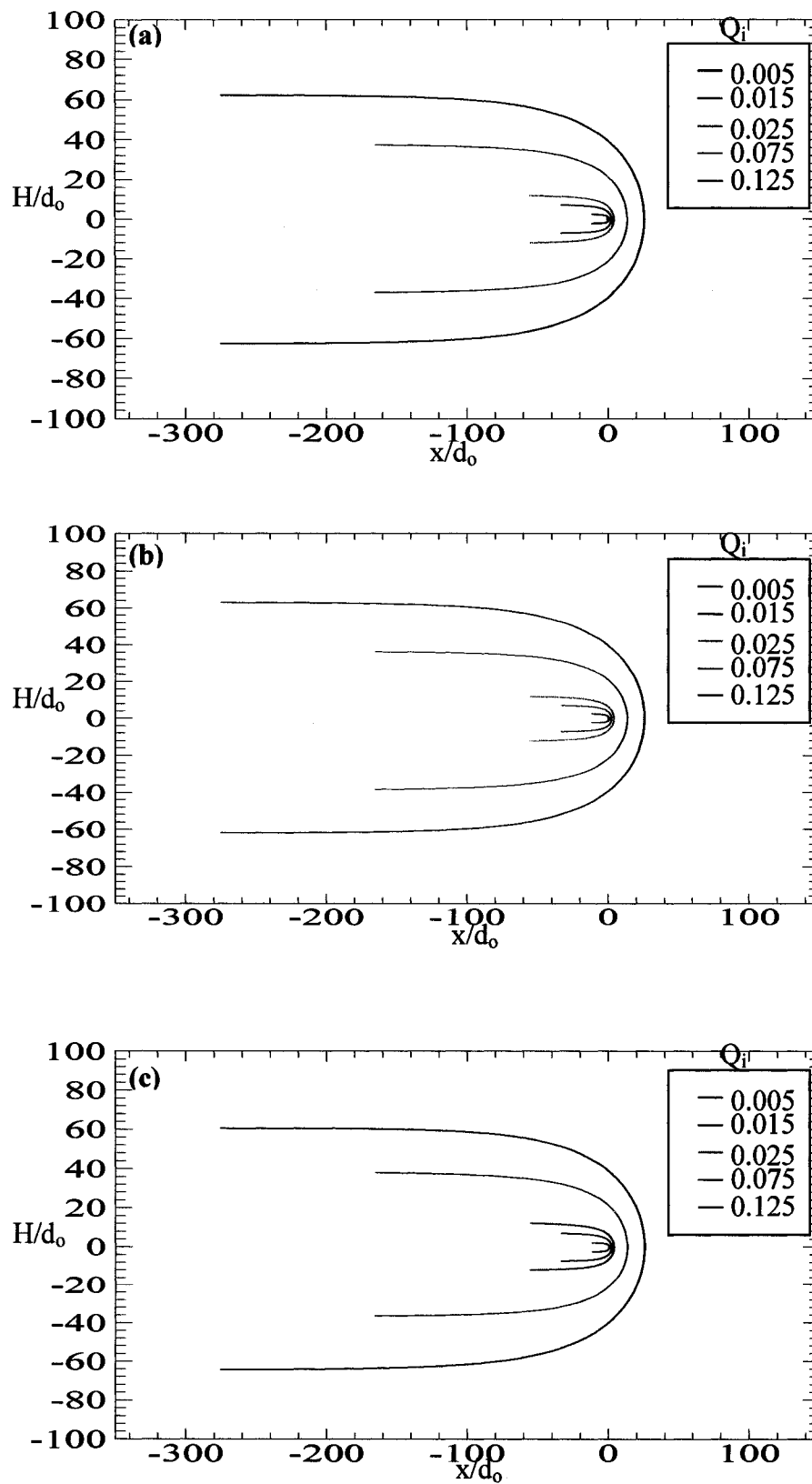


Figure 4.7: Stagnation streamline plots of inviscid flow; (a) Test A (b) Test B and (c) Test C

4.4.2 Comparison of inviscid data to potential flow theory

A detailed evaluation of the numerical inviscid results (Tests A, B and C) was conducted since the initial comparison in Figures 4.6 and 4.7 convey the difference in the parameters defining the entrainment envelope and to evaluate the likely influence of the mathematical singularity on the results. The contrast was estimated by comparing the numerical inviscid results (Figure 4.6) with the potential flow (analytical) solution (Figure 4.4) for the five intake discharges (Cases 1-5). Figure 4.8a summarizes the differences in the width of entrainment envelope by plotting the intake withdrawal rate (normalized by the total flow Q in the computational domain) against the entrainment envelope width. It is clearly evident from this figure that the inviscid solution of Test A is in good agreement with the potential flow analytical solution and the extent of agreement was quantified to be an average of 0.3%. Furthermore, the figure confirmed that subsequent reduction of the intake diameter to $0.1d_o$ (Test A) and $0.01d_o$ (Test B) results in varied entrainment envelope width characterized by loss of symmetry of the envelope as illustrated in Figure 4.8b.

The symmetry loss was calculated by measuring the positive and negative width of the entrainment envelope to the line of symmetry, the complete dataset is contained in Appendix F. Figure 4.8b confirms the agreement of Test A with the analytical result by exhibiting close up to the line of symmetry.

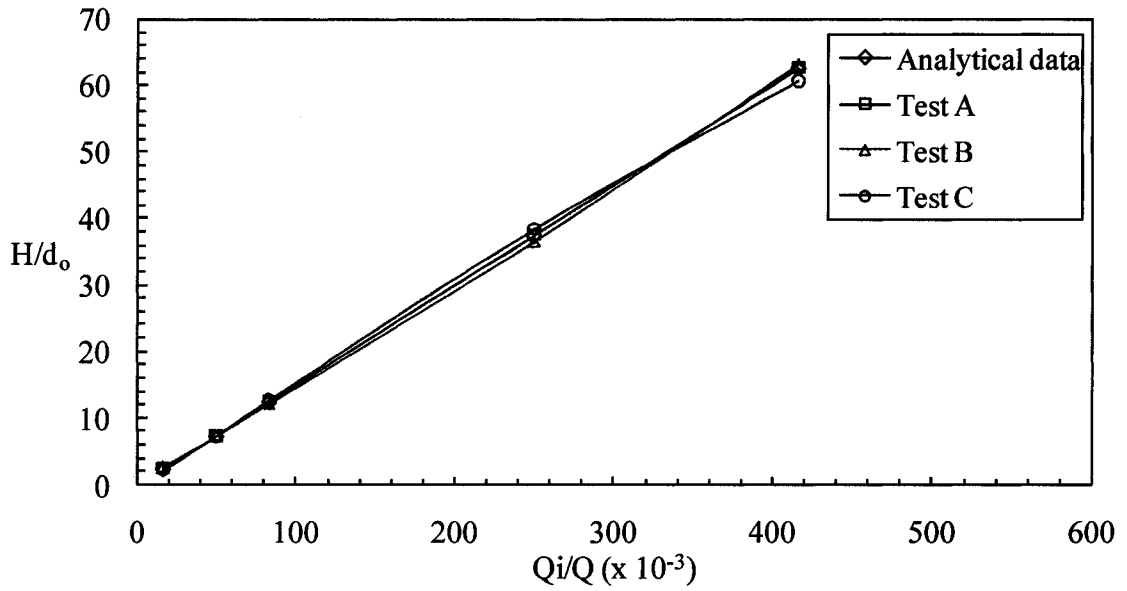


Figure 4.8a: Analytical data comparison to numerical inviscid result for H

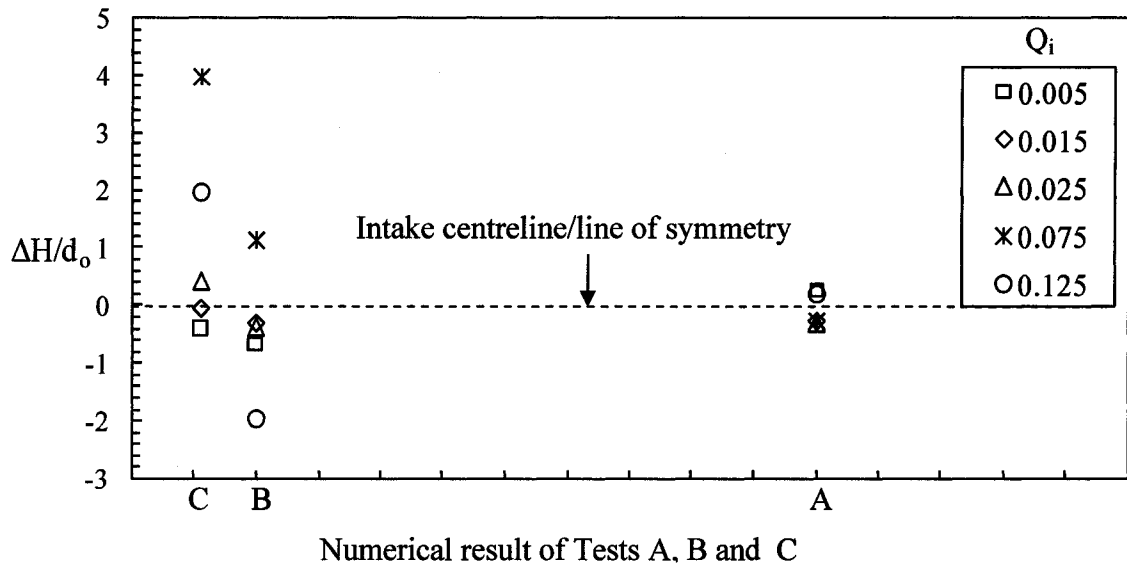


Figure 4.8b: Influence of singularity on numerical inviscid solution of Tests A, B and C

The disparity in the radial distance from the intake centreline to the envelope, r_o (plotted on the left vertical axis) for the three numerical inviscid tests (Tests A, B and C) and the analytical solution is illustrated in Figure 4.9. As may be expected, the r_o values for Test A are closer to the potential flow result (analytical result) than Tests B and C.

The r_o is slightly over predicted in Cases 4 and 5 by three to six intake diameters, ($3d_o$ to $6d_o$) however, the nearness trend observed in r_o for the three tests is agreeable since approximately equal number of grids was used to discretize the domain. The slight differences in the analytical and numerical inviscid solutions may be attributed to the incapability of CFD to simulate a singularity point. Similar trend were observed for r_s (plotted on right vertical axis) as illustrated in Figure 4.9 and it is not discussed here to allow brevity. Thus, Test A will be considered for further analysis. On the whole, the agreement between the analytical result and inviscid data (Tests A, B and C) is reasonable given the discrepancies between the numerical model governing equations and the potential flow expressions.

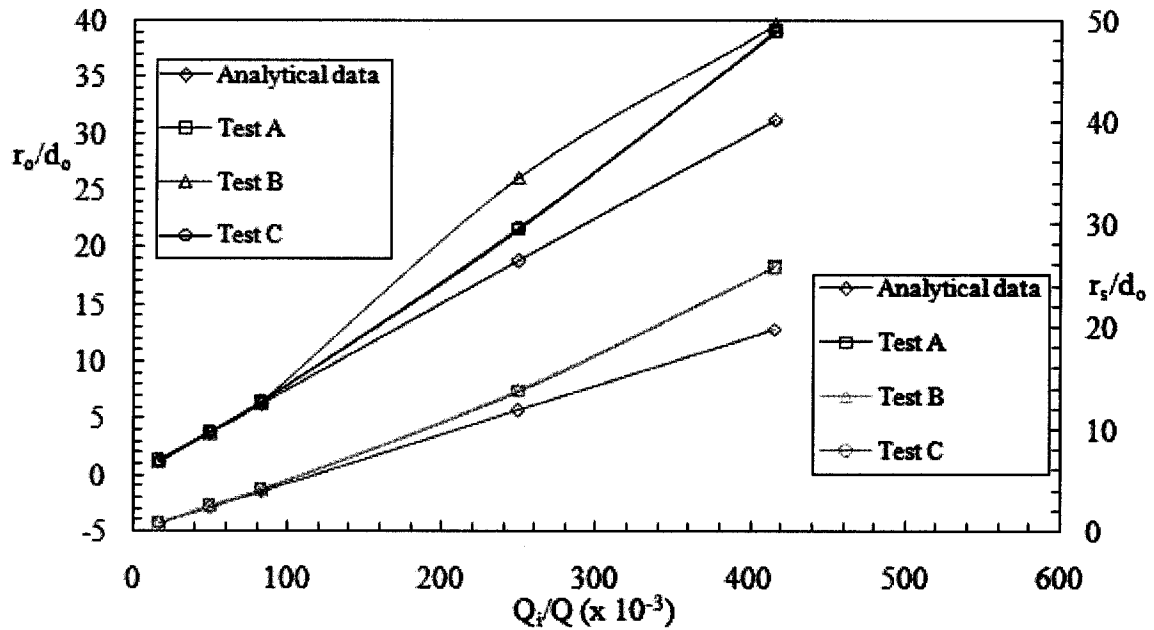


Figure 4.9: Analytical data comparison to numerical inviscid result for r_s and r_o

4.4.3 Flow field for laminar flow condition

A better prediction of the flow pattern into a hydraulic intake is had by investigating the problem while considering the effect of viscosity in the flow. In this

study, the laminar flow condition was employed to study the real nature of the flow under viscous conditions. Initially, the flow was modeled in its steady state (velocity at a given point in space does not vary with time) with relatively moderate solution convergence achieved at 5000 to 20000 iteration time steps for intake discharge Cases 1 to 4. After a prolonged wall-clock time, it was observed that the flow unsteadiness was established in Case 5 (highest discharge) which resulted in longer iteration steps without the convergence of the residual. Therefore, the model was further simulated as unsteady flow with a time step size of 0.001sec to further understand the flow features and to achieve convergence of the residual for cases with highest intake discharge, Cases 4 and 5. The solutions were found to converge within 20 to 300 time steps but the range of iteration accepted for actual result analysis was $4500 \leq \text{time steps} \leq 10000$. This range was considered necessary so as to ensure that other methods of judging convergence were achieved (see Appendix C) and to establish the influence of time steps. It was found that a time step size of 0.001sec is quite appropriate for the accuracy of this study. Figure 4.10 presents a comprehensive illustration of the flow patterns for the three tests. In this section, Cases 3, 4 and 5 (of all five cases) were selected to depict the flow patterns. Figure 4.10 (a-c) depicts the result of Case 3, Case 4 is contained in Figure 4.10 (d-f) and Case 5 is shown in Figure 4.10 (g-i) for the three tests respectively.

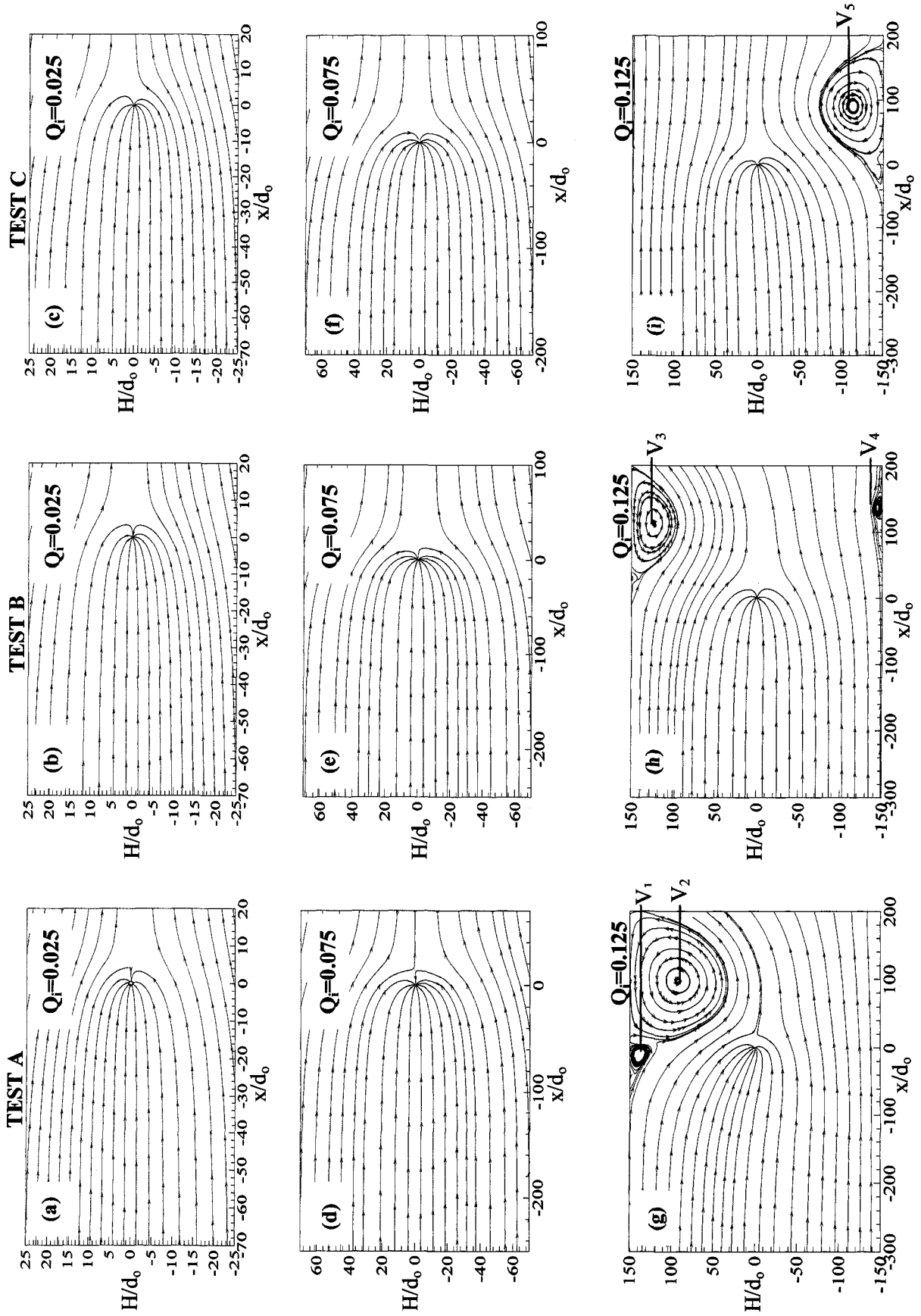


Figure 4.10: Flow patterns of laminar flow for Case 3 ($Q_i = 0.025$), Case 4 ($Q_i = 0.075$) and Case 5 ($Q_i = 0.125$)

The numerical estimation of the entrainment envelope for laminar flow is approximately similar to the inviscid solution presented in Section 4.2.2.3. It can be observed in Figure 4.10 (a-c) that the flow is divided into two regions, the flow that enters the intake pipe and the flow that escape the entrainment by flowing downstream of the intake. Specifically, Figure 4.10a reveals that passing flow must be at a perpendicular distance of $H = 12.51d_o$ away from the intake mouth to avoid being entrained. The stagnation streamline that separates the flow clearly defined the entrainment envelope for each of the cases. However, cursory inspection of Test C in Figure 4.10c shows that the width of entrainment envelope obtained is higher than those of Tests A and B for the same discharge. The comparison of Figure 4.10 (a-i) substantiates earlier deduction that the potential for entrainment of water varies with the intake discharge. For example, Case 3 in Figure 4.10a has a lower envelope width than Case 5 in Figure 4.10g.

Further assessment of Figure 4.10 reveals the unsteadiness and the additional flow features present in the flow. The main flow features present are attributed to the highest intake withdrawal rate; Figure 4.10g to Figure 4.10i. Comparison of these figures with Figure 4.10 (a-f) shows that the flow is stable for intake withdrawal rate Cases 1-4. In contrast to this observation is the flow instability characterized by strong re-circulation zone in Case 5. By examining Test A (Figure 4.10g), a strong reverse flow was found at the upper side wall right above the intake center, V_1 . At a horizontal distance of 100 diameters from the intake centre, the intensity of the vortical feature was strengthened and resulted into a strong clockwise vortical structure, V_2 , with vertical distance of $110d_o$ which diffused into the flow. Similarly, this vortical feature was found present in Test B (Figure 4.10h) at approximately the same horizontal distance drifted towards the channel outlet. Comparison of the two features (V_2 and V_3) shows that V_3 has a reduced vortical

intensity. Opposite to structure V_3 is a reversed flow that developed into a clockwise vortical structure V_4 close to the lower side wall. The core of the strong re-circulation zone is shifted to the lower side wall in Test C, thereby changing the relative positions of the vortices for the three tests. In order to ensure that the occurrence of these vortices is a result of flow instability and not due to the unsteady flow condition imposed on the problem, some of the converged steady solutions of Cases 3, 4 and 5 were re-simulated as unsteady flow. It was found that the unsteady state solution for the three cases corresponds to the previous steady state solution with no vortices and no change in the value of entrainment envelope.

Presented in Figure 4.11 is the stagnation streamline for all the discharge cases. Figures 4.11a, b and c represent the entrainment envelope for Test A, Test B and Test C respectively. As expected from the observation of Figure 4.10, the entrainment envelope increases as the discharge increases. The entrainment envelopes for the first four intake discharges were fairly symmetrical with controllable loss of symmetry. The corresponding entrainment envelope width H for the lowest intake discharge (Case 1) is $2.504d_o$, $2.506d_o$ and $1.648d_o$ for Test A, B, and C. On the contrary, the instability effect generated in the channel for the highest intake discharge (Case 5) distorted the motion of flow into the hydraulic intake.

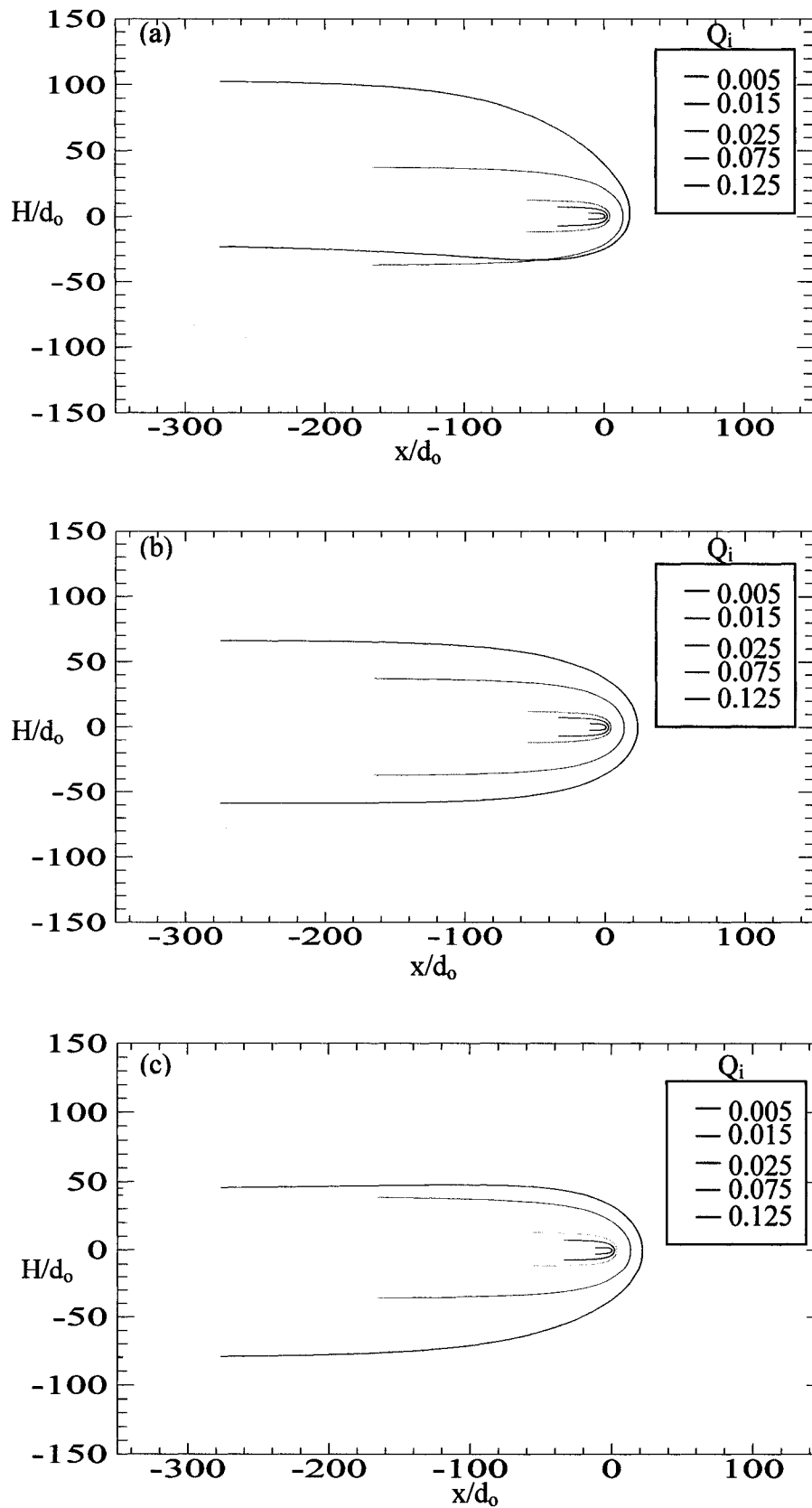


Figure 4.11: Stagnation streamline plots of laminar flow; (a) Test A (b) Test B and (c) Test C

The above figures clearly portray the extent of distortion of the entrainment envelope as a result of diffusion of vorticity into the flow from the upper wall for Tests A and B; and from the lower wall for Test C. Consequently, the entrainment envelope width for Test A and C is asymmetrical while that of Test B, although distorted, is comparatively symmetrical about the streamwise central horizontal line. Nevertheless, the figures conform to the trend of entrainment, that is, the highest intake discharge has the largest potential for entrainment and vice versa. For further reference, the largest $\pm H/d_o$ is considered for Case 5 only.

4.4.4 Comparison of vorticity contour to validate entrainment envelope distortion

The presence of vortical features in the channel flow authenticates the conclusion of many investigators (see Chapter 2) that the occurrence of vortices (either free surface or dye-core) is unpredictable and continues to be an issue at intakes. A closer look of Figure 4.10 (g-i) shows that the re-circulation region forms at the intake downstream because of convection and re-organization of strong vorticity induced by the flow at the entrance of the intake pipe. Hence, the vorticity magnitude around the intake region is examined for the highest intake discharge, Case 5. Figure 4.12a which represents the magnitude of vorticity over the intake pipe for Test A revealed that the vorticity created on the intake surface dispersed into the flow from the circumferential intake surface and convected downstream of the intake. The intensity was strong which resulted into a highly distorted entrainment envelope. A similar scenario exists for Test C but with less intensity. Figure 4.12b (zoomed view) on the other hand shows the magnitude of vorticity over the intake cylindrical surface for Test B, which can be concluded to evenly localized on the intake cylinder and confirms the entrainment envelope symmetrical shape.

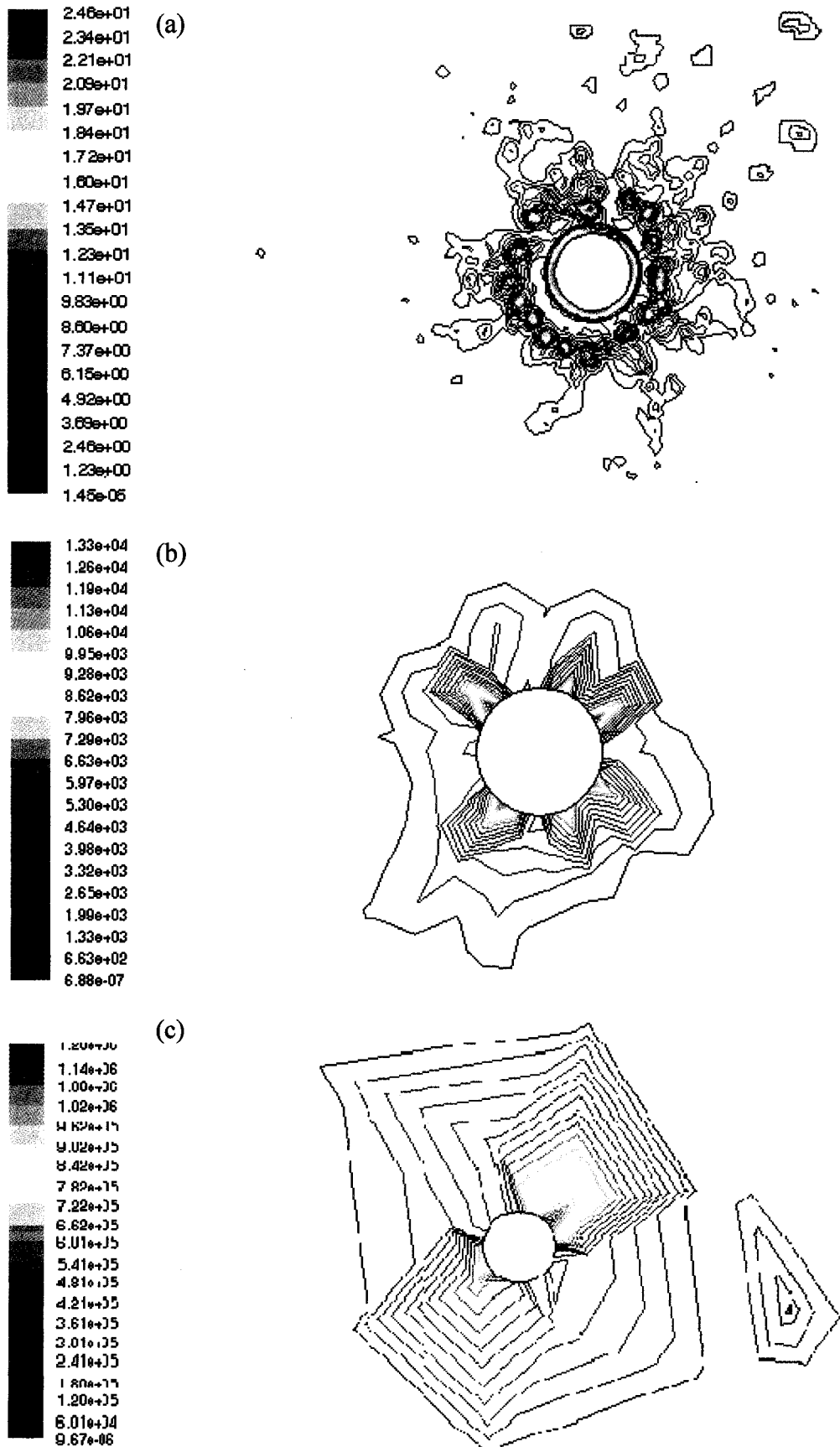


Figure 4.12: Contour plots of vorticity magnitude (1/s) for Case 5; (a) Test A, (b) Test B and (c) Test C

4.4.5 Comparison of numerical laminar data to potential flow theory

In reference to Figure 4.11, it can be ascertained that the entrainment envelope parameters for each test vary as the intake discharge increases. Figure 4.13 shows the change in the width H of the entrainment envelope. It is imperative to note that as the width of the entrainment envelope changes, the radial distance from the intake centre to the envelope r_s and the horizontal distance from intake centre to rear stagnation point r_o vary accordingly. The changes in r_o and r_s are provided in Figure 4.14.

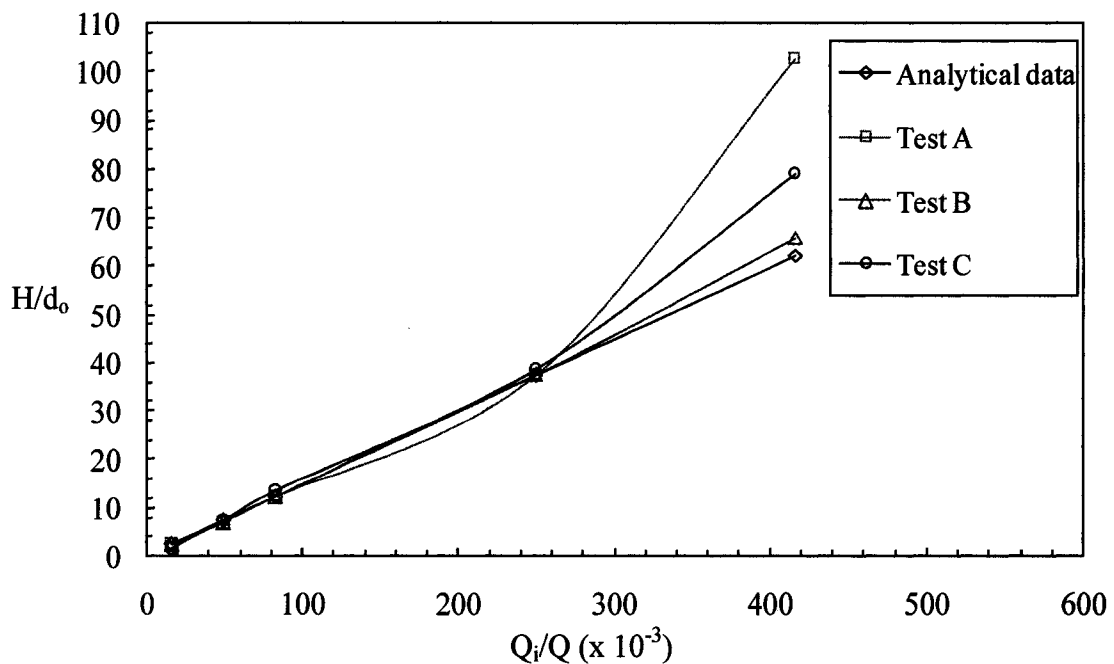


Figure 4.13: Analytical data comparison to numerical laminar solution for H

The plot in Figure 4.13 shows that the width of the entrainment envelope varies significantly for the three tests for Case 5; Test B shows good agreement to the analytical solution by an average percentage of 0.15%. Critical evaluation of the figure revealed that the three tests results are close to the analytical data for low intake discharges (Cases 1-3). The average percentage of change in width for Test C is 0.21%. Figure 4.14 also

agrees with this deduction. It detailed the changes in the parameter r_o and r_s of the entrainment envelope relative to the intake discharge. It confirms that Cases 4 and 5 results are over-predicted numerically and further shows that both Test B and Test C are in better agreement with analytical data than Test A. Under the ideal assumption of cylindrical flow symmetry about the intake's x -axis, the loss of symmetry plot in Figure 4.15 emphasized the symmetrical envelope for Test A except for Case 5 that was distorted. Overall assessment shows that Test A produced a symmetrical envelope for Cases 1-4 while Test B can be considered to yield symmetrical entrainment envelope for all the cases. It can be further deduced that potential flow analysis failed in predicting the entrainment envelope size at higher intake discharge (Case 5) for the three tests (see Figures 4.13 and 4.14). Comparison of these tests revealed that Test B clearly simulates the potential flow theory of singularity point.

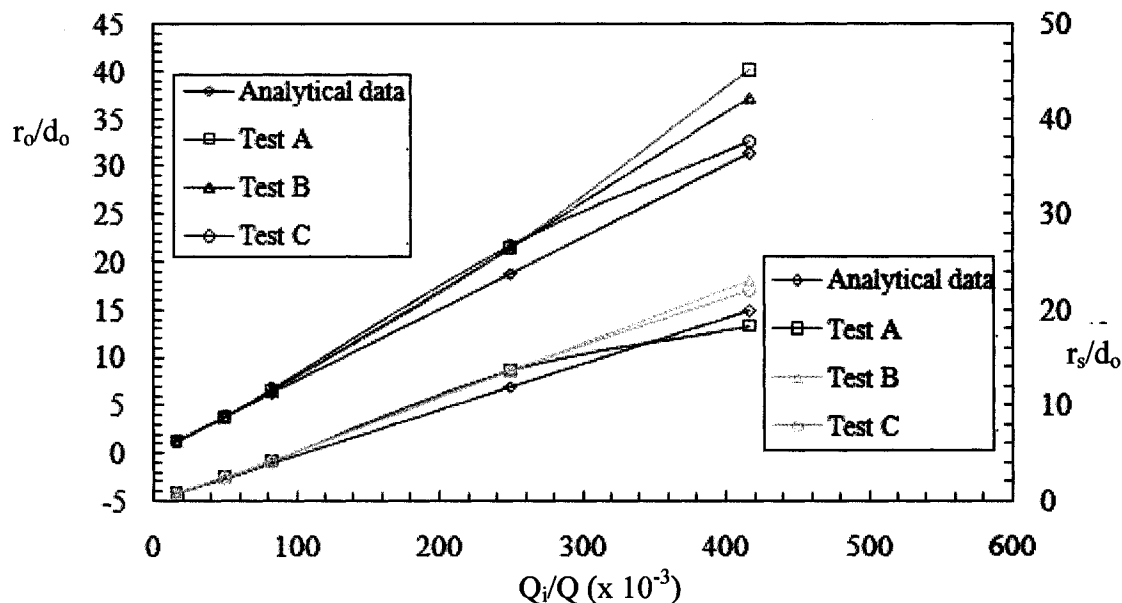


Figure 4.14: Analytical data comparison to numerical laminar solution for r_s and r_o .

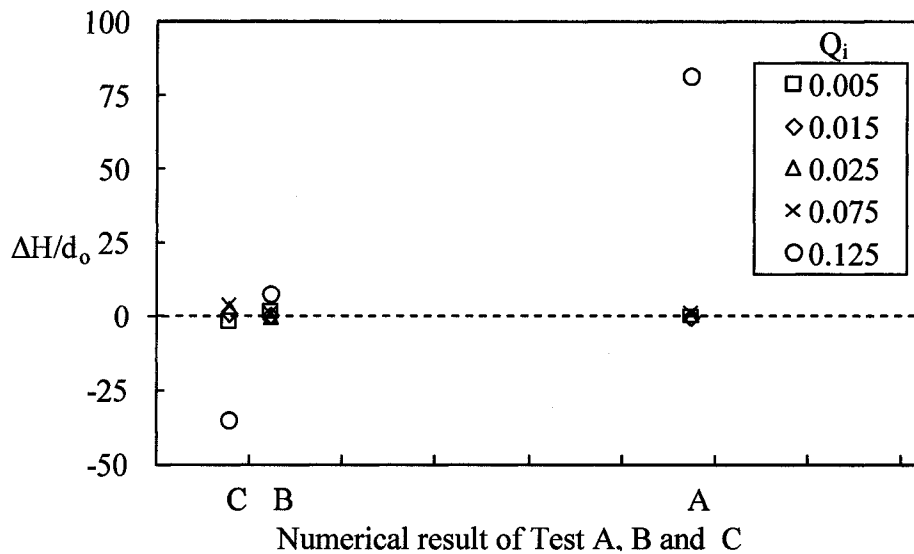


Figure 4.15: Influence of singularity on numerical laminar solution

4.5 Experimental Results

Velocity measurements were taken within the intake region of influence, described as 11 x 11 diameters around the intake centre in both streamwise and cross-wise directions. The velocity field was sampled using the sampling grid discussed in Chapter 3. Three intake discharges were investigated by measuring the mean velocities at the horizontal x - y plane positioned at $0.25d_o$ from the intake centreline. It is imperative to mention that the largest entrainment envelope for intakes can only be found at the intake entrance or outlet (discussed in the 3-D section), but this study was conducted at $0.25d_o$ due to restrictions imposed by the geometry of the transmitting optics, the positioning of the flume working section, the flume location and the intake pipe material. Figures 4.16-4.18 present the results from the velocity measurements scaled by the intake diameter d_o . Figure 4.16a depicts the streamwise vector plots for the lowest intake discharge (Case 1). The vector directions show that the flow into the intake is drawn from depth slightly above and below the intake rim. To clearly observe the radial extent of

flow into the intake as suggested by potential flow theory, a Kriging interpolation (provided in TecPlot360 software by Tecplot Inc.) method was used to interpolate spatially onto a circular 10 x 25 grid around the intake as presented in Figure 4.16b. This shows that flow into the intake comes from a fairly narrow band located about $1.2d_o$ above the intake centre ($r_o = 1.2d_o$) which is almost equal to $1.25d_o$ distance predicted by potential flow theory.

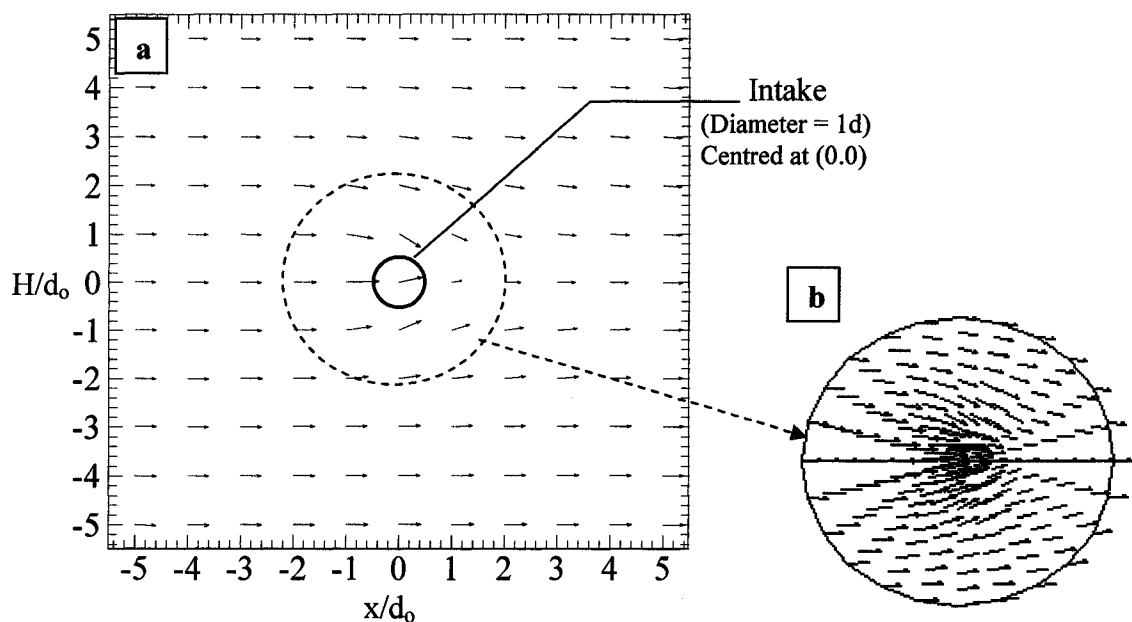


Figure 4.16: Velocity vector plots for Test A (a) full view (b) zoomed view of vectors at intake region of influence

The velocity vector plot for Case 2 and Case 3 are shown in Figures 4.17 and 4.18 respectively. It was not surprising that these figures are consistent with earlier results from potential flow theory and numerical study. The strongest velocities are observed at the intake entrance and converged into the intake pipe. The figures confirm the trend of entrainment such that Case 2 displays a lower potential for entrainment than Case 3. In

Figure 4.17, vectors located 3.5 diameters from the intake centreline are drawn into the intake while vectors beyond it flow downstream of the intake. This depth marks the radial distance above the intake region (r_o) that defines the entrainment envelope. Similar conclusion could be drawn from Figure 4.18 with vectors beyond 4.5 diameters converging into the intake.

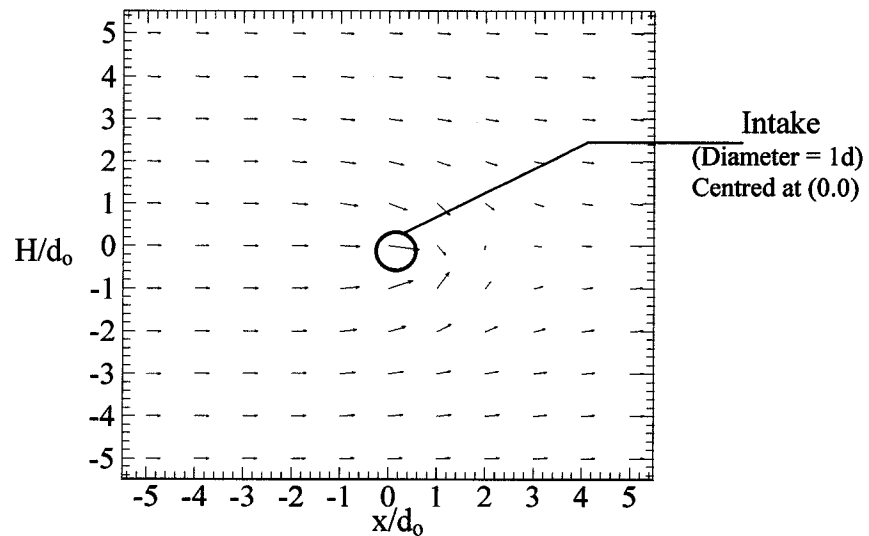


Figure 4.17: Velocity vector plots for Case 2

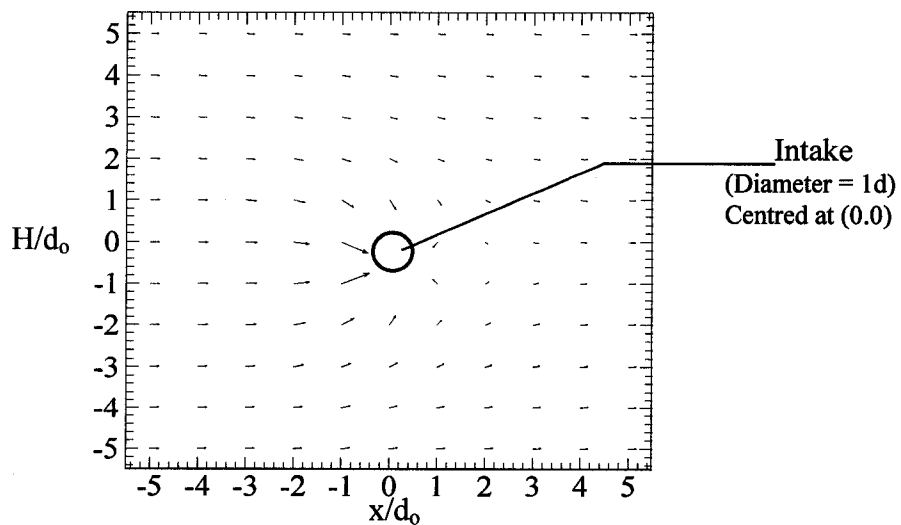


Figure 4.18: Velocity vector plots for Case 3

The experimental runs were repeated twice and similar velocity pattern were obtained for each case.

The following visual observations were made with the aid of dye injection so as to observe the potential for entrainment exhibited by the three intake discharges investigated (Cases 1-3). Based on detailed review of the video tapes and observations made during repeated experiments, the following figures were chosen to describe the entrainment envelope. Figures 4.19, 4.20 and 4.21 present Cases 1, 2 and 3 results in which the dye was steadily injected at approximate distances of $1.5d_o$, $3d_o$ and $4.5d_o$ from the intake mouth. Close observations of the figures show that Case 1 has the lowest potential for entrainment while Case 3 has the highest potential for entrainment. These observations confirmed the deduction made by velocity measurements, analytical and numerical methods. The extent of entrainment for each case was defined by a stagnation streamline.

4.6 Review of Two-Dimensional Flow Results

The investigational analysis of the 2-D flow patterns, streamlines, vorticity and vectors disclosed the flow behaviour into a hydraulic intake. It confirmed that the boundaries or region of withdrawal influence can be accurately predicted for a given flow condition. It clarifies the zone that is needed to be protected in order to guarantee the withdrawal of quality water from the river and to avoid intake ingestion of debris. It also gave an insight into the effect of vorticies on the entrainment envelope. Data comparison of these methods of approach is presented in Appendix F (Table F3) which shows good agreement in the three methods of approach. The three dimensional study of the entrainment envelope will give more insight into the width and depth of the region of withdrawal influence for an intake in a cross flow.

4.7 Three-Dimensional Flow Study

The three dimensional flow results were channel towards validating the behaviour of flow into a hydraulic intake predicted in 2-D and to clarify the flow features observed earlier in the study. All data were obtained at the asymptotic condition.

4.8 Potential Flow Solution of Three-Dimensional Flow

The delineation of intake withdrawal influence of a hydraulic intake in river using 3-D potential flow expressions (which reduced to a planar coordinate in Chapter 3) is similar to the 2-D techniques and procedures. Hence, the entrainment envelope results for each intake discharge/case will not be mentioned here to allow brevity but the superimposed stagnation streamlines presented in Figure 4.19 frame all the details. The figure affirms the trend of flow around a hydraulic intake in a channel by dividing the flow into two zones; the zone that is drawn into the intake which represents the depth (D) of the entrainment envelope (changed to depth D as a result of the 3-dimensionality of Rankine half-body) and zone that escapes the entrainment. Clearly illustrated in Figure 4.20 is the size of the entrainment envelope depth with respect to the increase in intake discharge. The figure confirms the linear relationship of these determinant factors such that increase in intake discharge amplifies the values of the entrainment envelope parameters. Case 5 with the highest intake discharge entrains water within the depth of $44.6d_o$ from the intake centre while Case 1 entrains water within $9.0d_o$ from the intake centre respectively. In other words, flow at $D \leq 44.6d_o$ will be drawn into the intake while flow within $D \geq 44.6d_o$ will escape the entrainment. Figure 4.19 is set as standard for judging the delineation of the entrainment envelope for 3-D numerical approach.

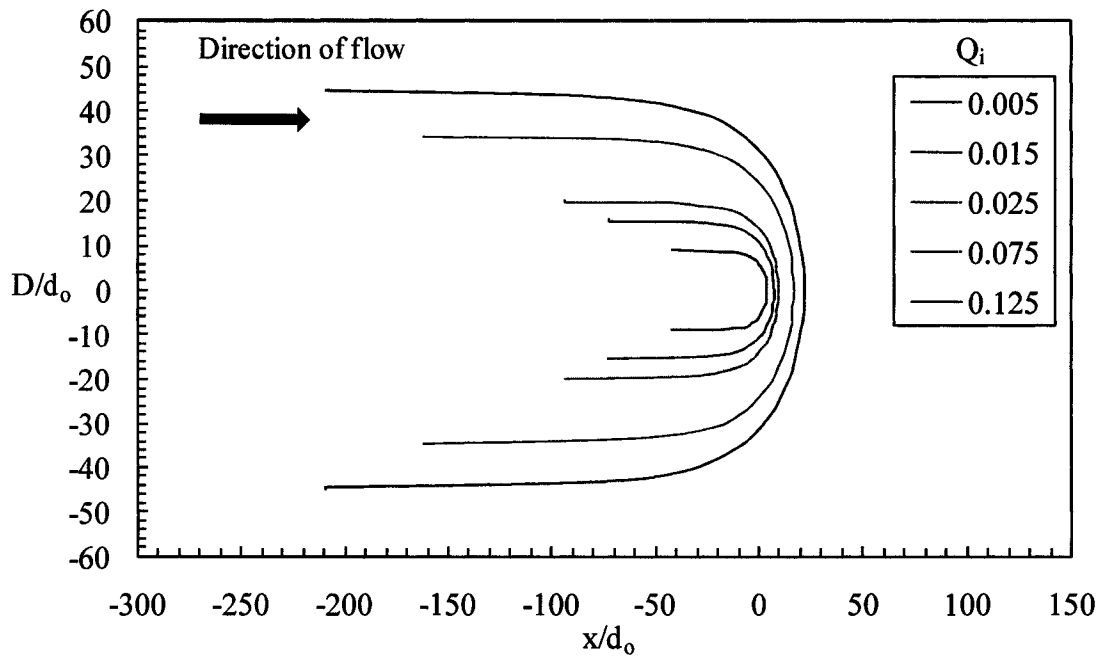


Figure 4.19: 3-D potential flow result for intake discharges - Cases 1-5.

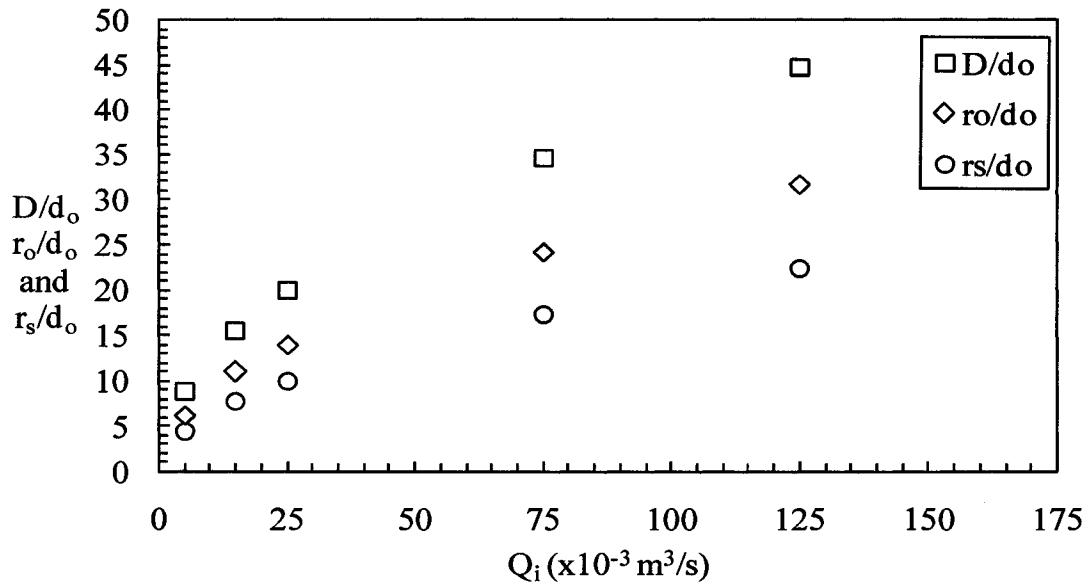


Figure 4.20: Relationship between intake discharge and entrainment envelope parameters

4.9 Numerical Solution of Three-Dimensional Flow

The three-dimensional data was visualized by taken two-dimensional sections or planar cuts through the data. These horizontal ($x-z$) and vertical ($x-y$) planes were then selected for comparison purposes. The horizontal plane gives the maximum width of flow measured from intake entrance and vertical plane provides the maximum depth of the flow drawn into the intake. From brief study, it was observed that the planar section right at the entrance and centre of the intake pipe contribute the maximum width and depth of the entrainment envelope. Thus, all subsequent data reported in this section were taken from these planes.

4.9.1 Flow field for 3-D inviscid flow condition

Figure 4.21 presents the flow pattern in a vertical plane situated at the intake mouth ($z = 25d_o$) for Tests A, B and C. Case 1 of each test is presented here to establish comparison. Preliminary inspection of the flow patterns reveal the portion of flow that goes into the intake. Figure 4.21a shows that flow at perpendicular distance of $9d_o$ is drawn into the intake while Figures 4.21b and 4.21c revealed a depth of 9.55 and 9.20 diameters for Tests B and C respectively. These differences in values confirmed earlier deduction (from 2-D) of singularity effect. Also, Figure 4.22 depicts the flow patterns in a horizontal plane positioned at the intake centre line ($y = 0$) for Case 1. For Test A (Figure 4.22a), the flow passing the intake at a perpendicular distance of $9d_o$ or greater will not enter the intake. Figures 4.22b and 4.22c reflect a perpendicular distance of $9.80d_o$ and $9.50d_o$ for Tests B and C respectively. A close observation of Figures 4.21 and 4.22 clearly show the difference in the extent of the entrainment envelope which can be attributed to the increase in intake discharge as concluded in 2-D flow study.

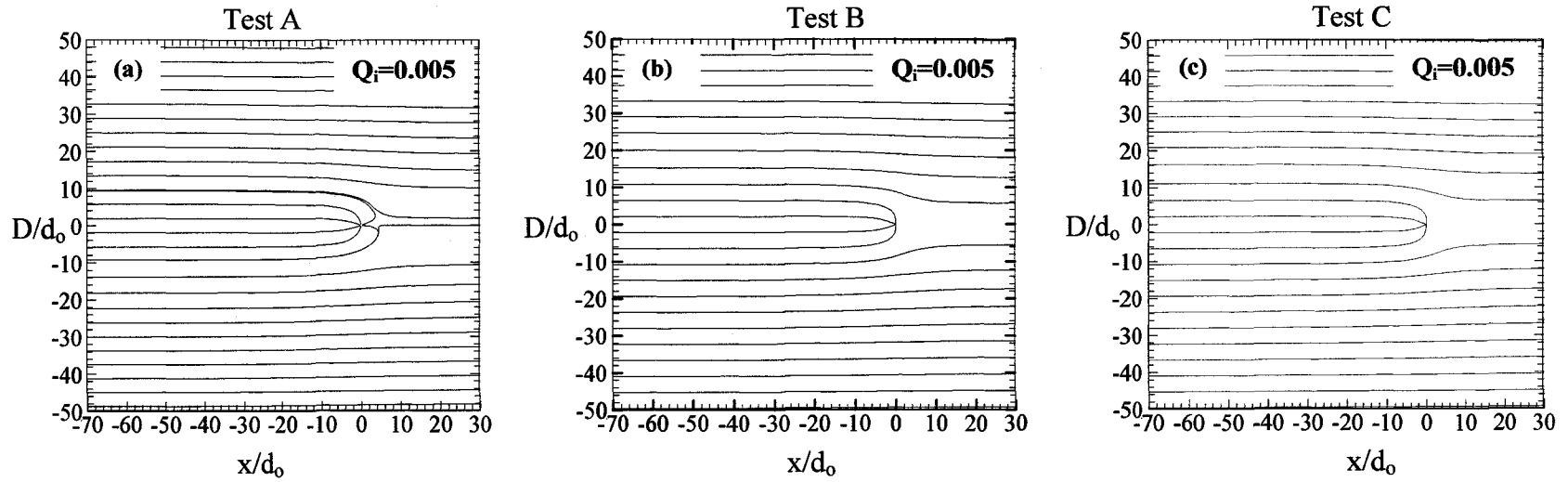


Figure 4.21: Flow patterns of inviscid flow for Case 1 ($Q_i = 0.005$) at a vertical plane $z = 25d_0$

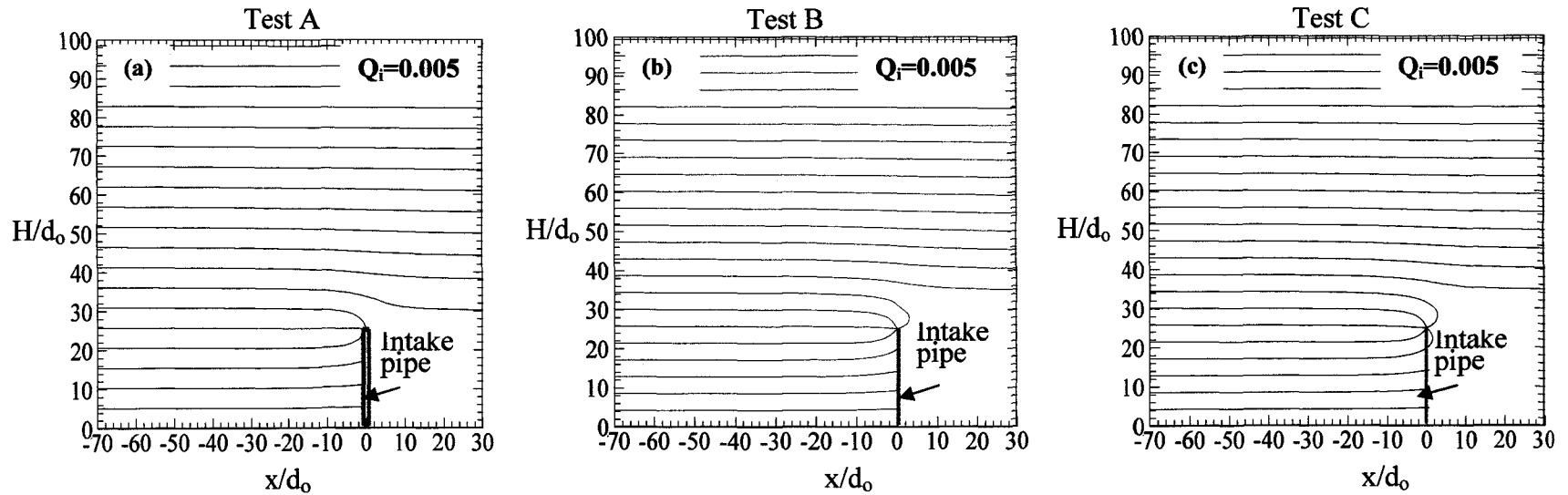
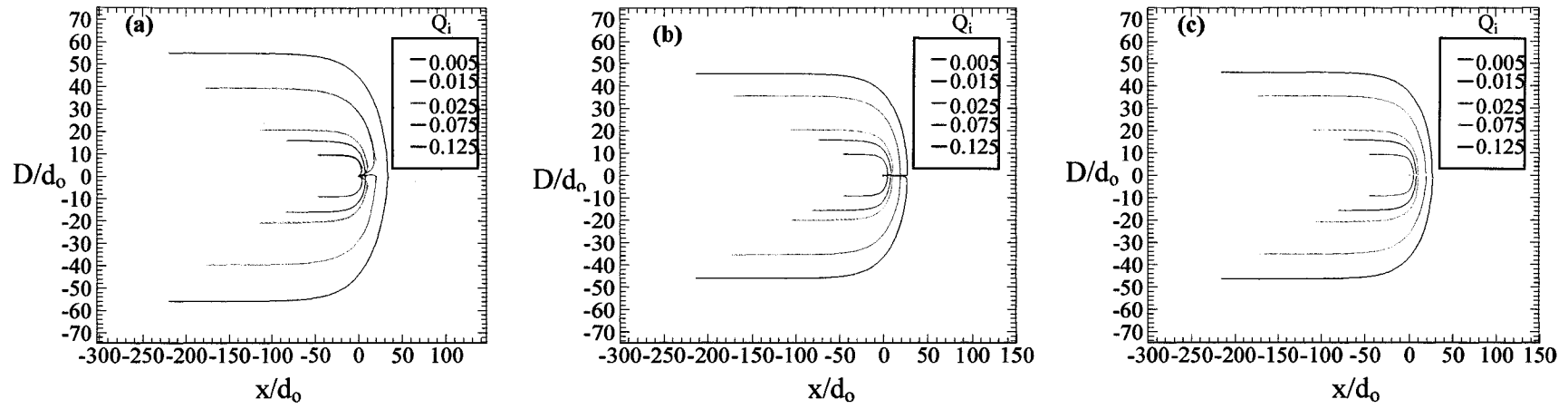


Figure 4.22: Flow patterns of inviscid flow for Case 1 ($Q_i = 0.005$) at a horizontal plane $y = 0$



69

Figure 4.23: Stagnation streamline plots of inviscid flow at vertical plane $z = 25d_0$; (a) Test A (b) Test B and (c) Test C

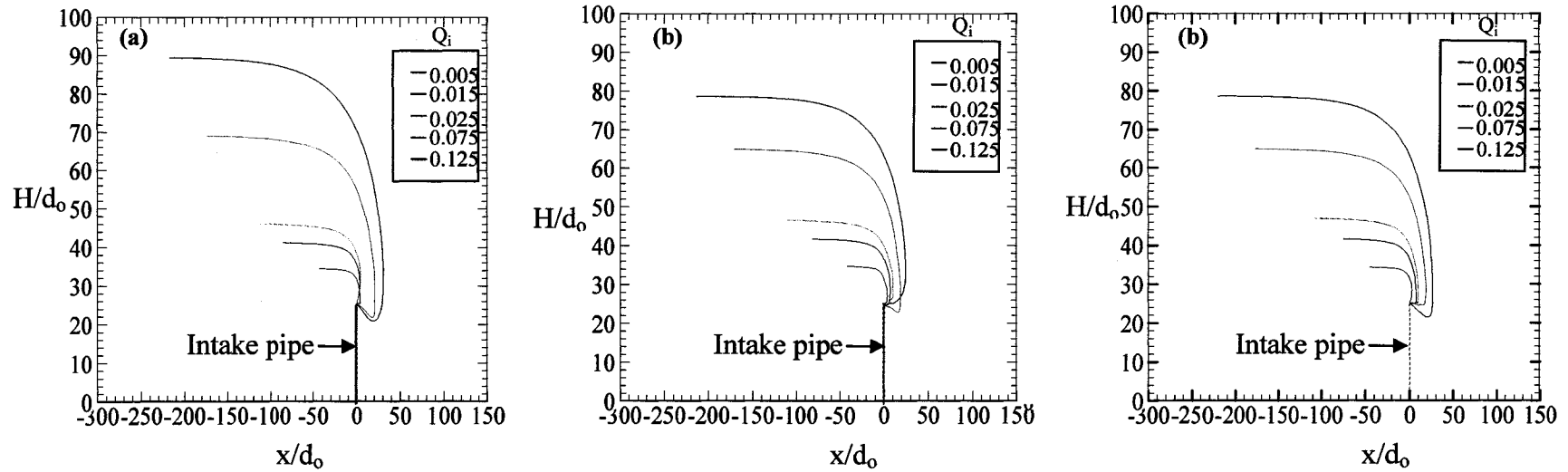


Figure 4.24: Stagnation streamline plots of inviscid flow at horizontal plane $y = 0$; (a) Test A (b) Test B and (c) Test C

Similar flow patterns were obtained for Cases 2-5 (not shown) with increasing envelope size. Figures 4.23 and 4.24 illustrate the stagnated streamlines that delineate the depth and width of the entrainment envelope for the three tests.

4.9.2 3-D numerical inviscid and analytical data comparison

The difference in the two flow conditions, inviscid and laminar flow is presented in Figure 4.25. As concluded in the 2-D study that an increase in intake flow proportion Q_i increases the entrainment envelope parameters (i.e. entrainment envelope width H , horizontal and radial distances from the intake centre to the entrainment envelope r_s and r_o), the comparison focus only on the width (H - located at left vertical axis) and depth of the entrainment envelope (D - located at right vertical axis) for the three tests studied (reader should take note of change in scale in the two vertical axes). It can be observed from the figure that Test B and Test C best model the potential flow solution with average percentages of 1.1% and 1.25% respectively. It also revealed that Tests B and C are symmetrical about the intake axis. In contrast, Test A result varies significantly from the potential flow solution with an average percentage of 9.41%. The result of Test A when compared with Tests B and C shows that it over-predicted the entrainment envelope parameters for Cases 4 and 5. Loss of symmetry is found in Test A (not shown) in comparison with potential flow solution as a result of revolution of the envelope about its axis. This confirms the importance of singularity effect in the delineation of entrainment envelope by 3-D potential flow approach. On the other hand, Figure 4.25 reveals the incapability of potential flow solution to predict the depth of the envelope at higher intake discharge (Cases 4 and 5) for the three tests.

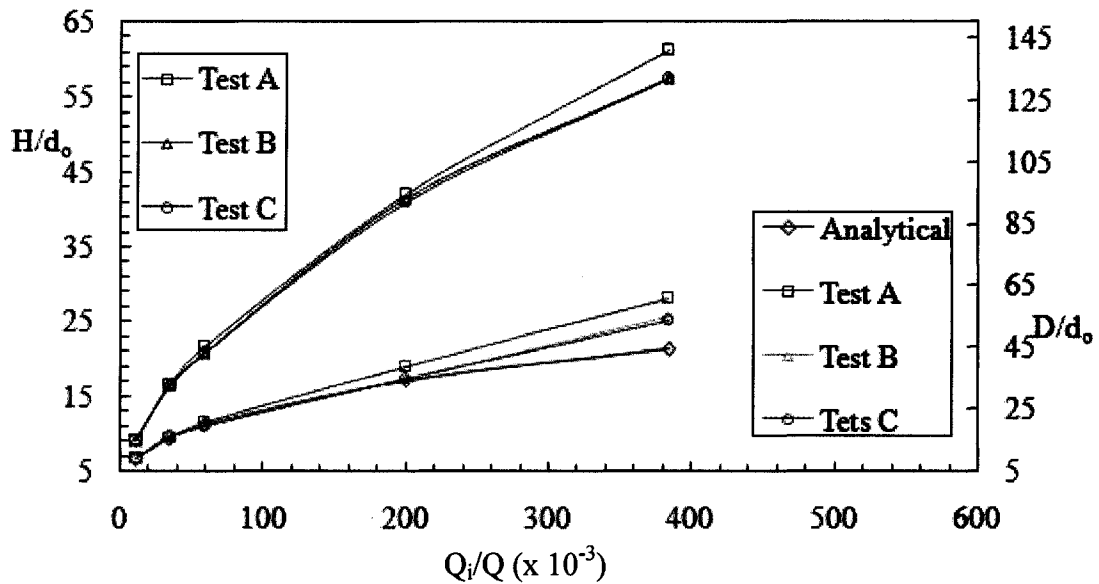


Figure 4.25: Comparison of 3-D potential flow and numerical inviscid solutions

4.9.3 Flow field for 3-D laminar flow condition

Figure 4.26 portrays the depth of the entrainment envelope on a vertical plane located at the intake mouth for Cases 3, 4 and 5. Similar to 2-D study, both steady and unsteady flow conditions were considered and the solutions were found to be similar for the three tests. In Figure 4.26 (a, b and c), the depth of flow entrained into the intake was measured as $20.8d_o$ for Test A, $20.0d_o$ and $19.6d_o$ for Test B and Test C respectively. Close observation of Case 4 shows the gradual distortion of the envelope by the vortices as observed in the 2-D laminar flow study. The presence of vortices at the intake mouth was fully established in Case 5, which caused an increase in the depth of the envelope to $61.0d_o$ for Test A (with larger vorticity magnitude) and $54.1d_o$ for Tests B and C as compared to analytical envelope width of $45d_o$. Additional observation of fully developed clockwise vortices (V_1 and V_2) was found in Case 5.

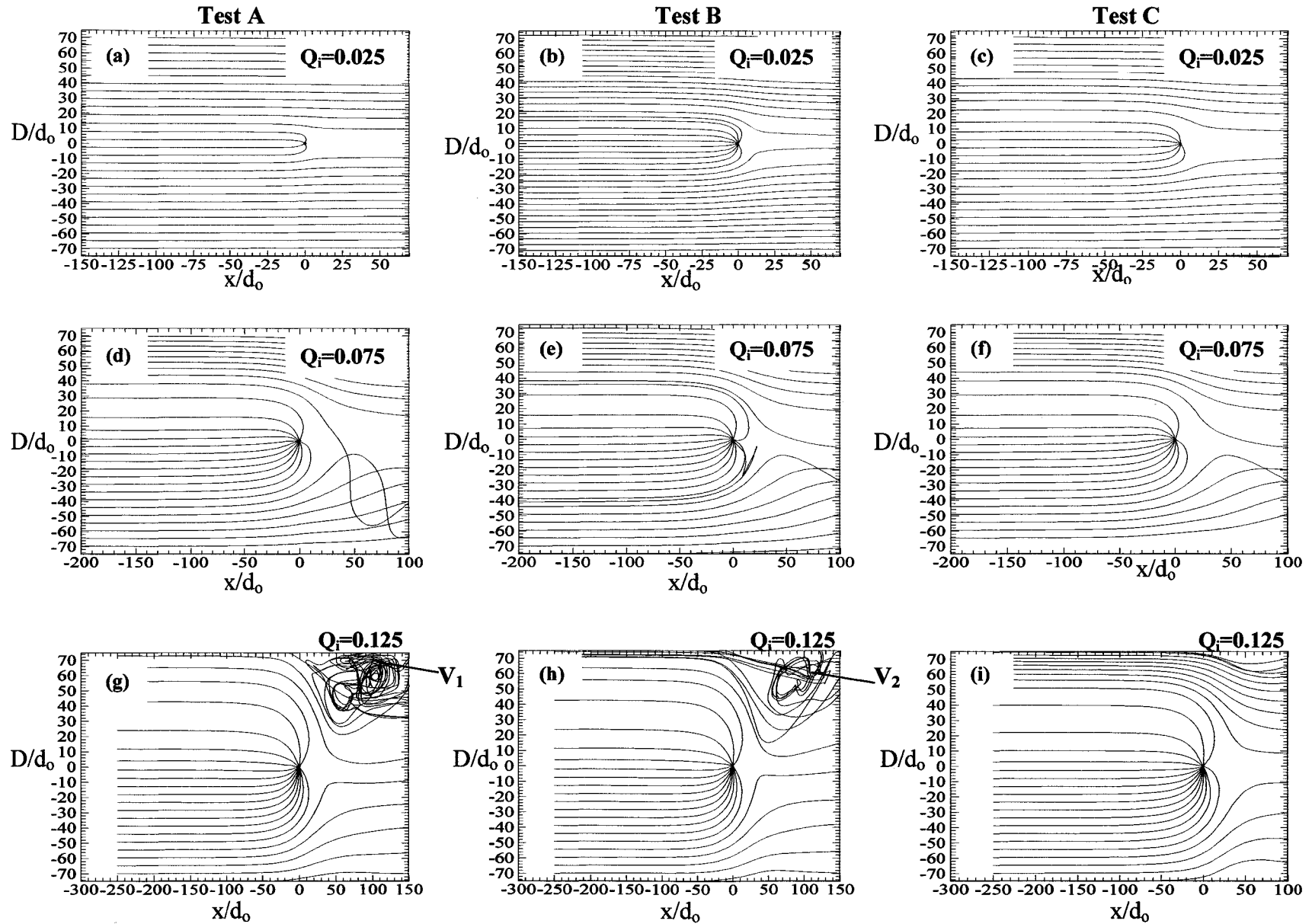


Figure 4.26: Flow patterns of laminar flow for Case 3 ($Q_i = 0.025$), Case 4 ($Q_i = 0.075$) and Case 5 ($Q_i = 0.125$) at a vertical plane $z = 25d_0$

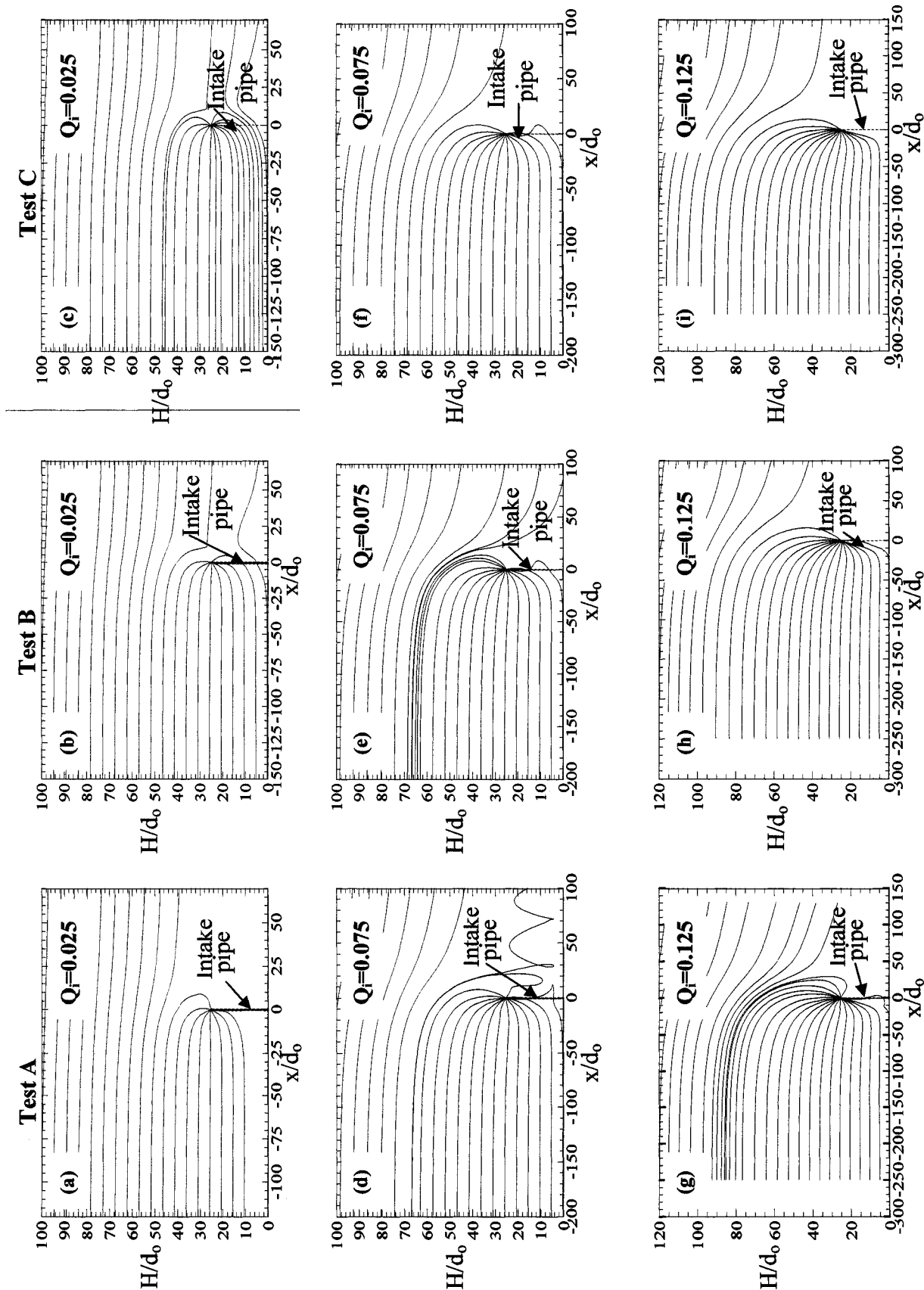


Figure 4.27: Flow patterns of laminar flow for Case 3 ($Q_i = 0.025$), Case 4 ($Q_i = 0.075$) and Case 5 ($Q_i = 0.125$) at a horizontal plane $y = 0$

Figure 4.27 confirms these flow features and revealed the differences in the width of the entrainment envelope. For Case 5, the width was measured as $61.25d_o$ for Test A and reduced to $57.50d_o$ for Tests B and C. The significant differences in the entrainment envelope of each case were detailed in Figures 4.28 and 4.29 for Tests A and B (Test C was not repeated since Tests B and C results are similar). These figures depict that the entrainment potential is greater in Case 5 than subsequent cases and result into increase in the depth and width of the envelope with corresponding increase in intake discharge. Further assessment of Figures 4.28 and 4.29 revealed the asymmetrical shape of the entrainment envelope of Tests A and B for Case 5 when compared to 3-D potential flow solution. This may be attributed to full establishment of vortices effect at higher intake discharge. It also shows the distorted stagnation streamline of Case 4 by vortices, prior its diffusion into the flow.

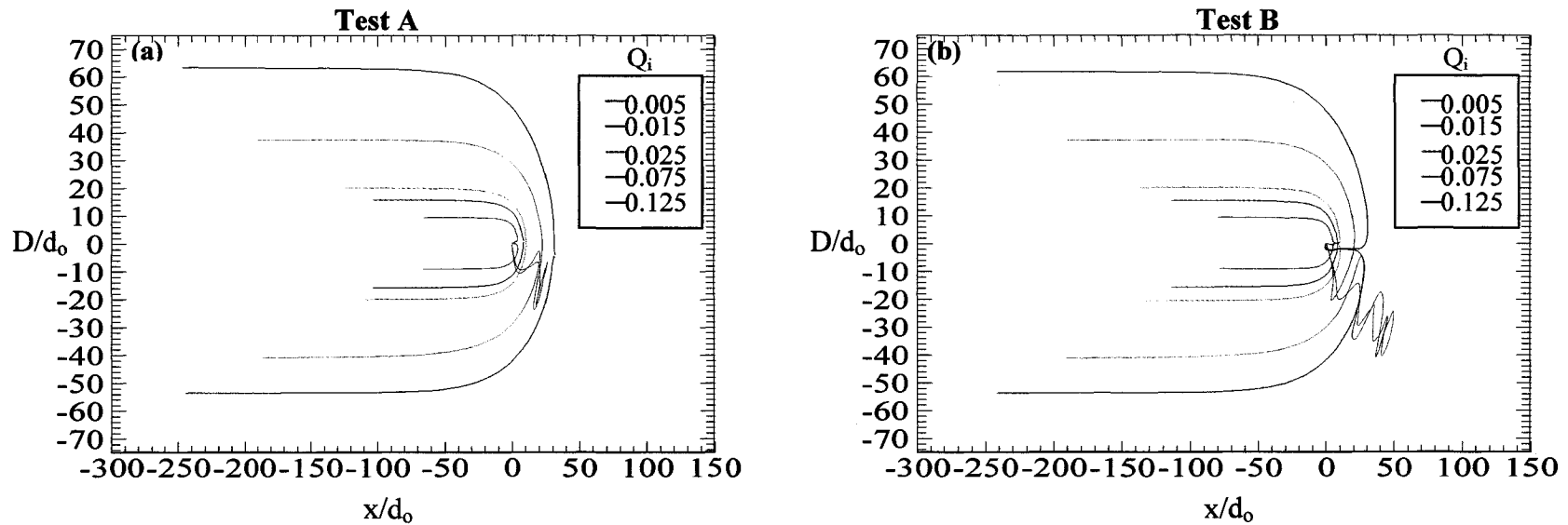


Figure 4.28: Stagnation streamline plots of laminar flow at vertical plane $z = 25d_0$; (a) Test A and (b) Test B

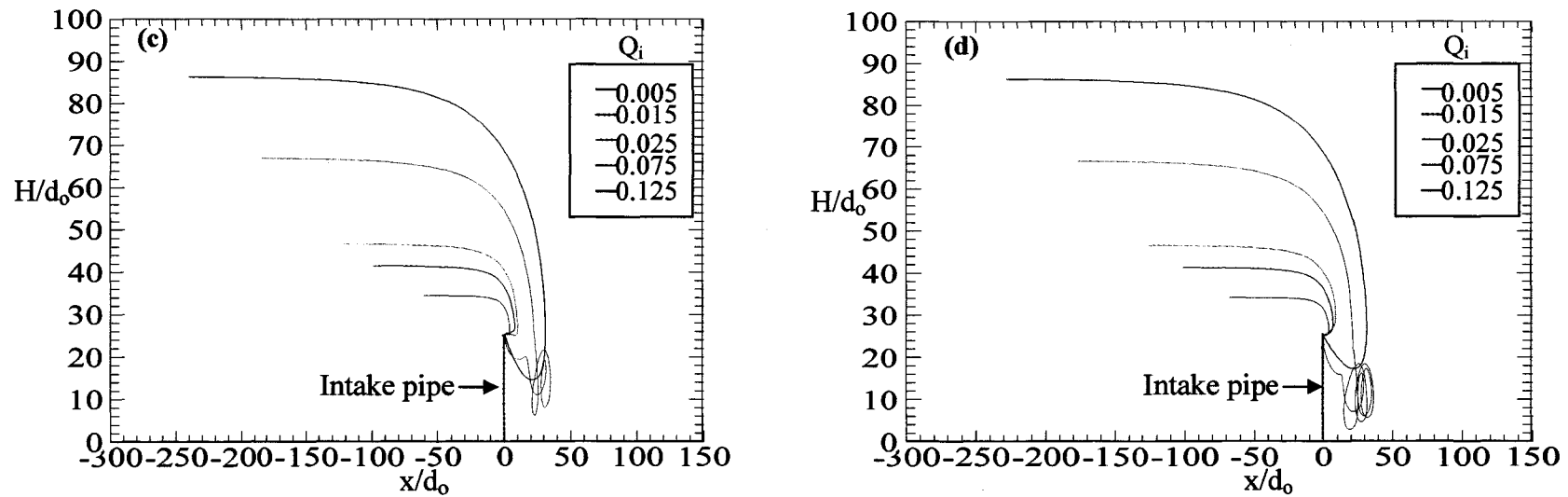


Figure 4.29: Stagnation streamline plots of laminar flow at horizontal plane $y = 0$; (a) Test A and (b) Test B

4.9.4 Numerical laminar and analytical data comparison

The width (H) and depth (D) of the entrainment envelope were further analyzed in Figure 4.30. It shows that Test B and Test C best simulate the potential flow solution with an overall average of 1.31% and 1.35%. On the other hand, Test A exhibited a linear relationship with analytical data, Test B and Test C for Cases 1, 2 and 3 and overestimated the envelope in Cases 4, 5. The loss of linearity for Test A may be as a result of extensive vorticity diffusion into the flow and the size of the intake diameter ($1d_o$). Similar to the deduction made from inviscid flow analysis, Figure 4.33 reveals that the potential flow result failed in predicting the entrainment envelope at higher intake discharge (especially Case 5) for the three tests. The assessment of envelope parameters (r_o and r_s) were similar, hence they were not repeated in this section. The details of data compared are provided in Appendix F (Table F4).

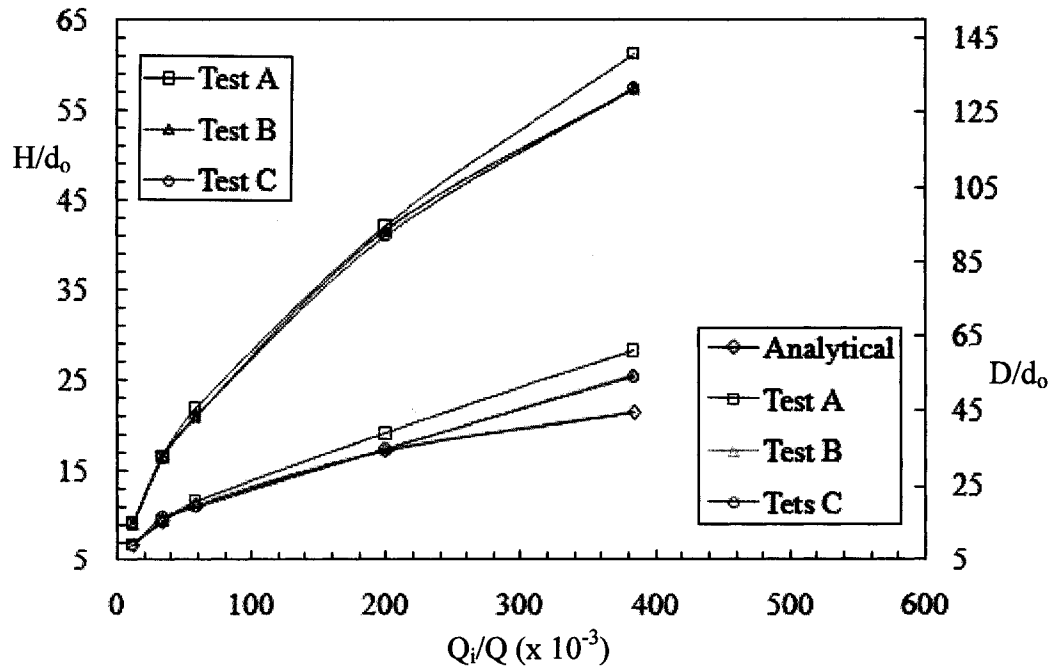


Figure 4.30: Numerical laminar flow data compared to potential flow solution

4.10 Review of Three-Dimensional Flow Results

The three dimensional study of the flow into an intake indeed gave more insight into the formation of the entrainment envelope by defining both the width and depth of flow that enter the intake. The potential flow theory predicts the depth of entrainment envelope for lower to moderate intake discharges (Cases 1-3) which was further confirmed by the inviscid and laminar flow results of the numerical analyses. However, as the intake discharge increases, the capability of the potential flow theory to accurately predict the entrainment envelope reduced. The effect of vortices in the region around the intake was revealed in the laminar flow analysis which confirms earlier deduction in the 2-D study. The data compared in this section is detailed in Appendix F which shows good agreement in the delineation methods with Test B being the best replica of the potential flow solution for the two flow conditions. Overall, this investigation has presented figures that illustrate the extensive region of the intake entrainment envelope. The minor differences in the methods of approach (for both 2-D and 3-D) may be due to the following:

- (1) The potential flow theory considers flow to be inviscid (frictionless) with negligible surface tension and circulation in the approaching uniform canal flow while in real fluid flow, viscosity, surface tension and circulation effects exist.
- (2) The equations for potential flow theory is based on singularity point (perfect point sink or negligible intake diameter) while the numerical and experimental methods consider the size of the intake diameter.
- (3) As a result of limited experiments conducted, the effect of side-wall boundary layer effect (which usually causes the streamlines close to the outer boundary of

the intake pipe to be non-radial) on the entrainment envelope was not investigated.

- (4) Although, the uncertainty analyses reveal the accuracy of the study, measurement errors may still account for this disparity.

4.11 Physical Significance of Study to IPZ Delineation

This study was targeted to complement the work of watershed community representatives and organizations that focused on delineating the Intake Protection Zones based on the “Surface Water Guidance Modules’ set up by the Ministry of Environment Canada. To reiterate, the IPZ is the designated area/zones around the intakes that is to be protected from immediate contaminants of concern that might potentially impact the quality of water drawn into the intake. The physical model used for this study is the City of Windsor Intake located in the Detroit River (See Figure 4.31). The Detroit River is one of the Great Lakes connecting channels, hence, the modules in defining the IPZ for Great Lakes connecting channels intakes apply here. According to the guidance module, two zones are required to be potentially delineated; Zone 1 (GC IPZ-1) which is referred to as the most vulnerable zone and Zone 2 (GC IPZ-2) defined as zones outside the first zone that can impact the intake. This research work is limited to the area around the intake crib/mouth (GC IPZ-1) which is considered as the most vulnerable as a result of its close proximity to the intake.

The MOE guideline for establishing GC IPZ-1 is to first set a minimum upstream distance which include a semi-circle shape with a 1km radius (location of intake is the centre of circle) as shown in Figure 3.2a. The shape of the GC IPZ-1 can be further modified based on the flow dynamics (geophysical properties) around the water intake as

shown in Figure 3.2b. For both set and refined GC-IPZ-1 shape, a minimum downstream distance of 100m from the intake should be established to compensate for possible localized back drift influences of wind and/or channel operations for hydroelectric or navigation purposes. This defined shape marks the zone that will be critically protected from every contaminant polluting our drinking water. The 1km starting fixed radius established by MOE was obtained based on the following considerations:

- (a) The minimum time of travel distance upstream of an intake.
- (b) Assessment of the temporal and spatial mixing patterns of incoming flows around the intake.
- (c) The minimum response time for the water treatment plant operator to respond to adverse conditions or an emergency spill, set at a minimum two hour contaminant travel time to the intake.

The second step in delineating the IPZ is to refine the set out (minimum) zone by considering the unique features of the intake, its location and physical features, the surrounding environment, and other area of influence around the intake across a range of hydrodynamic conditions.

This being said, presented in Figure 4.33 is the set-out GC IPZ-1 and the developed entrainment envelope for the prototype withdrawal rate (City of Windsor Intake) using the Froude scaling technique presented in Appendix A. This figure was developed using the Google Earth software manufactured by Earth-360.org in order to accurately estimate the GC IPZ-1 distance, City of Windsor intake location and the entrainment envelope. The figure illustrates that the immediate zone from which the hydraulic intake (entrainment envelope) draws its water is 23m radius for the physical

model intake discharge. By adding a factor of safety of 100%, the total distance is equivalent to 46m, which means that out of the 1000m designated protected zone, the City of Windsor withdraw water from is immediate surrounding region marked by 46m radius distance. The relevance of this is that this value can be considered along with other factors in refining the Intake Protection Zone as outlined in the guidance module. The awareness of the immediate region from which the intake draws its water might allow flexibility in refining the Intake Protection Zone.



Figure 4.31: Physical model location in Great Lakes connecting channel

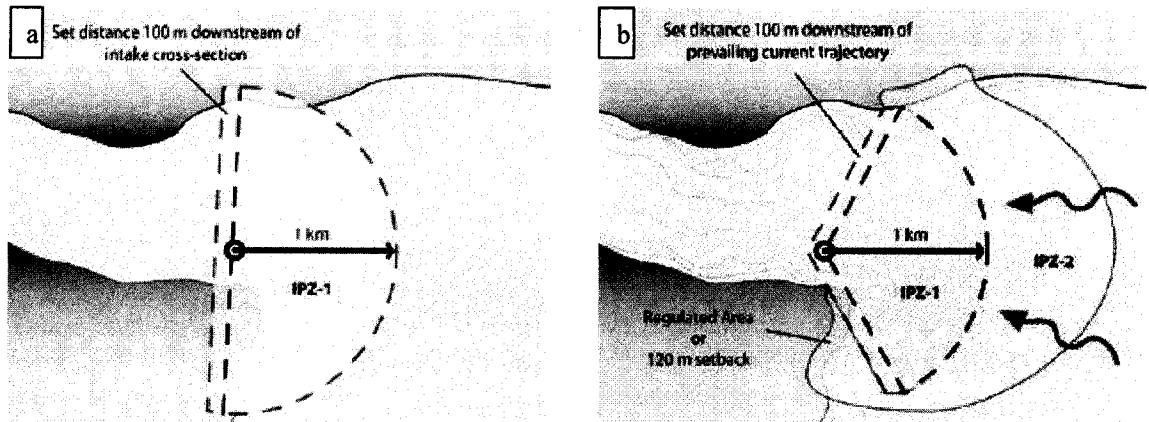


Figure 4.32: Zone delineation techniques by MOE guidance module (2006): (a) preliminary intake zone; (b) revised zone based on geophysical properties

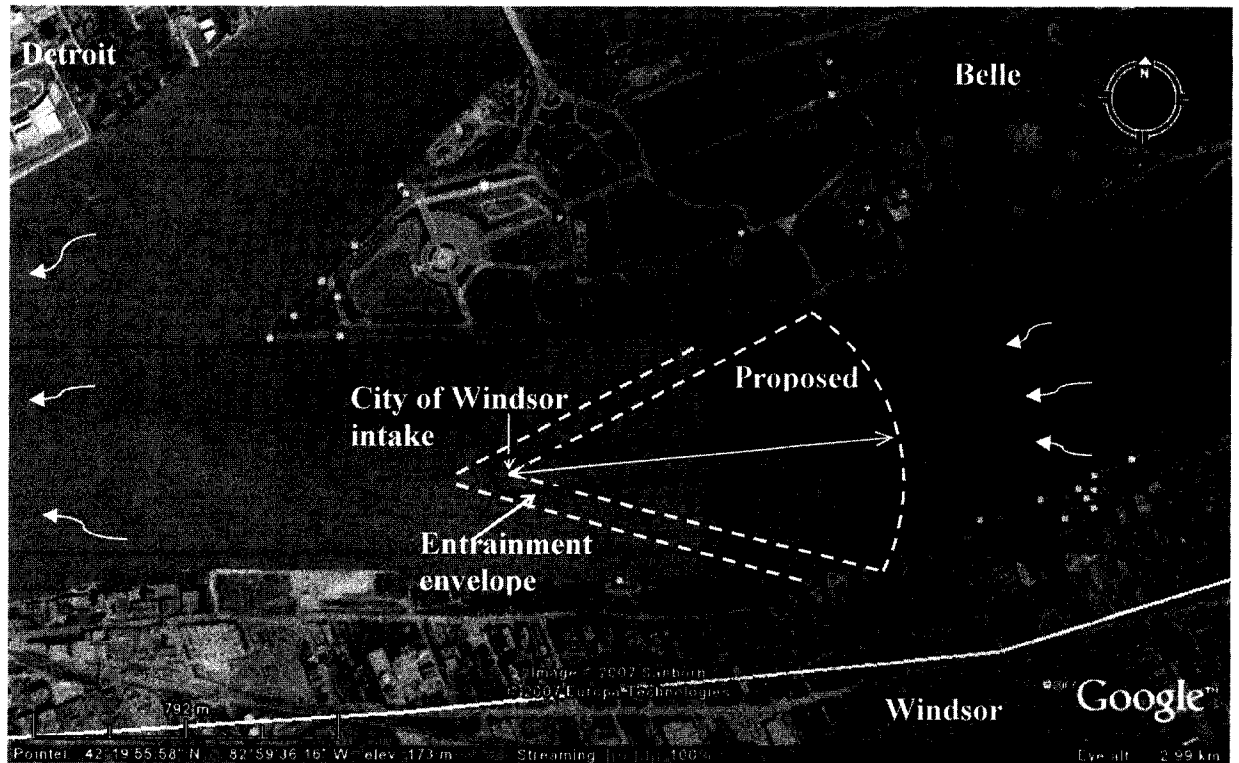


Figure 4.33: Illustration of GC 1PZ1 and entrainment envelope

CHAPTER 5

CONCLUSIONS AND RECOMMENDATIONS

5.1 Conclusions

This research was carried out to investigate the delineation of the water intake entrainment envelope for two hydraulic flow conditions using three methods. The potential flow theory was applied by combining the point sink having the same discharge and centre as the intake and the uniform flow. Two dimensional flow pattern established contrast in the numerical inviscid and laminar radial flow into the intake. The three dimensional investigation of the radial flow, experimental velocity measurements and visual observation aided in deciphering the entrainment envelope and other important flow features that consequentially impact the performance of water intakes. This study bears some significance since majority of the literature reviewed have focused on measurement and mitigating vortices at hydraulic intakes. Results from this investigation may be applied to further understand the connection between the intake entrainment envelope and the presence of vortices. More importantly, this work furnishes a starting point in delineating the protection zone (IPZ) for our public water intakes situated in river in an effort to find appropriate solution to our environmental concerns. The main conclusion drawn from these methods of approaches are detailed as follows:

- (1) Previous studies have recognised that the potential flow solution is useful in providing solution to simple hydraulic problems. The present study quantitatively validates the role of this theory by delineating the hydraulic intake entrainment envelope at asymptotic state. It defined the entrainment envelope as the region of withdrawal influence or area providing water to the hydraulic intake which is

described as the Rankine half-body. The numerical and experimental analyses of the exact model qualitatively validated this theory and confirm the delineation of the intake entrainment envelope. The entrainment envelope developed for the inviscid radial flow by these methods is extended to 2.5 diameters from the intake line of symmetry at an asymptotic state for the lowest intake discharge.

- (2) The comparison of the methods of approaches for both 2-D and 3-D inviscid and laminar radial flow conditions confirmed the symmetrical shape of the intake entrainment envelope and accurately predicted the width of the entrainment envelope. An approximate equal dimension of intake entrainment envelope was obtained for each intake discharge with different methods. Similar linear trend was observed in the potential for entrainment as the intake discharge increases. Ultimately, the withdrawal for the highest intake discharge substantially increased the dimensions of the intake entrainment envelope to 62.5 diameters above the intake centreline; exhibiting a higher potential while the entrainment envelope developed by the lowest intake discharge was 2.5 diameters. These similarities and uniformity in the entrainment envelope dimensions confirmed the accurate delineation of entrainment envelope by the three delineation methods.
- (3) The numerical simulation of three tests condition with varying intake pipe diameters clarify the importance of singularity point in potential flow theory and the deviation of this theory from reality as the diameter of the intake increases. The comparison of the three tests entrainment envelope revealed loss of symmetry in the test condition with highest intake pipe diameter ($1d_o$) while test condition with reduced diameter ($0.1d_o$) accurately modeled the potential flow theory with

symmetrical entrainment envelope about its central intake axis. That is, potential flow assumption (with a singular point sink) fails at $d_i > 0.1d_o$.

- (4) The 3-D study of the entrainment envelope provides more physical relevance of the study by delineating the width of water drawn into the intake (entrainment envelope width) and the exact functional depth of flow that provides water to the intake (entrainment envelope). This result may assist the water plant operators in determining the required submergence depth necessary for intakes situated in river and the actual location of discharge outfalls in river so as not to potentially impact the flow quality.
- (5) The computational investigation of 3-D flow concludes that the validity of the potential flow solution is limited to low and moderate intake discharges, that is, if the intake flow proportion to the total flow in the domain is $1.2\% \leq Q_i/Q \leq 5.6\%$. The potential flow solution gives acceptable results for inviscid flow condition.
- (6) The 3-D delineation of the entrainment envelope is required for the laminar flow condition while the 2-D study may be considered sufficient for inviscid flow condition. Also, 3-D investigation of the envelope is highly imperative for intake flow proportion above $Q_i/Q > 16.67\%$ for both flow conditions.
- (7) The numerical simulation of laminar (viscous) flow revealed the presence of vorticity in the channel flow and its effect on the entrainment envelope. It concludes that high magnitudes of clockwise vortices are present in the vicinity of the intake pipe for the high intake withdrawal rate (Cases 4 and 5). Also, the vorticity diffusion into the flow resulted into entrainment envelope distortion and substantially increased the dimensions of the intake entrainment envelope which

cannot be predicted via potential and inviscid flow assumptions. The three dimensional study of this flow condition supports this deduction by confirming the presence of these vortices at water intakes. This observation supports the work of Carriveau et al. [2000].

- (8) The defined intake entrainment envelope may be instrumental in delineating the Intake Protection Zone (IPZ) and refining the predicted domain of the IPZ.

5.2 Recommendations for Future Works

The scope of this research provides an excellent judgment in delineating an entrainment envelope. However, as inferred earlier in this thesis that the research area is an emerging one and aimed at achieving a better prediction of the entrainment envelope, some of the topics of interest that can further expand the scope includes;

- (1) Incorporation of the dataset into potential flow expression, continuity equation and Navier-Stokes equations so as to generate a mathematical model that can accurately calculate the entrainment envelope at an instant.
- (2) Consideration of asymmetrical location of the hydraulic intake (when $y_u \neq y_l$) will be vital in evaluating its effect on the entrainment envelope and will establish a better comparison with the symmetrical location considered in this study.
- (3) Numerical study of the effect of turbulence interaction at the vicinity of the intake by estimating the mean and turbulence quantities on the entrainment envelope. Further 3-D study on the location where vortices are prevailing will be consequential in mitigating its effect on water intake discharge capacity.
- (4) Experimental investigation of the three dimensional velocities of the flow into the water intake will further foster the delineation of the entrainment envelope.

REFERENCES

- Ansar, M., Nakato, T. and Constatinescu, G. 2002. Numerical Simulations of Inviscid Three-Dimensional Flows at Single and Dual Pump Intakes, *Journal of Hydraulic Research*, 40(4): 461-470.
- Ansar, M. and Nakato, T. 2001. Experimental Study of 3-D Pump-Intake Flows with and without Cross Flow, *Journal of Hydraulic Engineering*, 127(10): 825-834.
- Anwar, H.O. 1966. Formation of a Weak Vortex, *Journal of Hydraulic Research*, 4(1): 1-16
- Carriveau, E.C., Baddour, R.E. and Kopp, G.A. 2002. The Entrainment Envelope of Dye-Core Vortices at Submerged Hydraulic Intakes, *Canadian Journal of Civil Engineering*, 29: 400-408.
- Carriveau, E.R. 2004. Earth Tech Intake Hydrodynamic Investigation Final Report, Hydrodynamic Research Group, University of Windsor, Canada.
- Celik, I. B. 2004. Procedure for Estimation and Reporting of Discretization Error in CFD Applications, *Journal of Fluids Engineering Editorial Policy Statement on the Control of Numerical Accuracy*, <http://journaltool.asme.org/Templates/JFENumAccuracy.pdf>.
- Chen, Z., Ettema, R. and Lai, Y. 2004. Ice-Tank and Numerical Study of Frazil Ingestion by Submerged Intakes, *Journal of Hydraulic Engineering*, 130(2): 101-111.
- Freitas, C.J. 1999. Perspective: Selected Benchmarks from Commercial CFD Codes, *Journal of Fluids Engineering*, 117: 208-218.
- Freitas, C.J., Ghia, U., Celik, I.B., Roache, P. and Raad, P. 2003. ASME'S Quest to Quantify Numerical Uncertainty, 41st Aerospace Sciences Meeting and Exhibit, Reno, Nevada, American Institute of Aeronautics and Astronautics, 2003-0627
- Fluent Inc. 2005. *Fluent 6.2 User's Guide*, Fluent Inc, Lebanon.

- Gulliver, J.S. and Rindels, A.J. 1987. Weak Vortices at Vertical Intakes, *Journal of Hydraulic Engineering*, 113(9): 1101-1116.
- Hite, J.E. and Mih, W.C. 1994. Velocity of Air-Core Vortices at Hydraulic Intakes, *Journal of Hydraulic Engineering*, 120(3): 284-297.
- Holtschlag, D. J. and Koschik, J. A. 2002. Contents of an An Acoustic Doppler Current Profiler Survey of Flow Velocities in Detroit River, a Connecting Channel of the Great Lakes, US Geological Survey Open-File Report 03-219, Lansing, Michigan.
- Kirchhoff, R.H. 1985. *Potential Flows: Computer Graphic Solutions*, Marcel Dekker, Inc., New York.
- Marghzar, S.H., Rahimzadeh, H. and Montazerin, N. 2002. Numerical Simulation at an Asymmetric Horizontal Intake, 5th International Conference on Hydro - Science and Engineering, Article 305, Warsaw, Poland.
- Munson, B.R., Young, D. F. and Okiishi, T. H. 2002. *Fundamentals of Fluid Mechanics*, 4th Edition, John Wiley & Sons, New York.
- Ontario Ministry of Environment. 2006. Clean Water Act and Source Water Protection Program, (<http://www.ene.gov.on.ca/en/water/cleanwater/index.php>)
- Ontario Ministry of Environment. 2006. Surface Water Vulnerability: Source Protection Draft Guidance Module, (http://www.ene.gov.on.ca/envision/gp/5600e_4_Surfacewater-r.pdf).
- Padmanabhan, M. and Hecker, G.E.1984. Scale Effects in Pump Sump Models, *Journal of Hydraulic Division, ASCE*, 110(11): 1540-1556.
- Tokyay, T.E. and Constantinescu, S.G. 2006. Validation of a Large-Eddy Simulation Model to Simulate Flow in Pump Intakes of Realistic Geometry, *Journal of Hydraulic Engineering*, 132(12): 1303-1315.

- U.S. Environmental Protection Agency. 2006. Surface Water Assessment and Protection Program, (<http://www.epa.gov/r5water/cwa.htm>)
- White, F.M. 2003. Fluid Mechanics, McGraw-Hill Companies, Inc., New York.
- Yildirim, N. 2004. Critical Submergence for a Rectangular Intake, *Journal of Engineering Mechanics*, 130(10): 1195-1210.
- Yildirim, N. and Jain, S.C. 1981. Effect of a Surface Layer on Free Surface Vortex, *Proc., 18th Int. Association for Hydraulic Resources, Delft, The Netherlands* 4: 411-418.
- Yildirim, N. and Kocabas, F. 1995. Critical Submergence for Intakes in Open Channel Flow, *Journal of Hydraulic Engineering*, 121(12): 900-905.
- Yildirim, N. and Kocabas, F. 2002. Prediction of Critical Submergence for an Intake Pipe, *Journal of Hydraulic Research*, 40(4): 507-518.
- Yildirim, N., Kocabas, F. and Gulcan, S.C. 2000. Flow-Boundary Effects on Critical Submergence of Intake Pipe, *Journal of Hydraulic Engineering*, 126(4): 288-297.
- Yuan, S.W. 1967. *Foundations of Fluid Mechanics*, Prentice-Hall, Englewood Cliffs, New Jersey.

APPENDICES

APPENDIX A

SCALING PARAMETERS FOR EXPERIMENTAL AND NUMERICAL MODEL

The experimental and numerical models employed in this study were obtained through the Froude scaling law techniques. The technique is governed by the principle that the Froude number is equal in both the prototype - Detroit River and the models. As a result of dimension limitations imposed by the laboratory settings, some model parameters were justified in relative to their proportionality to the prototype (denoted by asterisk) while the essential prototype dimensions were modeled directly according to the scaling laws. The following equations show the relationship that ensued from the scaling law. The obtained parameters are presented in Table A1 and A2 for both experimental and numerical model respectively.

$$\text{Froude number } F = \frac{V_m}{\sqrt{g_m L_m}} = \frac{V_p}{\sqrt{g_p L_p}} \quad (\text{A-1})$$

$$\text{Length ratio } L_r = \frac{L_m}{L_p} = \frac{1}{125} \quad (\text{A-2})$$

$$\text{Velocity ratio } V_r = \frac{V_m}{V_p} = \sqrt{L_r} \quad (\text{A-3})$$

$$\text{Flow ratio } Q_r = \frac{Q_m}{Q_p} = \sqrt{L_r^5} \quad (\text{A-4})$$

where F_r is the Froude number. L_r is the length ratio, L_m is the model length, L_p is the prototype length, V_r is the velocity ratio expressed in terms of length ratio, V_m is the model velocity, V_p is the prototype velocity, Q_r is the flow rate ratio, Q_m defines the model flow rate and Q_p defines the prototype flow rate.

Table A.1: Relevant scaling parameters for experimental model

Parameters	Prototype	(units)	Model	(units)
River Reach Length	$L_p = 1625$	(m)	$L_m = 13$	(m)
Intake Diameter	$d_p = 2.44$	(m)	$d_m = 0.02$	(m)
River Reach Velocity	$V_p = 0.60$	(m/s)	$V_m = 0.05$	(m/s)
River Reach Flow	$Q_p = 3879$	(m ³ /s)	$Q_m^* = 0.02$	(m ³ /s)
Intake Submergence	$S_p = 9.45$	(m)	$S_m^* = 0.25$	(m)
River Reach Width	$w_p = 640$	(m)	$w_m^* = 1$	(m)
Intake Penetration	$I_p = 140$	(m)	$I_m^* = 0.5$	(m)
Intake Flow	$Qi_p = 1.40$	(m ³ /s)	$Qi_m^* = 0.005$	(m ³ /s)

Table A.2: Relevant scaling parameters for computational model

Parameters	Prototype	(units)	Model	(units)
River Reach Length	$L_p = 1125$	(m)	$L_m = 9$	(m)
Intake Diameter	$d_p = 2.44$	(m)	$d_m = 0.02$	(m)
River Reach Velocity	$V_p = 0.60$	(m/s)	$V_m = 0.05$	(m/s)
River Reach Flow	$Q_p = 3879$	(m ³ /s)	$Q_m^* = 0.45$	(m ³ /s)
Intake Submergence	$S_p = 9.45$	(m)	$S_m^* = 1.5$	(m)
River Reach Width	$w_p = 640$	(m)	$w_m^* = 3$	(m)
Intake Penetration	$I_p = 140$	(m)	$I_m^* = 0.5$	(m)
Intake Flow	$Qi_p = 1.40$	(m ³ /s)	$Qi_m^* = 0.005$	(m ³ /s)

APPENDIX B

PROPERTIES OF WATER

The properties of water utilized in this study were extracted from the general physical properties of fluid prepared by Munson et al. (2002). These properties are tabulated in Table A1.

Table B.1: Properties of water at 20°C

ρ (kg/m ³)	γ (kN/m ³)	ν (m ² /s)	σ (N/m)	c (m/s)	p_v (N/m ²) _{abs}
998.2	9.789	1.004 x 10 ⁻⁶	7.28 x 10 ⁻²	1481	2.338 x 10 ³

APPENDIX C

CONVERGENCE HISTORY

The numerical solutions generated by CFD code, FLUENT were accepted in this study based on the techniques and procedures described by Freitas [1999] and following the specific guidelines provided in the Journal of Fluids Engineering Policy for numerical accuracy. The convergence histories of the normalized scaled residuals, the surface integrals for mass flow rate, the lift and drag coefficients were dynamically monitored during each run. Additionally, the overall mass, momentum and scalar balance for each run were checked for all the unsteady conditions. The criteria on which these histories were validated are described in the following sections.

C1. Convergence of residual history

The grid independence test presented in Section 3.4.5 established that the simulated results can be affected by the quality of the computational grid and the type of meshing schemes employed. Other influencing factors that delay the convergence of residuals for the solution variables as stated in FLUENT User's Guide [2005] includes excessive skewness in the grid, wrong choice of discretization schemes and inappropriate selection of model parameters. These factors increases the required computing time and results in fluctuations of the residuals and monitored variables. To this end, the convergence was monitored by ensuring that the residuals decay to some small value (based on the set up convergence criterion) and then leveled out (stop changing). Simulation runs with oscillation were stopped and discarded as the case arises. The residual history of a converged solution is presented in Figures C1, C2 and C3 for both 2-

D and 3-D cases. Only the convergence history similar to these figure are used for analysis.

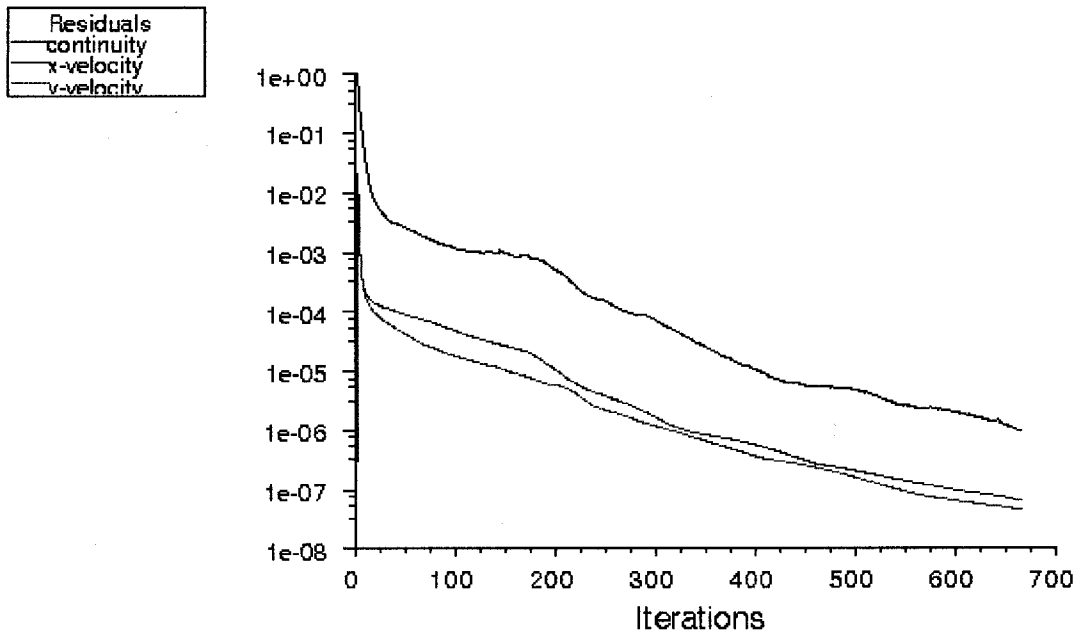


Figure C1: Convergence of residuals for 2-D laminar model (intake proportion $Q/Q = 0.0833$; Test A)

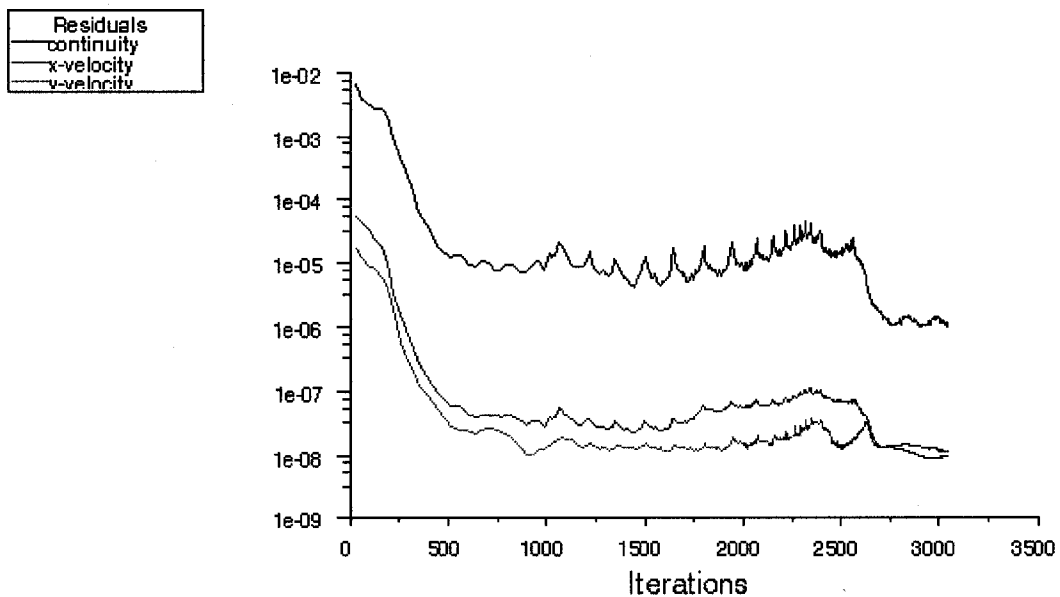


Figure C2: Convergence of residuals for 2-D laminar model
($Q/Q = 0.0167$; Test A)

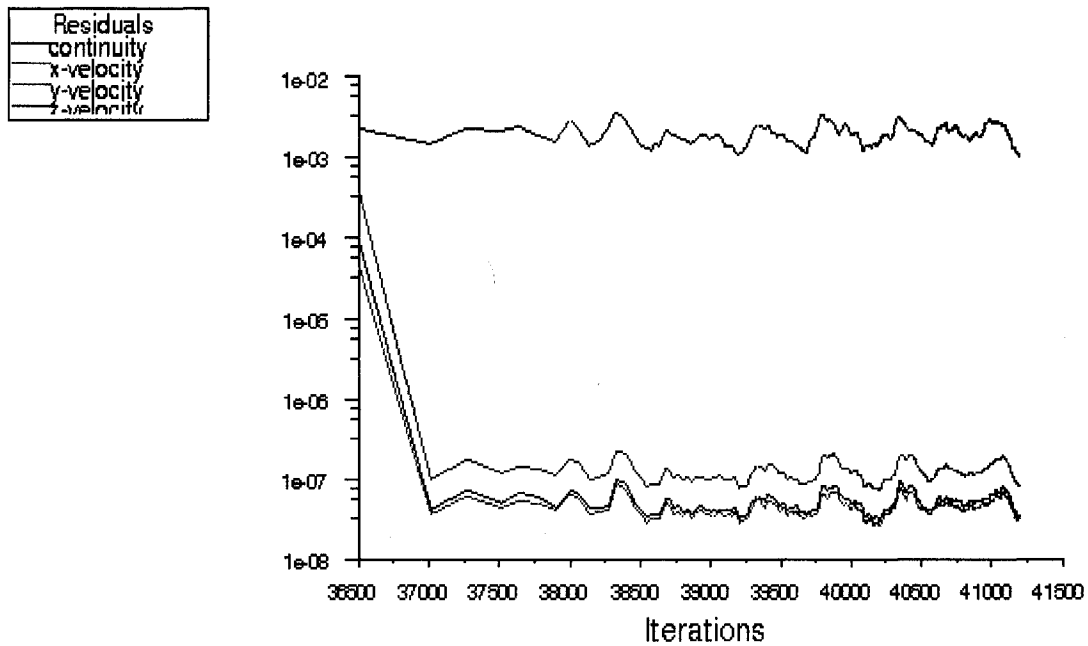


Figure C3: Convergence of residuals for 3-D laminar model

($Q_i/Q = 0.034$; Test B)

C2. Convergence of monitored flow variables

The integral report of a field variable was also used to check the convergence of the solution. The mass flow rate of the velocity magnitude, a known factor, was monitored on the intake outlet by ensuring that the average value on the surface stops changing. At this point, the monitored variable values remain unchanged even if the governing equation discretization scheme is changed. Also, the drag and lift coefficients were monitored alongside with the surface integral in order to validate the convergence. Presented in Figures C4, C5 and C6 are the plots of mass flow rate, C_d and C_l . The results obtained for the C_d and C_l were confirmed with their analytical equations. The coefficients were found to decrease as the iteration progresses and eventually became steady with more iteration steps.

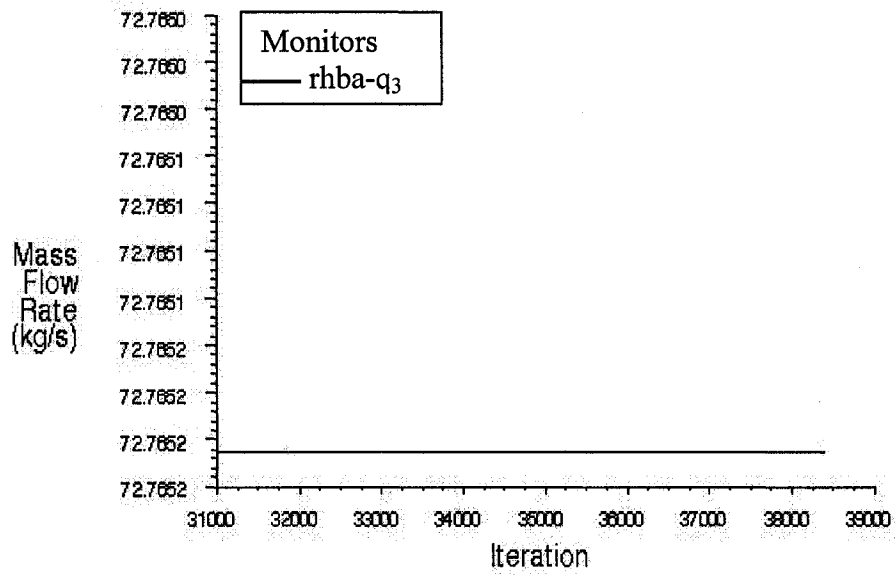


Figure C4: Convergence of mass flow rate on intake outlet for 3-D laminar model ($Q_i/Q = 0.385$; Test A)

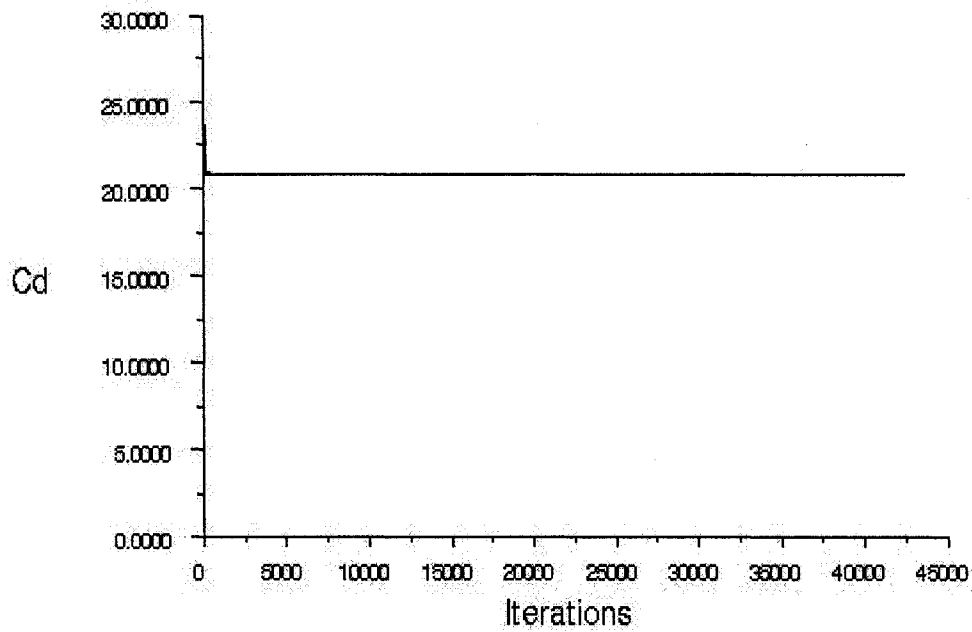


Figure C5: Convergence of drag coefficient for 3-D laminar model ($Q_i/Q = 0.345$; Test B)

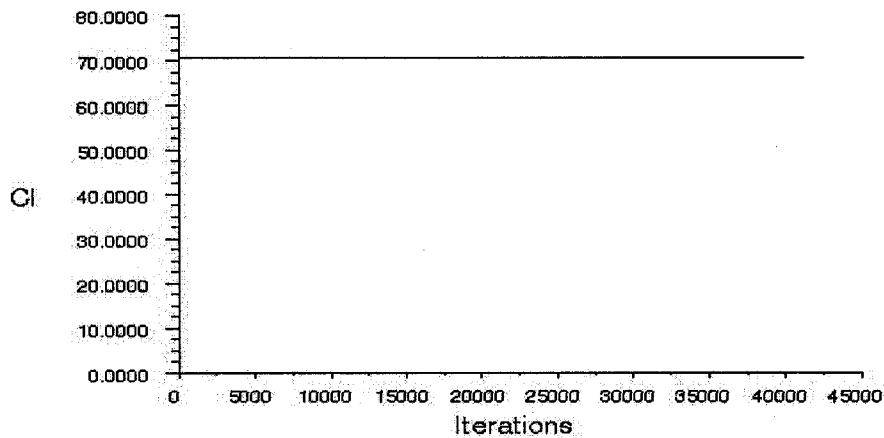


Figure C6: Convergence of lift coefficient for 3-D laminar model
($Q_i/Q = 0.345$; Test B)

C3. Convergence by flux report

The overall mass, momentum, energy and scalar balances were obtained in the flux report panel to ensure that the mass and energy are suitably conserved. In this case the results were achieved by ensuring that the net imbalance is less than 0.2% of the net flux through the entire domain. Table C1 presents the net flux through the computational domain by considering the mass distribution in the intake outlet, channel outlet and the channel inlet. The result agrees well with the specification in the FLUENT User's Guide [2005].

Table C.1: Flux report

Option	Zone/Boundaries	Results
Mass Flow Rate	channel - inlet	449.19001
	channel - outlet	-444.14291
	intake - outlet	-5.0470989
Net flux (kg/s)		-2.220446e-13

APPENDIX D

NUMERICAL ERROR ANALYSIS

Grid convergence analysis GCI was used to estimate the error of important parameters of the study which includes the entrainment envelope width, the radial distance above the intake to the envelope and horizontal distance from intake centre to the stagnation point (SG). The GCI is a measure of the percentage the computed value is different from the asymptotic numerical value. It indicates an error band on how far the solution is from the asymptotic value. It indicates how much the solution would change with a further refinement of the grid. A small value of GCI indicates that the computation is within the asymptotic range. The recommended procedures as outlined in the Journal of Fluids Engineering Policy for CFD accuracy [Celik 2004] are described in the following order:

- (1) Define a representative cell, mesh or grid size h in 2-D

$h = \left[\frac{1}{N} \sum_i^n (\Delta A_i) \right]^{\frac{1}{2}}$ where A_i is the area of the i^{th} cell and n is the total number of cells used.

- (2) Choose three different sets of grids and run simulation to obtain the key variables important to the study. Calculate the grid refinement factor or theoretical order of convergence $r = \frac{h_{coarse}}{h_{fine}}$ to obtain the r values for the number of grids investigated. In this study, the flow field is computed on four grids and the value of r_{21} , r_{32} and r_{43} are calculated accordingly using the number of grids and cells in the domain. These

values were used to calculate the apparent order P with the order of convergence obtained from the grid refinement result (ϕ) detailed in Chapter 3.

(3) Calculate the apparent order using expression:

$$P = \frac{1}{\ln(r_{21})} \left[\ln \frac{\varepsilon_{32}}{\varepsilon_{21}} \right] + q(p) \text{ where } q(p) = \ln \frac{r_{21}^p}{r_{32}^p}$$

$\varepsilon_{32} = \phi_3 - \phi_2$, ε_{21} and ε_{43} are calculated accordingly.

Apply Richardson extrapolation expression to obtain extrapolated values;

$\phi_{\text{ext}}^{21} = (r_{21}^p \phi_1 - \phi_2)/(r_{21}^p - 1)$; with these expressions, ϕ_{ext}^{32} and ϕ_{ext}^{43} are calculated.

(4) Using the apparent order P ; calculate the error with the following expression;

$$\text{Approximate relative error: } e_a^{21} = \left[\frac{\phi_1 - \phi_2}{\phi_1} \right]$$

$$\text{Extrapolated relative error: } e_{\text{ext}}^{21} = \left[\frac{\phi_{\text{ext}}^{12} - \phi_1}{\phi_{\text{ext}}^{12}} \right]$$

The fine grid convergence index is then defined as:

$$GCI_{\text{fine}}^{21} = \left[\frac{F_s e_a^{21}}{r_{21}^p - 1} \right]. \text{ Where } F_s \text{ is the factor of safety}$$

The factor of safety used in this study is 1.25. This was recommended for comparison of three or more grids. The grid convergence error for the subsequent grid is

calculated using this format with reference to the grid convergence table in Chapter 3.

Table D1 shows the error report.

Table D.1: Error estimate for H and r_o

H/d_o	Error (%)	r_o/d_o	Error (%)
15.3251		6.1473	
13.4112	0.915	5.1583	0.8230
12.4407	0.607	4.1601	0.5120
12.4406	0.001	4.1600	0.0008

APPENDIX E

UNCERTAINTY ANALYSIS OF EXPERIMENTAL DATA

The uncertainty analysis presented below is based on the methodology for estimating uncertainty in LDA measurements developed by Yanta and Smith (1973) and Schwarz et al. (1999). A 95% confidence interval is assumed in the following analysis. The main source of error in the LDA measurements is the uncertainty in the determination of the frequency present in each burst by the processor. In addition to the above, the uncertainty in statistical quantities will also depend on the sample size (N), this gives the precision error and can be calculated as the standard deviation of the sample. The authors derived the total uncertainty in the streamwise (σ_u) and cross-stream (σ_v) components of the mean velocity respectively as following:

$$\frac{\sigma_u}{U} = \left[(\sigma_o)^2 + \frac{1}{N} \left(\frac{u}{U} \right)^2 \right]^{1/2} \quad (1)$$

$$\frac{\sigma_v}{U} = \left[(\sigma_o)^2 + \frac{1}{N} \left(\frac{v}{U} \right)^2 \right]^{1/2} \quad (2)$$

where σ_o is the error due to the uncertainty in the determination of the beam-crossing angle which is equivalent to 0.4 according to Schwarz et al. (1999), N is the number of samples (121 data points), U is the mean inlet velocity in the flume and u and v are the velocity measurement obtained at point $(-1d_o, 1d_o)$ for Case 3. By solving above equations, the typical estimates of uncertainties for the mean quantities of the velocity u and v are 0.56% and 0.49% respectively.

APPENDIX F

TABULATED DATA SET

F1. Comparison of 2-D numerical inviscid result with potential flow theory

Table F1 details the variation in the entrainment envelope width by comparing the analytical and numerical inviscid results. Analytical data is denoted with subscript a while the inviscid data is presented with subscript f . The asymptotic values are measured from the intake centre to the envelope in the positive $+y$ direction. The calculated loss of symmetry that occurred as a result of singularities effect is tabulated in Figure F2. Q_i/Q is the proportion of channel flow drawn into the intake and H is the entrainment envelope width.

Table F.1: Analytical data comparison with numerical inviscid data

Intake discharge	Test A			Test B			Test C		
	$Q_i/Q(\times 10^{-3})$	$H/d_{(a)}$	$H/d_{(f)}$	$\% \Delta$	$H/d_{(a)}$	$H/d_{(f)}$	$\% \Delta$	$H/d_{(a)}$	$H/d_{(f)}$
16.7	2.49	2.60	-3.85	2.49	2.83	-13.25	2.49	2.30	7.96
50.0	7.49	7.40	1.30	7.49	7.34	2.11	7.49	7.48	0.24
83.3	12.49	12.35	1.17	12.49	12.31	1.50	12.49	12.71	-1.70
250.0	37.49	37.54	-0.13	37.49	36.52	2.59	37.49	38.48	-2.64
416.7	62.48	62.50	-0.03	62.48	63.05	-0.91	62.48	60.52	3.13

Table F.2: Effect of singularity on entrainment envelope (EE) width

Test	Change in Entrainment Envelope (H/d_0)				
	Q1	Q2	Q3	Q4	Q5
A	-0.412	-0.036	0.422	1.972	3.978
B	-0.648	-0.304	-0.368	-1.952	1.129
C	0.292	-0.267	-0.288	0.216	-0.260

F2. Summary of two-dimensional flow data

Table F3 presents the results obtained from the delineation methods employed in this study. The analytical result is denoted with subscript a , subscript f designates the inviscid result and subscript l denotes the laminar flow condition. The experimental data is not stated here because they were data observed at non-asymptotic state. However, the radial distance above intake centre to the entrainment envelope (r_o) was measured and compared with analytical data and they were found to concur with both analytical and numerical approaches. EE denotes the entrainment envelope.

Table F.3: Entrainment envelope data for 2-D solution

Intake Discharge	Entrainment envelope width (H)								
	Test A			Test B			Test C		
Q_i/Q ($*10^{-3}$)	$H/d_{o(a)}$	$H/d_{o(f)}$	$H/d_{o(l)}$	$H/d_{o(a)}$	$H/d_{o(f)}$	$H/d_{o(l)}$	$H/d_{o(a)}$	$H/d_{o(f)}$	$H/d_{o(l)}$
16.7	2.49	2.60	2.50	2.49	2.83	2.51	2.49	2.30	1.65
50.0	7.49	7.40	7.06	7.49	7.34	7.06	7.49	7.48	7.66
83.3	12.49	12.35	12.50	12.49	12.31	12.50	12.49	12.71	13.92
250.0	37.49	37.54	37.69	37.49	36.52	37.70	37.49	38.48	38.96
416.7	62.48	62.50	102.87	62.48	63.05	66.12	62.48	60.52	79.24

Intake Discharge	Radial distance above intake centre to EE (r_o)								
	Test A			Test B			Test C		
Q_i/Q ($*10^{-3}$)	$r_o/d_{o(a)}$	$r_o/d_{o(f)}$	$r_o/d_{o(l)}$	$r_o/d_{o(a)}$	$r_o/d_{o(f)}$	$r_o/d_{o(l)}$	$r_o/d_{o(a)}$	$r_o/d_{o(f)}$	$r_o/d_{o(l)}$
16.7	1.25	1.29	1.27	1.25	1.29	1.31	1.25	1.24	1.18
50.0	3.75	3.82	3.79	3.75	3.83	3.84	3.75	3.84	3.85
83.3	6.25	6.48	6.61	6.25	6.50	6.46	6.25	6.56	6.69
250.0	18.75	21.50	21.42	18.75	26.10	21.43	18.75	21.64	21.69
416.7	31.25	39.03	40.08	31.25	39.62	37.30	31.25	38.98	32.56

Intake Discharge	Horizontal distance from intake centre to EE (r_s)								
	Test A			Test B			Test C		
Q_i/Q ($*10^{-3}$)	$r_s/d_{o(a)}$	$r_s/d_{o(f)}$	$r_s/d_{o(l)}$	$r_s/d_{o(a)}$	$r_s/d_{o(f)}$	$r_s/d_{o(l)}$	$r_s/d_{o(a)}$	$r_s/d_{o(f)}$	$r_s/d_{o(l)}$
16.7	0.80	0.81	0.80	0.80	0.81	0.81	0.80	0.80	0.81
50.0	2.39	2.47	2.45	2.39	2.48	2.44	2.39	2.45	2.41
83.3	3.97	4.15	4.15	3.97	4.20	4.14	3.97	4.05	4.16
250.0	11.93	13.80	13.70	11.93	13.90	13.54	11.93	13.70	13.72
416.7	19.89	25.80	18.33	19.89	25.90	23.13	19.89	25.85	21.95

F3. Summary of three-dimensional flow data

Table F4 presents the analytical and numerical data for both flow conditions of Test B. The analytical result is depicted with subscript a , numerical inviscid result is represented with subscript f and numerical laminar data is represented with subscript l . EE designates the entrainment envelope.

Table F.4: Entrainment envelope data for 3-D solution of Test B

Q_i/Q (*10 ⁻³)	EE depth (D)			EE width (H)		Radial distance from intake centre to EE (r_o)			Horizontal distance from intake centre to EE (r_s)		
	$D/d_{o(a)}$	$D/d_{o(f)}$	$D/d_{o(l)}$	$H/d_{o(f)}$	$H/d_{o(l)}$	$r_o/d_{o(a)}$	$r_o/d_{o(f)}$	$r_o/d_{o(l)}$	$r_s/d_{o(a)}$	$r_s/d_{o(f)}$	$r_s/d_{o(l)}$
11.2	8.9	9.6	9.1	9.8	9.1	6.2	6.8	6.3	4.5	4.7	4.5
34.5	15.5	15.7	16.5	16.8	16.5	11.0	11.5	11.6	7.7	8.6	8.7
58.8	19.9	20.3	20.0	21.7	21.0	14.0	14.8	14.6	9.9	10.1	11.1
200.0	34.6	35.5	35.0	39.8	41.6	24.2	26.7	31.0	17.3	19.2	25.1
384.0	44.6	45.5	55.0	53.8	57.5	31.6	36.6	49.0	22.3	26.5	30.1

VITA AUCTORIS

Temitope V. Olatunji was born in 1978 in Ilesa, Nigeria. She graduated from Ilesa Grammar School, Ilesa in 1995. From there she went to Federal Polytechnic Ede where she obtained a National Diploma in Architectural Technology in 1997. She proceeded to Federal University of Technology Akure where she obtained a B.Eng in Civil Engineering with a First Class honour in 2004. She is currently a candidate for the Master's degree in Civil Engineering at the University of Windsor and hopes to graduate in Fall 2007.